UC Berkeley
UC Berkeley Electronic Theses and Dissertations

Title
Hybrid Two-Dimensional Electronic Systems and Other Applications of sp-2 Bonded Light Elements

Permalink
https://escholarship.org/uc/item/2r083103

Author
Kessler, Brian Maxwell

Publication Date
2010

Peer reviewed|Thesis/dissertation

eScholarship.org Powered by the California Digital Library
University of California

Hybrid Two-Dimensional Electronic Systems and Other Applications of sp-2 Bonded Light Elements

by

Brian Maxwell Kessler

A dissertation submitted in partial satisfaction of the
requirements for the degree of
Doctor of Philosophy

in

Physics

in the

GRADUATE DIVISION
of the
UNIVERSITY OF CALIFORNIA, BERKELEY

Committee in charge:
Professor Alex Zettl, Chair
Professor Feng Wang
Professor Seung-Wuk Lee

Spring 2010

Hybrid Two-Dimensional Electronic Systems and Other Applications of sp-2 Bonded Light Elements

Copyright 2010
by
Brian Maxwell Kessler

Abstract

Hybrid Two-Dimensional Electronic Systems and Other Applications of sp-2 Bonded Light Elements

by

Brian Maxwell Kessler
Doctor of Philosophy in Physics

University of California, Berkeley

Professor Alex Zettl, Chair

The field-effect is a cornerstone of modern technology lying at the heart of transistors in consumer electronics. Experimentally, it allows one to continuously vary the carrier concentration in a material while studying its properties. The recent isolation of graphene, the first truly two-dimensional crystal, allows application of the field effect to a much wider range of physical situations. In the first part of the thesis, we investigate hybrid materials formed by coupling metals to the two-dimensional electron gas (2DEG) in graphene. We couple superconducting materials to the graphene sheet by cluster deposition. This material displays a superconducting phase whose properties are tuned by the carrier density via the field effect. The transition temperature is well-described by Berezinskii-Kosterlitz-Thouless vortex unbinding. The ground state properties show interesting effects due to the distribution of cluster spacings. Observations related to other hybrid electronic systems including ferromagnets and normal metals are presented. The second part of this thesis involves energy applications of light element materials. The mechanisms affecting coating of carbon nanotubes using atomic layer deposition is developed and applied to photovoltaic systems. The gas adsorption properties of activated boron nitride are investigated and the relative influence of surface area and hydrogen binding affinity is elaborated. The third part of this thesis explores electromechanical properties of suspended graphene membranes. We investigate buckling and strain in exfoliated graphene membranes as well as their deformation under an applied gate potential.

To everyone who helped,

Thanks for everything.

Contents

List of Figures v

List of Tables vii

I Electronic Correlations Coupled into Two Dimensions 1

1 Introduction 2

2 Tuning Superconductivity in Two Dimensions 4
2.1 History and Overview of Theory 4
2.2 Coupling Superconducting Correlations into Graphene 4
2.2.1 Deposition of Low Melting Point Materials on Graphene 5
2.2.2 Analysis of Normal State Properties Before and After Sn Deposition . 5
2.3 The Superconducting Transition 11
2.3.1 Berezinskii-Kosterlitz-Thouless Physics 13
2.3.2 Nonlinear Current-Voltage Relationship 15
2.4 Ground State Properties 16
2.4.1 Critical Currents 16
2.4.2 Magnetoresistance and Critical Fields 18
2.4.3 High-Magnetic Field Effects and Splitting of the Dirac Point 22
2.5 Conclusions and Future Work 23

3 Other Two-Dimensional Hybrid Structures 26
3.1 Transport Through Superlattices of Ferromagnets 26
3.1.1 Overview of Theory and Device Structure 26
3.1.2 Magnetoresistance in Parallel Fields 27
3.1.3 Magnetoresistance in Perpendicular Fields 29
3.1.4 Magnetic Force Microscopy Characterization of Magnetic Configuration 32
3.2 Non-local Resistance of Modified van der Pauw Disks 34

4 Hexagonal Boron Nitride: A Two-Dimensional Dielectric 38
4.1 Dielectric Properties 40

4.1.1 Device Fabrication 40
4.1.2 Breakdown Strength 40

II Energy Applications of sp-2 Bonded Materials 43

5 Hydrogen Storage 44
5.1 Motivation and Types of Storage 44
5.2 Theoretical Considerations for Physical Adsorption 45
5.3 Synthesis of Activated Boron-Carbon-Nitride (a-BCN) materials 46
5.4 Hydrogen Absorption of Properties of a-C and a-BN 48
5.4.1 Dominant Role of Brunauer-Emmett-Teller surface area 49
5.5 Future Directions 49

6 Nanotube Based Dye-Sensitized Solar Cells 51
6.1 History, Overview and Theory of Operation 51
6.2 Atomic Layer Deposition of Titania on Nanotubes 52
6.2.1 Effect of Temperature on Morphology and Coating Efficiency 55
6.3 Coating of Forests for Production of Solar Cells With Carbon Nanotube Electrodes 56

III Other Research 61

7 Two-Dimensional Mechanical Membranes 62
7.1 Device Fabrication 62
7.2 Buckling and Strain in Suspended Graphene 62
7.3 Electrostatic Deflection of Suspended Graphene 65

Bibliography 69

A Device Fabrication 76
A.1 Exfoliated Graphene Devices 76
A.1.1 Exfoliation of samples onto prepared wafers 77
A.1.2 Optical identification of thin flakes 77
A.1.3 Raman scattering analysis of thin flakes 78
A.1.4 Alignment to scratches for exfoliated graphene 81
A.2 Chemical Vapor Deposition Devices 83
A.3 Production of the finest features requires attention to the proximity effect . . 84
A.4 Production of holey substrates for graphene electromechanical measurements 86

B Experimental Protocols 87
B.1 Electrical Measurements 87
B.2 He-3 Refrigeration 88

C Basic graphene electronic properties **91**

List of Figures

1.1 General principle of tunable hybrid systems . . . 3

2.1 Morphology of low melting point metal deposition on graphene . . . 6
2.2 Comparison of Raman spectra before and after Sn deposition. . . . 7
2.3 Device Overview . . . 8
2.4 Effect of Sn on room temperature transport . . . 9
2.5 Effective contact resistance due to Fermi level pinning . . . 11
2.6 3D view of superconducting transition . . . 12
2.7 Branched view of the superconducting transition . . . 13
2.8 Fits to the superconducting transtion. . . . 14
2.9 Mean field and BKT Transition Temperatures as a function of gate voltage. . . 15
2.10 Power law scaling of the Current-Voltage characteristics across the BKT transition. . . . 17
2.11 Comparison of the scaling exponent and flux-flow resistance across the BKT transition . . . 18
2.12 Current voltage characteristics at low temperatures . . . 19
2.13 High resolution differential resistance at low temperatures. . . . 20
2.14 Low field magnetoresistance at low temperatures . . . 21
2.15 Critical currents and nonlinear resistance as a function of perpendicular magnetic field. . . . 22
2.16 High field magnetoresistance at low temperatures and Dirac peak splitting . . 24
2.17 Patterned Josephson junction superlattice. . . . 25

3.1 Device concept for magnetic transport measurements. . . . 27
3.2 False color SEM image of magnetic superlattice device . . . 28
3.3 In-plane magnetoresistance at low temperatures . . . 29
3.4 Summary of the in-plane magnetoresistance hysteresis and the zero-field resistance of the device. . . . 30
3.5 Low-field perpendicular magnetoconductance . . . 31
3.6 Scattering lengths as a function of gate voltage . . . 32
3.7 Appearance of a satellite Dirac peak in high magnetic fields . . . 33
3.8 Magnetic force microscopy characterization of sample properties. . . . 34
3.9 Modified van der Pauw disk . . . 35
3.10 Electrical Transport of modified van der Pauw disk . . . 36

3.11 Predicted magnetic response of the modified van der Pauw disk 37

4.1 Hexagonal boron nitride structure. 39
4.2 Optical micrographs of BN microcrystals deposited using the scotch tape method. 39
4.3 Electrical breakdown of a BN single crystal. 41
4.4 Electrical breakdown characteristics of dielectric materials. 42

5.1 Characterization of the activated boron nitride. 47
5.2 Comparison of hydrogen adsorption isotherms for a-C and a-BN 48
5.3 Enthalpy of Hydrogen absorption for a-C and a-BN 50

6.1 Dye sensitized solar cell and power generation characteristics 52
6.2 Charge conduction in dye-sensitized solar cell electrodes 53
6.3 The ALD process cycle for deposition of TiO_2 53
6.4 The "ALD window" for controlled layer-by-layer deposition 54
6.5 EELS Characterization of TiO_2 coated MWNT 57
6.6 Effect of Temperature on ALD Coating 58
6.7 Dual Stage Coating Process 59
6.8 Nanotube forest coated by ALD TiO_2 59
6.9 IV Characteristics of a DSC with a carbon nanotube electrode fabricated in the Zettl lab. 60

7.1 Schematic of the measurement geometry for electrostatic AFM measurements. 63
7.2 Wrinkling in graphene sheets exfoliated over holes 64
7.3 Imaging electrostatic deflection of bilayer graphene. 66
7.4 Extraction of mechanical parameters from the maximum deflection of the graphene sheet as a function of gate voltage. 68

A.1 Contrast vs. height for hBN microcrystals 79
A.2 Raman spectra of different graphene layer thicknesses 80
A.3 Alignment and patterning exfoliated graphene sheets. 82
A.4 Electrical characterization of CVD graphene devices 84
A.5 Image of closely spaced fine features using e-beam lithography 85

B.1 Schematic of Cryo Industries ^{3}He fridge 89

C.1 Graphene lattice structure 92
C.2 Graphene electronic band structure 92

List of Tables

5.1 DOE Hydrogen Storage Targets for 2015. 45
5.2 Comparison of adsorption properties for activated carbon and activated boron nitride 49

7.1 Summary of wrinkling data measured by AFM and Raman spectroscopy. . . 65

Part I

Electronic Correlations Coupled into Two Dimensions

Chapter 1

Introduction

Electronic order in two dimensions is one of the richest areas in the study of condensed matter. Traditional three dimensional electronic phases such as superconductivity, magnetism, and charge density waves have different manifestations due to the reduced dimensionality[35]. In addition, completely new types of electronic order develop such as the integer and fractional quantum hall states[76, 74]. Recent experimental and theoretical work has produced even more novel phases such as topological insulating states like the quantum spin hall state[43]. The majority of previous studies have focused on thin films of three dimensional materials or interface/surface states. However, the recent isolation of truly two dimensional materials[13] such as graphene has opened the door to new possible experimental realizations. In particular, graphene allows the ability to more easily couple different electronic correlations into two dimensions.

The bipolar two-dimensional electron gas (2DEG) present in graphene[30] is markedly different from the buried 2DEGs found at oxide interfaces or in GaAs heterostructures in that it is 'open' to the environment with a stable and inert surface. Using standard 2DEGs it is only feasible to capacitively couple the electron gas to materials deposited on their surface[62, 77], whereas graphene is expected to allow direct coupling and thus offer access to different regions of phase space[69]. In this work we sought to determine whether bulk materials deposited directly onto the graphene surface, such as metal clusters, can act as dopants and efficiently couple through the electron gas, whose carrier density and type can be tuned by an applied gate voltage. The low carrier density in graphene, relative to bulk values, and weak intrinsic interactions such as spin-orbit coupling, should limit back-action of the electron gas on dopant properties. Thus, exposed graphene sheets could provide a near-ideal substrate for the manipulation and general study of proximity-induced electronic phases. The general device schematic for the first part of this thesis is shown in figure 1.1

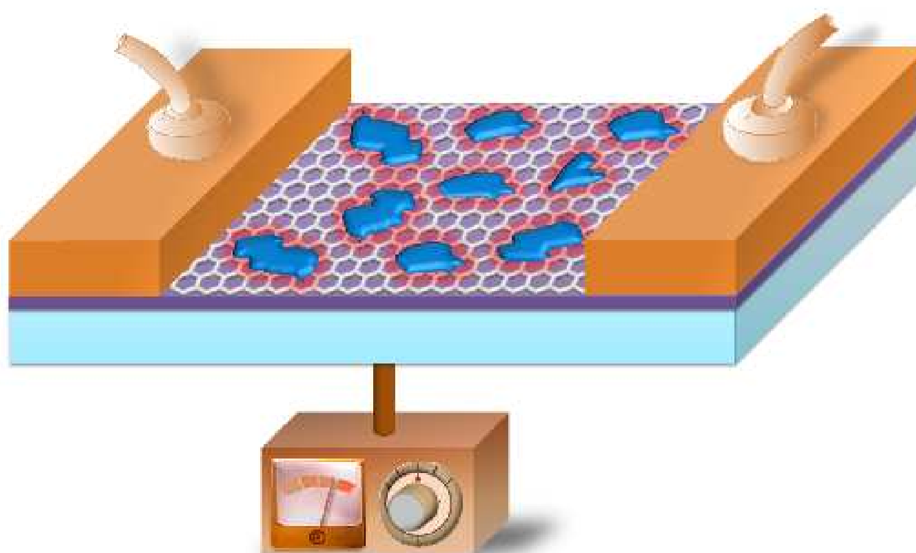

Figure 1.1: Schematic of the general principle of tunable hybrid systems formed by coupling materials to graphene sheets. The graphene (honeycomb) is supported on an insulating gate dielectric. The blue clusters are materials with interesting electronic properties. The correlations extend into the graphene sheet a characteristic length illustrated by the red coloring. Gold contacts allow measurement of electronic transport. The back gate allows the carrier density and coupling of dopants to be tuned via an applied potential (tuning knob). The open surface can be accessed via a range of local probes.

Chapter 2

Tuning Superconductivity in Two Dimensions

2.1 History and Overview of Theory

The superconducting transition in two-dimensions is of interest for both the fundamental understanding of electronic order in reduced dimensions and applications involving superconducting circuits and detectors. An open question is how the transition behaves as the density of carriers mediating the superconductivity is varied. In particular, the strength of disorder appears to play a fundamental role separating qualitatively different behavior[68]. In two-dimensions, the electric field-effect provides the most versatile method for tuning the carrier density of a system at fixed disorder. However, the field-effect places more stringent limits on the dimensionality of the system since the film must be thinner than the Debye length governing the screening of the electric field by charge carriers. In typical metals this length is much smaller than the penetration depth that places the limit on two-dimensional superconductivity. Despite this limitation, the field effect has been used to tune the superconducting transition in specific materials such as thin films with anomalously low carrier density[56] and interfacial states between complex oxides[14]. An alternative approach is to couple superconducting correlations directly into a truly two-dimensional electronic system, graphene.

2.2 Coupling Superconducting Correlations into Graphene

Graphene has been shown to effectively carry proximity-induced Josephson currents injected from contacting electrodes[36, 23]. However, a finite coherence length limits the length of such junctions to approximately one micron, reducing the physics to one-dimension, with junction length L governing the relevant physics. To maintain coherence over longer distances in two dimensions while retaining the unique properties of the graphene sheet we employ the geometry discussed previously (Fig. 1.1) where a large array of nanoscale dopant

islands is placed in a non-percolating network on top of the graphene sheet[28].

2.2.1 Deposition of Low Melting Point Materials on Graphene

To produce the island network, Sn or In (99.999% purity) was evaporated using an electron gun in high vacuum (10^{-7} torr) onto graphene substrates at room temperature. We find that low melting point metals such as the elemental superconductors Sn and In readily form self-assembled islands when deposited on pristine graphene at room temperature (Fig. 2.1) similar to previous results on graphite[38]. Analysis of scanning electron micrographs and atomic force micrographs (see figure 2.1) indicates that 10 nm of nominal deposition thickness (as measured by a quartz crystal monitor), typically results in islands with 80 ± 5 nm diameter and 25 ± 10 nm gaps between them.

We note the difference in morphology even between the Sn and In clusters. Sn tends to form irregular bulbous shapes, while the In forms well faceted nanocrystals. Interestingly, the facets of these nanocrystals tend to all fall along similar directions at angles of 15, 30 and 60 degrees. This indicates some degree of registry and commensurablity with the underlying graphene lattice. Thus, deposition of In could be used as a simples means of measuring the orientation of graphene samples by deposition and subsequent imaging of the orientation of the nanocrystals.

The melting point of In is extremely low for a metal (157 ^{o}C) hence its use in solders. This presents a problem for our investigations, since lithographic steps typically require annealing polymethylmethacrylate (PMMA) at 180 ^{o}C (see section A.3), which results in agglomeration and sintering of the In clusters changing their morphology and leading to large spacings. This could be avoided by the use of shadow masks. In subsequent sections we focus solely on samples coated with Sn.

2.2.2 Analysis of Normal State Properties Before and After Sn Deposition

Raman Spectra

The quality and monolayer nature of the exfoliated samples can be confirmed via Raman spectroscopy. In figure 2.2 the Raman spectrum of Sample A before and after deposition of Sn is shown. The single symmetric 2D peak unambiguously identifies this sample as a monolayer[29]. The quality of the sample is evident from a lack of a measurable D peak before deposition indicating that there are minimal crystalline defects in our sample. This mode is typically forbidden since it requires scattering from K to K' which fails to conserve crystal momentum. Thus, the mobility is limited by scattering from charged impurities in the substrate rather than crystal defects.

After deposition of Sn we notice prominent changes in the Raman spectra. Most significant is the appearance of the D peak at $\sim$1300 cm^{-1}. The question arises as to what defects are allowing the D process to occur. Since the Sn deposition is a low temperature process relative to the melting point of graphite, it seems unlikely that the deposition is actually inducing crystalline defects. One of the most prominent defects causing appearance

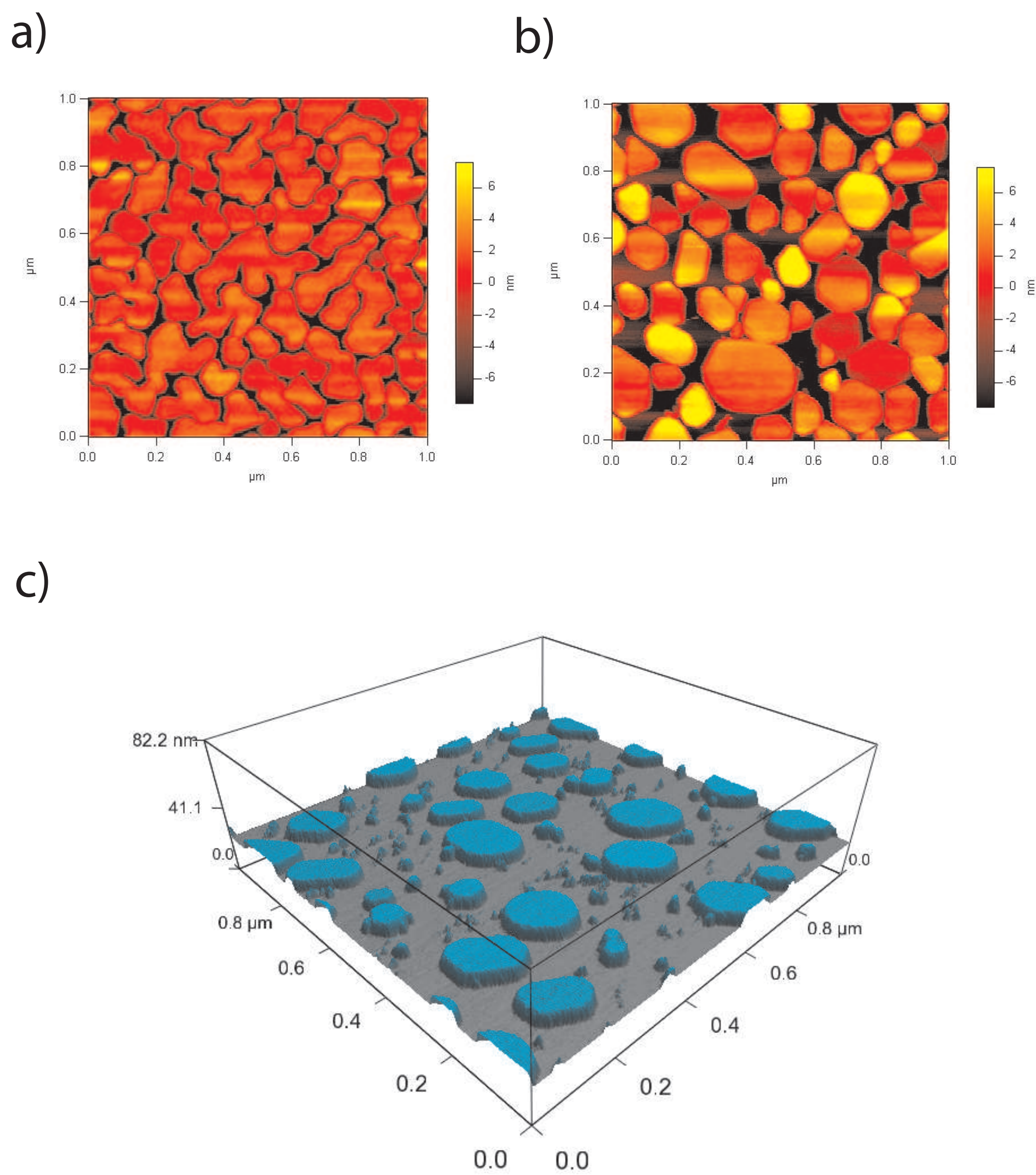

Figure 2.1: Morphology of low melting point metal deposition on graphene. AFM Images of Sn (a) and In (b) deposited onto graphene at room temperature. c) Image of sparse In deposition showing the very flat plate-like crystals formed.

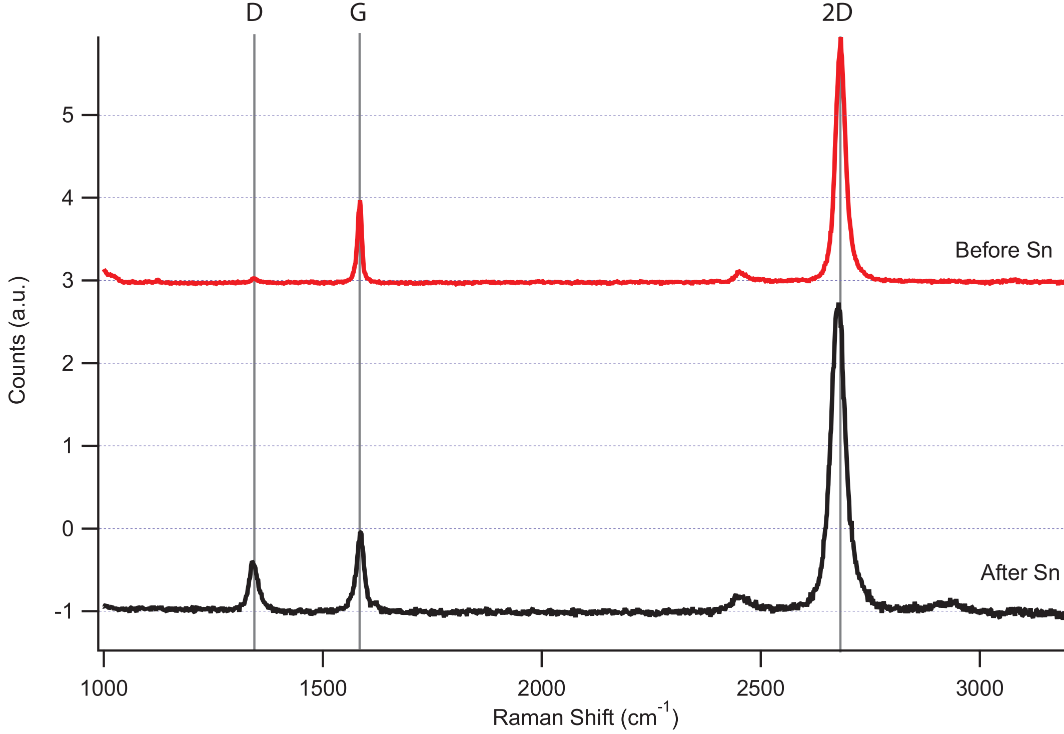

Figure 2.2: Comparison of Raman spectra before (red) and after (blue) Sn deposition acquired using 514 nm excitation. The intensity has been normalized to the G-peak intensity.

of the D-peak is edges which inherently do not conserve crystal momentum. The ratio of the D-peak intensity in small samples has actually been very well correlated to the domain size using the relation [12]

$$L_{domain}(\text{nm}) = \frac{560}{E_l^4}\frac{I_G}{I_D} \tag{2.1}$$

where E_l is the laser line energy in eV and I_G and I_D are the integrated peak intensities of the G and D modes respectively. For the 514 nm laser line used in our studies the multiplicative constant is 16.6 nm. Using the measured intensities of the G-to-D ratio (1.7 ± 0.2) for three samples, this formula gives a value of 28 ± 3 nm, which corresponds excellently with the observed gaps between islands via AFM and SEM images in the previous section.

Doping and Scattering

We now turn to the electronic properties of Sn decorated samples. Electron beam lithography was used to define four-probe contacts to the graphene sheet so that transport measurements could be made before and after Sn deposition. The degenerately doped Si acts as a back gate and allows us to control the carrier concentration in the graphene sheet.

In figure 2.4 we show the room-temperature field-effect characteristics of a device before and after Sn is deposited. Ideally, the charge neutrality point V_D in intrinsic graphene should

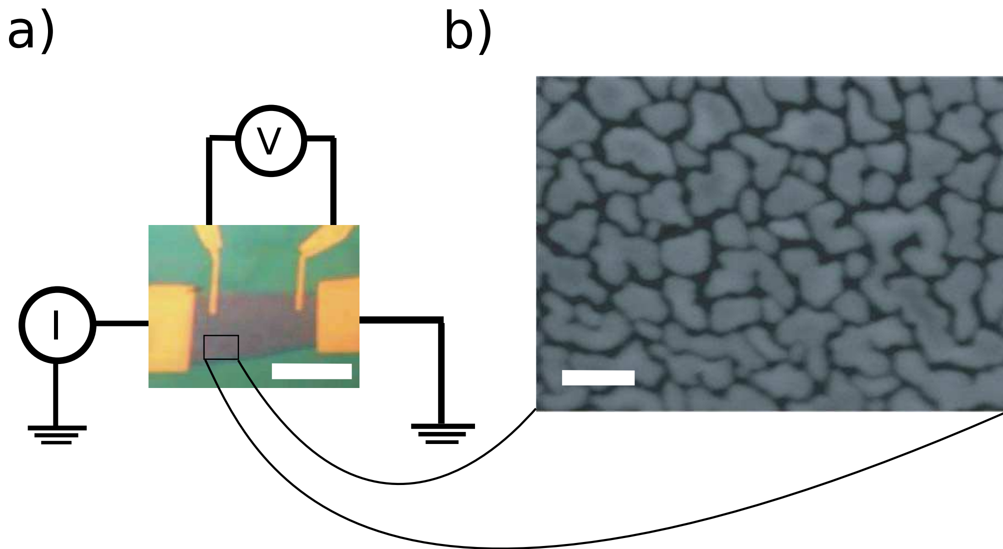

Figure 2.3: a) Optical image of a typical device showing the four probe configuration (Scale bar 10 microns). b) Scanning electron micrograph of Sn island morphology on the graphene sheet (Scale bar = 100 nm)

lie at a gate potential of zero volts. Typical of other groups producing exfoliated graphene on silicon oxide, we find our samples are initially p-doped such that the charge neutrality point occurs at a positive gate potential of +10 to +60 V as seen in figure 2.4. This shift is attributed to surface-charge doping the graphene sample $n_{imp} \sim 10^{12}$. The location of the charge neutrality point is fairly consistent for samples made in the same batch, but varies from batch to batch indicating sample fabrication plays a role in this unintentional doping. Work is currently underway to better control this unintentional doping.

Our pristine samples display room temperature field-effect mobilities of 2000-13000 $\mathrm{cm}^2/(\mathrm{V} \cdot \mathrm{s})$ which is typical of other groups' samples supported on SiO2 [30]. It is well known that the reduction of graphene mobility on SiO_2 is due to charged impurity scattering from the oxide[19].

Suspended graphene samples isolated from a substrate and annealed in UHV have been shown to produce mobilities of up to 200,000 $\mathrm{cm}^2/(\mathrm{V} \cdot \mathrm{s})$ [24]. However, structural stability limits such samples to dimensions of ∼1 micron, making them inadequate for the present work where we wish to probe the full two-dimensional physics.

The blue curve in figure 2.4 displays the field-effect characteristics of a device after the Sn is deposited. Although 40% of the graphene surface is coated by Sn islands after the deposition, many of the original electronic properties of graphene remain intact, including bipolar transport and field-effect mobilities $\mu > 1000\ \mathrm{cm}^2/(\mathrm{V} \cdot \mathrm{s})$. The three main effects of Sn deposition are a rigid shift in the charge neutrality point (Dirac point V_D) to more negative voltages, a factor of five decrease in mobility compared to the pristine graphene supported on silicon oxide, and a pronounced asymmetry between electron and hole transport. Note that the maximum resistance at charge neutrality remains unchanged, indicating that the

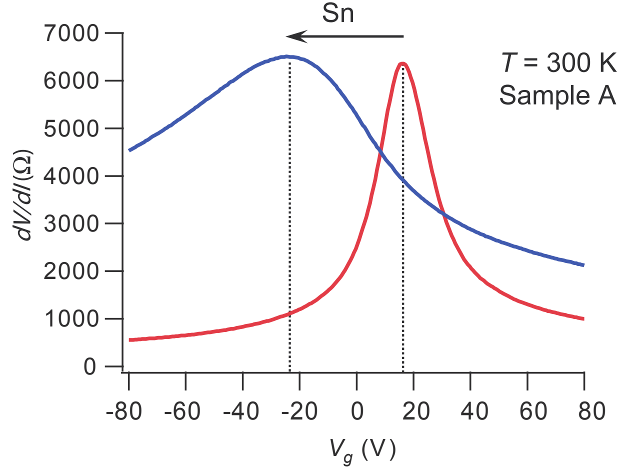

Figure 2.4: Effect of Sn on room temperature transport. Four-terminal sheet resistance as a function of gate voltage for Sample A before (red) and after (blue) Sn deposition. The dotted lines indicate the charge neutral point and the arrow indicates the shift after Sn deposition.

high coverage of low resistance Sn islands does not directly shunt the current in the graphene sheet and that we must consider the system as a coupled hybrid system.

All three of these effects are well described by inhomogeneous doping due to charge transfer from the metal islands to the graphene sheet[26]. Regardless of the location of the initial charge neutrality point, we find a consistent magnitude and direction of the neutrality point shift after deposition of Sn indicating that there is charge transfer between Sn and the graphene. From the shift in the charge neutrality point (V_D) on three separate samples and the known gate capacitance ($C_g = 115$ aF / μm^2) we can calculate the charge induced in the graphene sheet by the Sn, $n_{ind} = C_g \Delta V_D$. Normalizing by the observed Sn coverage, we infer that Sn transfers $9 \pm 2 \times 10^{12}$ cm^{-2} electrons to the graphene underneath it. This result is in agreement with recent experiments performed using other metals[58, 48]. Theoretically, this is expected from the difference in work functions between the two materials. Kelly et al. used density functional theory calculations to develop a simple model form [31]

$$\Delta E_F = \text{sgn}(\Phi_M - \Phi_G - \Delta_c) \frac{\sqrt{1 + 2\alpha D_0 (d_{eq} - d_0)|\Phi_M - \Phi_G - \Delta_c|} - 1}{\alpha D_0 (d_{eq} - d_0)} \tag{2.2}$$

where Φ_M and Φ_G are the metal and graphene work functions respectively, $\alpha = e^2/\epsilon_0 A =$ 349.3 eV/nm, $D_0 = 0.09$ from the density of states, and $\Delta_c = 0.9$ eV $d_{eq} = 0.33$ nm $d_0 = 0.24$ nm are fitting parameters to the density functional theory results. Using the values of $\Phi_G = 4.5$ eV and $\Phi_{Sn} = 4.42$ eV we obtain a theoretical charge transfer of 2.5×10^{13} cm^{-2}, a factor of $\sim$2 higher than our measured value. The discrepancy between this value and our inferred charge transfer from the Dirac point shift is possibly due to uncertainty in the distance of the metal layer to the graphene (eg. residual contaminants between the graphene and the metal surface).

The induced charge reduces the mobility of both types of carriers via charged impurity

scattering[19], which has been shown to be inversely related to the mobility of the charge carriers via

$$\mu = \frac{5 \times 10^{15}\,(\mathrm{V^{-1}s^{-1}})}{n_{imp}} \tag{2.3}$$

Taking the change in mobility before and after deposition of Sn we can use this equation to extract another estimate of the induced charge due to the metal deposition. Averaging over the electron and hole mobilities (due to the pronounced asymmetry), we obtain a value for the induced impurity content of $1.1 \pm 0.6 \times 10^{13}$ cm^{-2}, which agrees well with the independent estimate obtained above from the shift in the Dirac point. Note that this calculation does not depend on normalization by the covered area. The agreement of both methods gives us confidence in our assessment of the induced charge transfer.

We now turn to the question of the electron hole asymmetry. For charged impurities, it has been predicted[53] and shown experimentally[19] that there is an asymmetry induced between electrons and holes. However, the asymmetry we observe is actually in the opposite direction to what one expects from this effect, ie. holes have a more reduced mobility due to the induced electronic density while it is predicted that they should have a higher mobility. The explanation for the observed asymmetry is due to the inhomogeneous nature of the doping[26, 40]. The induced charge under the Sn islands pins the Fermi level below them so that they we measure an associated 'contact resistance' due to the potential barrier as carriers move between the islands.

The contact resistance due to such a potential barrier in graphene has been calculated using a model with a spatially varying k-vector, where the metal pins the Fermi wavevector underneath and it decays exponentially away from the interface over a characteristic distance d [40].

$$k_F(x) = k_F^{(m)} + \frac{k_F^{(g)} - k_F^{(m)}}{e^{-x/d} - 1} \tag{2.4}$$

where $k_F^{(m)}$ is the wavevector below the metal, $k_F^{(g)}$ is the graphene wavevector away from the metal determined by the gate potential. In the original theory, the distance d was just left as a parameter. To first order we can take this distance to be the Thomas-Fermi screening length $\lambda_{TF} = \frac{1}{4\alpha k_F}$ where $\alpha = \frac{4e^2}{\kappa \hbar v_F}$ with $\kappa = 3.9$ for SiO_2[13]. Using the induced charge measured for Sn deposited on graphene to infer the pinned wavevector $k_F^{(m)}$, we can calculate a resistance due to a potential step. In figure 2.5 we compare the result for a 30 nm wide step versus the experimentally measured resistance. Note that the simple model does not correctly deal with the behavior near the Dirac point where the k-vector does not actually diverge, but is actually limited to a finite value due to charge inhomogeneity[82].

In our sample, there are actually a distribution of such steps in parallel and series along with the intrinsic graphene sheet resistance. So, the exact value of the resistance contribution due to these steps is not known. This asymmetric effect is in addition to the (mostly) symmetric charged impurity scattering under the islands that reduces the inferred mobility overall. Full knowledge of the microstructure would be required to deconvolve these scat-

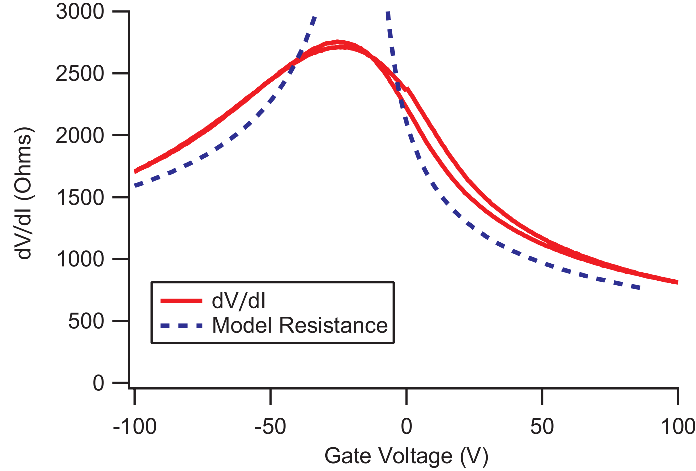

Figure 2.5: Effective contact resistance due to Fermi level pinning. The red line is experimental differential resistance measured as a function of gate voltage after Sn deposition. The blue dotted line is the calculated resistance for a 30 nm wide Sn junction representing the qualitative asymmetry in the transport characteristics.

tering processes. However, we note that the simple model does an excellent job reproducing the magnitude of the asymmetry in the transport characteristics.

2.3 The Superconducting Transition

In this section we explore the low temperature properties of this system [42]. To minimize oxidation of the Sn, the samples were immediately transferred to a He-3 cryostat and connected to highly filtered lines. Linear response and differential resistance were measured with standard low frequency (typically 17 Hz) lock-in techniques using low excitation currents in the range 10-100 nA. Samples were cooled slowly (0.3 K/min) to ensure that the sample was in thermal equilibrium with the cold stage and that measured temperatures were consistent.

As we lower the temperature, the effect the superconducting correlations in the Sn have on transport via the proximity effect becomes apparent. Figure 2.6 shows a three dimensional representation of the sheet resistance versus temperature for gate voltages on both the hole and electron sides of the charge neutrality point. At each gate voltage the curve exhibits two distinct features, a high temperature partial drop in resistance that occurs at ~ 3.5 K independent of gate voltage, and a broad transition between 3 K and 1 K to a state of zero resistance that is strongly dependent on the gate voltage. This is easier to see on a branched view of the transition shown in figure 2.7.

The first partial resistance drop is attributed to condensation of Cooper pairs in the Sn islands ($T_c^{Bulk} = 3.72$ K). Analysis of the drop shows that it can be fit by $\Delta\sigma(T) \propto \ln(T/T_{c0})^{-1}$ (figure 2.8) typical of Aslamazov-Larkin fluctuation-enhanced conductivity[2]

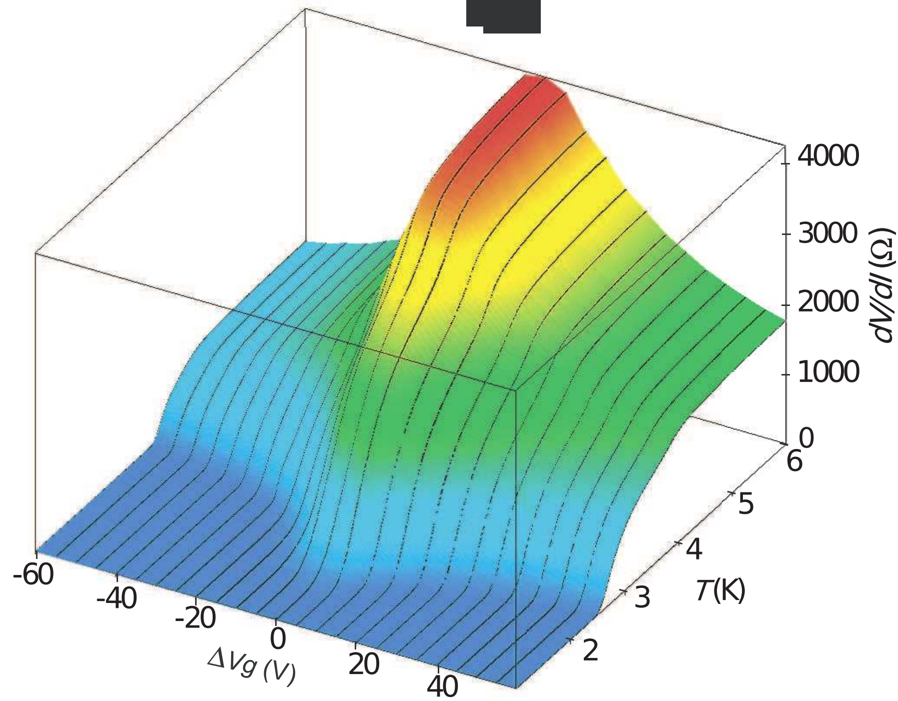

Figure 2.6: 3D view of superconducting transition. Sheet resistance versus temperature for various gate voltages, V_g, referenced to the charge neutrality point $V_D = +40$ V for this device. $\Delta V_g = V_g - V_D < 0$ corresponds to hole transport, whereas, $\Delta V_g > 0$ corresponds to electron transport through the graphene sheet.

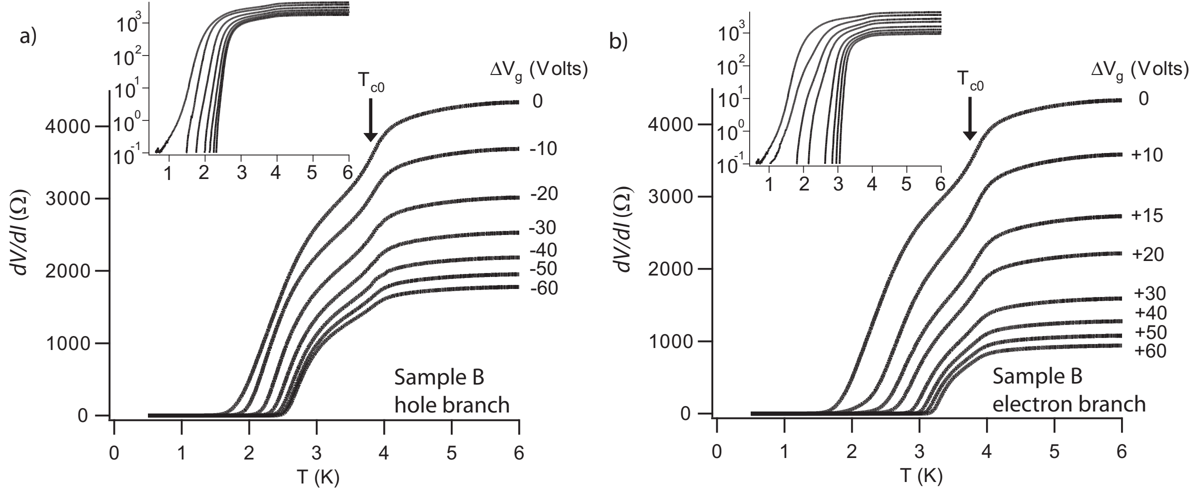

Figure 2.7: Branched view of the superconducting transition. Sheet resistance versus temperature for various gate voltages, V_g, referenced to the charge neutrality point $V_D = +40$ V for this device. In a) $\Delta V_g = V_g - V_D < 0$ corresponds to hole transport, whereas, $\Delta V_g > 0$ in b) corresponds to electron transport through the graphene sheet. The arrow labeled T_{c0} indicates the first partial resistance drop corresponding to the mean-field pairing transition of the Sn islands. Inset: Same data on a semi-log scale.

in two dimensions. Fitting each curve from $3.8 - 4.5$ K as shown in figure 2.8 we extract a mean-field pairing temperature (T_{c0}) of 3.54 ± 0.02 K independent of gate voltage (red squares in Fig. 2.9). Note that the amplitude of this drop is not directly proportional to the Sn coverage, indicating that the islands do not act as simple superconducting shunts and we must consider the coupled system.

2.3.1 Berezinskii-Kosterlitz-Thouless Physics

In two-dimensional superconducting systems, it is well known that although the amplitude of the superconducting wave function is well defined below the pairing temperature T_{c0}, thermally induced phase fluctuations (vortices) destroy global phase coherence and produce dissipation due to a finite flux-flow resistance[7, 45]. However, below the critical Berezinskii-Kosterlitz-Thouless unbinding temperature, T_{BKT}, the attractive interaction between vortices with opposite orientation (so-called antivortices) causes them to form bound pairs allowing a finite supercurrent to flow.

The vortex-unbinding temperature can be identified from the universal form of the flux-flow resistance[52], $R_\square$, due to the thermally excited vortices above the transition

$$R_\square(T) \propto \exp[b(T - T_{BKT})^{-1/2}] \tag{2.5}$$

where b is a constant of order unity governing the vortex-antivortex interaction strength and T_{BKT} is the vortex unbinding temperature. To extract this form we plot $(d\ln(R_\square)/dT)^{-2/3}$

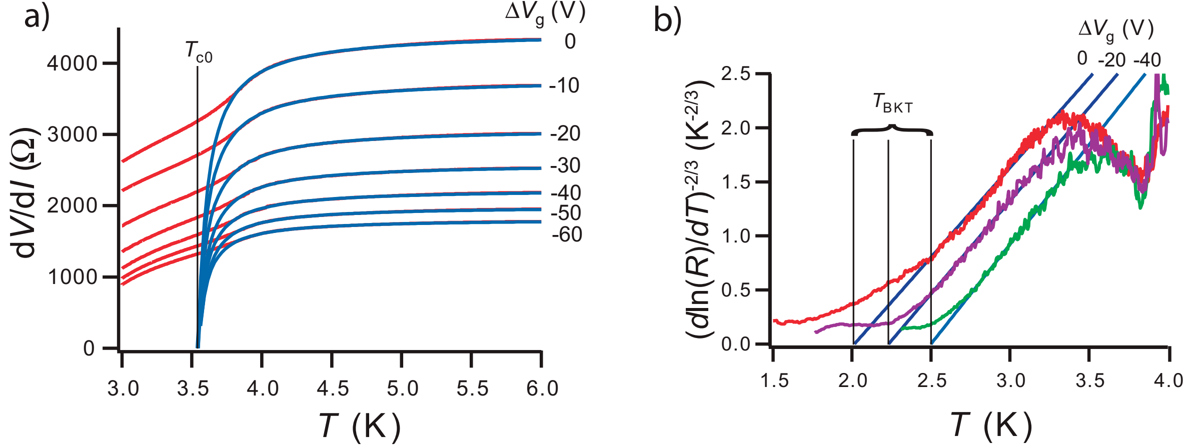

Figure 2.8: Fits to the superconducting transtion. a) Fits of the sheet resistance versus temperature to fluctuation-enhanced conductivity of the Aslamazov-Larkin form. The red lines are data from figures 2.6 and 2.7. The blue lines are fits to the Aslamazov-Larkin form. The average gate-independent T_{c0} is indicated. b) Rescaling of the sheet resistance versus temperature to the BKT form to extract the vortex unbinding temperature T_{BKT} at each gate voltage(see text).

vs. T, which produces a straight line with T_{BKT} given by the x-intercept for curves following the universal form. In figure 2.8 the resulting fits are given showing T_{BKT} extracted from the x-intercepts for three different gate voltages. Through a large intermediate range the curves follow the universal form (straight line). However, at low temperatures the curves level off due to finite-size effects, which cut off the attractive vortex-antivortex interaction[52]. This departure from the universal form is particularly evident near the charge neutrality point $\Delta V_g = 0$ (Fig. 2.8), possibly indicating proximity to a superconductor-normal quantum critical point at the lowest charge densities[67]. Figure 2.9 summarizes the resulting T_{BKT} (open circles) extracted from the resistance versus temperature curves at each gate voltage.

To analyze the gate voltage dependence of the vortex unbinding transition, $T_{BKT}(V_g)$, we can consider the sheet as a dirty two-dimensional superconductor where the gate voltage allows us to tune the normal state resistance. This model is justified since the length scales of disorder are much smaller than the superconducting coherence length, ie. $r \sim d \sim \ell_{mfp} < \xi_0$, where r is the size of the islands, d is the distance between islands, $\ell_{mfp} \sim 20-30$ nm is the mean free path extracted from field effect measurements at 6 K using C.7 and the superconducting coherence length Sn ($\xi_0^{Sn} \sim 300$ nm). For a dirty 2D superconductor, one can use the jump in superfluid stiffness at the vortex unbinding transition to relate T_{BKT} to the normal state resistance of the film[6, 25],

$$\frac{T_{c0}}{T_{BKT}}\left\{\frac{\Delta(T_{BKT})}{\Delta(0)}\tanh\left[\frac{\Delta(T_{BKT})}{2k_bT_{BKT}}\right]\right\} = \frac{\epsilon_v R_N}{R_0} \tag{2.6}$$

where $\Delta(T)$ is the superconducting energy gap, R_N is the normal state sheet resistance,

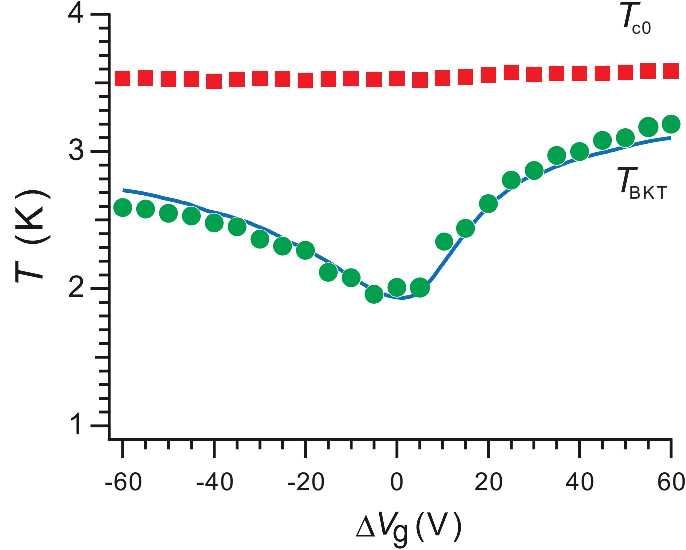

Figure 2.9: Mean field and BKT Transition Temperatures as a function of gate voltage. The mean-field pairing temperature, T_{c0} (red squares) and vortex-unbinding temperature, T_{BKT} (green circles) as a function of gate voltage. The solid blue line is a fit of T_{BKT} using equation 2.6 and the measured normal state properties of the device. (see text).

$R_0 = \frac{2.18\hbar}{e^2} \approx 8.96k\Omega$, and ϵ_v is an effective dielectric constant that describes the material dependent screening of the attractive vortex-antivortex interaction[25]. Using the weak-coupling BCS limit for the superconducting gap and the sheet resistance measured at 6 K, we fit the T_{BKT} extracted above using ϵ_v as the only adjustable parameter and find $\epsilon_v = 2.40 \pm 0.05$ (solid blue curve in figure 2.9), which is twice the value seen in related systems[25, 21]. This implies that the vortices and antivortices are relatively weakly bound in our system.

2.3.2 Nonlinear Current-Voltage Relationship

Another indicator of the Berezinskii-Kosterlitz-Thouless transition is revealed by the non-linear current voltage relationship near the transition. As seen above, thermally induced vortices produce a characteristic flux-flow resistance given by equation 2.5. In a similar manner, non-equilibrium current induced-vortices produce a characteristic dissipation as the BKT transition temperature is approached. Specifically, the voltage drop displays a crossover from ohmic behaviour $V \propto I$ above the transition to non-linear power law behavior $V \propto I^{\alpha}$ below the transition. At the BKT transition temperature, the exponent α is expected to jump discontinuously from 1 to 3 and increase monotonically for lower temperatures.

In figure 2.10, we display current-voltage curves on a log-log scale taken at a fixed gate potential of 0 V and temperatures from 1.6 - 4 K. As expected, the curves display a transition from linear (ohmic) behavior at high temperatures to nonlinear behavior at low temperatures. Note that at high currents, all of the curves retain the same normal-state ohmic resistance once the critical current for the film is exceeded. The dotted line corresponds to a power law with $\alpha = 3$ where we expect to see a jump. From the graph it appears that the the power

law transition happens at ~ 2.65 K. To quantitatively extract the non-linear exponent α we can take the logarithmic derivative of each IV curve to obtain $\alpha = \frac{\mathrm{dln}V}{\mathrm{dln}I}$. Doing this for each of the curves we get a value of $\alpha(T)$ as displayed in figure 2.11. We notice that the exponent displays a monotonic increase as temperature is lowered and there is no distinct jump from 1-3 as expected for the BKT transition.

We can compare the extracted non-linear exponent α with the linear resistance versus temperature analyzed using the flux-flow method of the previous section (equation 2.5). In figure 2.11 we display the flux-flow data in the form of equation 2.5, we extract a BKT transition temperature of 2.93 K, which corresponds to an exponent of $\alpha \simeq 2$. To reconcile this with the expected jump, we note that the observed renormalization of the vortex-antivortex interaction found in analysis of the linear resistance versus temperature data would imply a rounding of the jump[52].

2.4 Ground State Properties

2.4.1 Critical Currents

At temperatures well below T_{BKT}, all of the vortices and antivortices form bound pairs and a finite critical current develops which saturates to a gate-voltage dependent value for $T \ll T_{BKT}$. Full current-voltage characteristics as a function of applied gate voltage were obtained by applying a slowly varying triangle wave from a function generator to the biasing resistor and acquiring the induced voltage using an oscilliscope. As shown in figure 2.12, we observe a gate-tunable critical current of up to 10 μA 2.12. This critical current is qualitatively similar to isolated graphene Josephson junctions[36, 23] with the exception that, in our devices, critical current densities ($I_c/width \sim 1$ A/m) comparable to submicron graphene Josephson junctions are maintained over distances of tens of microns, demonstrating the fully two-dimensional phase coherence in this system.

To gain further insight into the critical current we can acquire high resolution differential resistance measurements as a function of bias current. The low noise and high resolution afforded by the lock-in technique allows us to probe the transition from the superconducting state to the normal state over four orders of magnitude in resistance. This reveals that the transition is not abrupt or smooth, but rather a cascading series of discontinuous jumps seen as plateaus in the differential resistance. We note that the fine structure observed is not an effect of measurement noise, but is reproducible from one scan to the next, indicating that it is a sample dependent quantity.

There are two prominent effects when the steps have been mapped out. First, all of the steps display a typical ‘V’ shape, with a minimum bias current at a gate voltage of $\sim$+29 V. Second, the value of the gate voltage where the minimum occurs decreases to more negative gate voltages for steps with a higher minimum bias current. When the device’s differential resistance increases to its normal state value, the minimum conductivity point occurs at a gate voltage of +12 V, which agrees with the normal state as well.

We now turn to relating these features to the known microstructure of this material. The ‘V’ shape of each step edge is very reminiscent of the critical current of an isolated Josephson

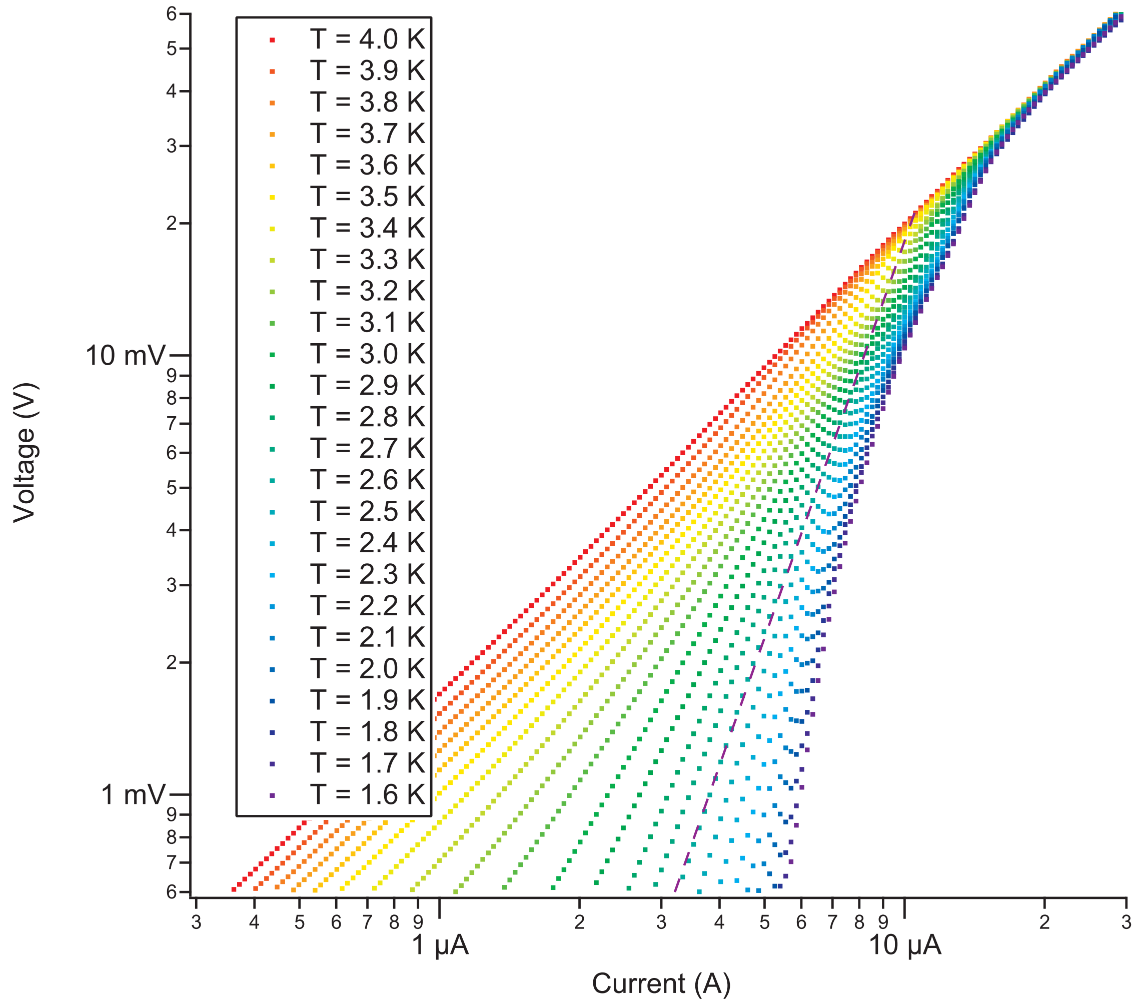

Figure 2.10: Power law scaling of the Current-Voltage characteristics across the BKT transition. Current-Voltage curves were taken at fixed gate potential of 0 V at various temperatures given in the legend. The dotted line indicates the expected $V \propto I^3$ power law scaling at the BKT transition.

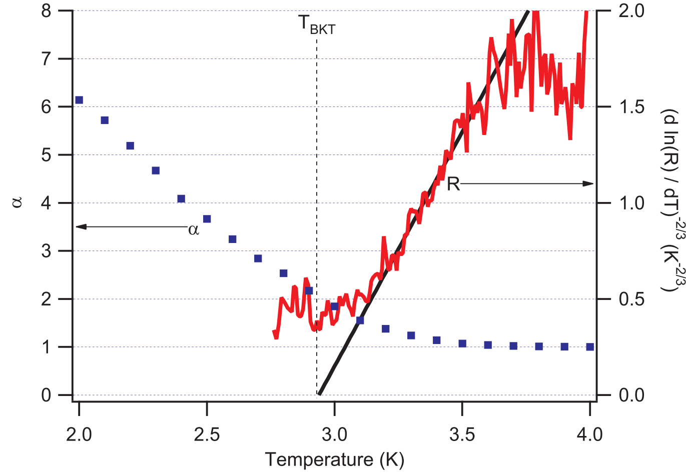

Figure 2.11: Comparison of the scaling exponent and flux-flow resistance across the BKT transition. Nonlinear exponent α on the left axis extracted from the IV curves in figure 2.10. Flux-flow resistance versus temperature for the same device on the right axis analyzed according to equation 2.5

junction[36, 23]. For this reason we attribute each step to the the transition of an individual Josephson junction (or possibly a set of junctions) to the normal state.

The leftward shift of the minimum bias point can qualitatively be described by short-channel effects due to non-zero screening of the doping away from the islands. Briefly, the channel between two Sn islands experiences an effective potential due to the partially screened charge transfer from the Sn islands. The charge transferred from the Sn decays over the Thomas-Fermi wavelength as discussed in section 2.2.2. For a short channel we can calculate the shift in gate voltage due to this decaying potential and find that for Sn and our gate dielectric it is well fit by

$$\Delta V_{eff} = \frac{94.5}{L} \text{ (V nm)} \tag{2.7}$$

and since I_c is also inversely proportional to the length of a Josephson junction through the relation $I_c \propto R_N^{-1}$ we can explain the observed shift in gate voltage for the higher current steps as being due to the transition of shorter junctions.

2.4.2 Magnetoresistance and Critical Fields

In addition to temperature and current, a finite magnetic field can also disrupt the superconducting state. There are two possible mechanisms by which magnetic fields lead to dissipation in a two-dimensional superconductor at zero temperature. First, a magnetic field introduces free vortices into the system. These vortices should cause a dissipation for any finite magnetic field due to the Lorentz force $v \times B$ producing a voltage drop across the sample. However, for a disordered sample, the vortices can be pinned at defects and thus

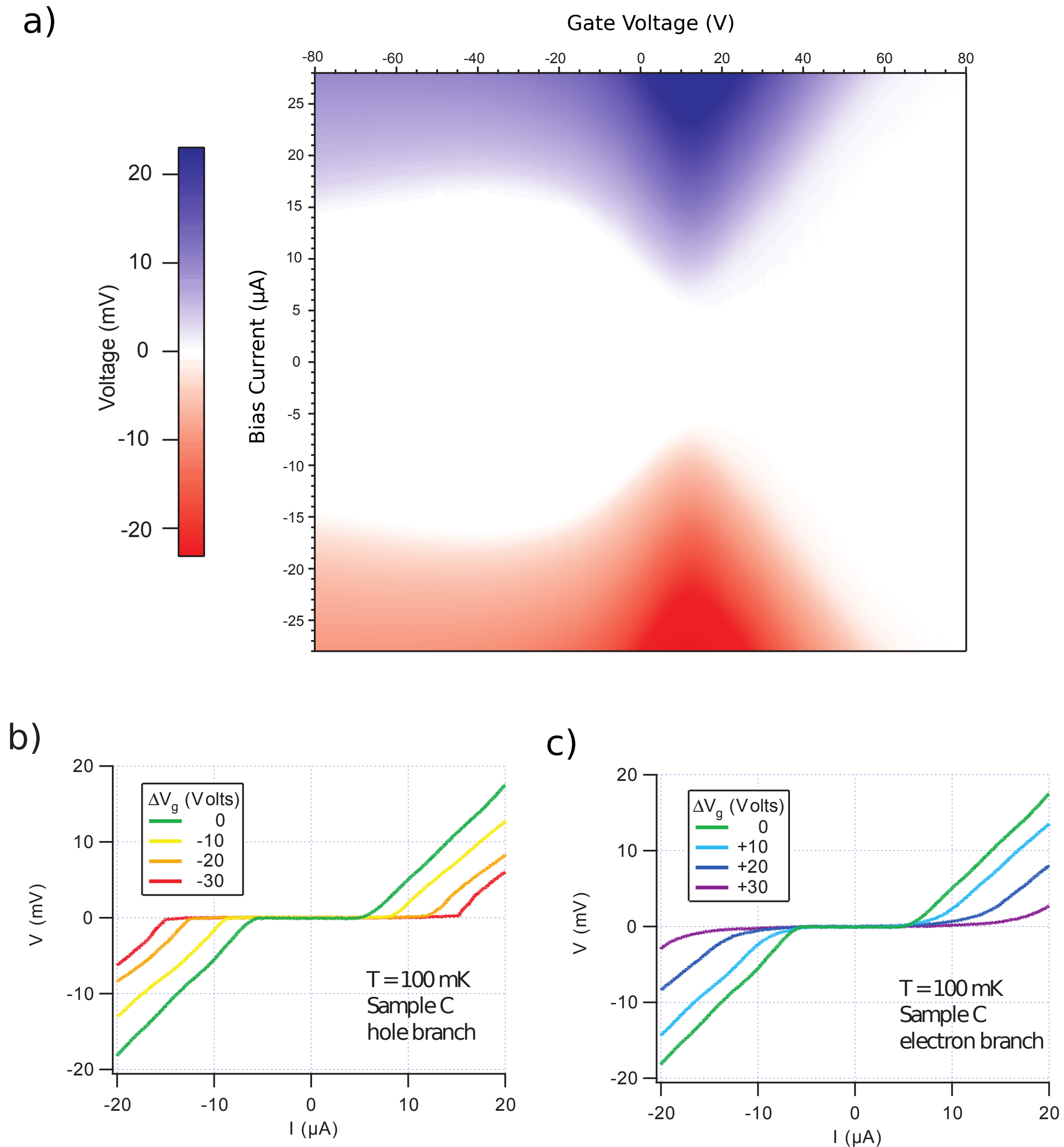

Figure 2.12: Current voltage characteristics at low temperatures. a) Two-dimensional map of current-voltage characteristics as a function of gate voltage taken at zero magnetic field and 100 mK. The horizontal axis corresponds to gate voltage and the vertical axis to bias current. The color scale indicates the measured voltage. (b-c) Individual current-voltage traces taken from the map shown in a) corresponding to hole transport (b) or electron transport (c) in the graphene sheet for gate voltages, ΔV_g relative to the Dirac point $V_D = +12$ V for this sample.

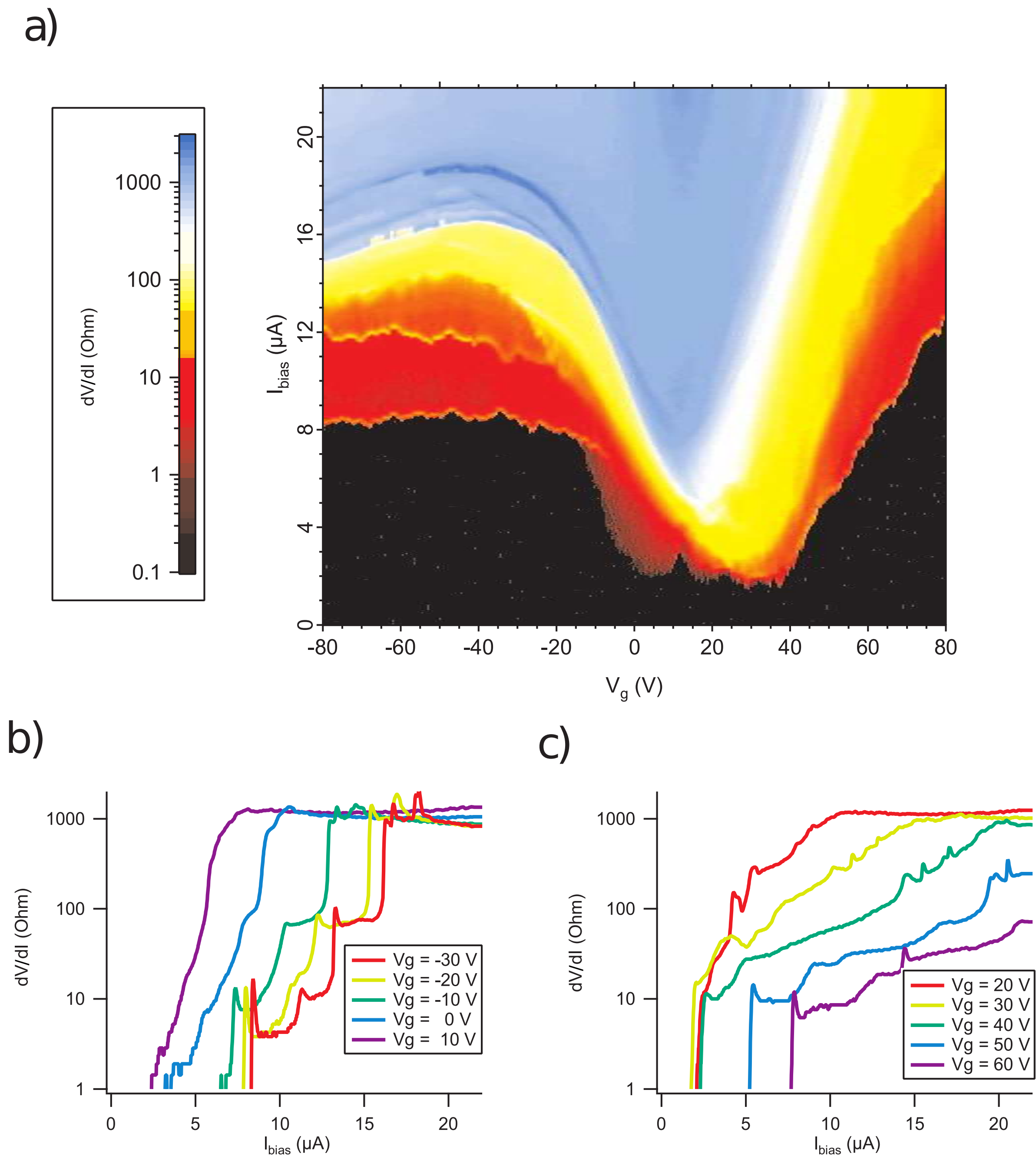

Figure 2.13: High resolution differential resistance at low temperatures. a) High resolution two-dimensional map of differential resistance on a logarithmic color scale as a function of gate voltage on the horizontal axis and bias current on the vertical axis. Data were taken at 100 mK and zero magnetic field. (b-c) Differential resistance traces as a function of bias current for various gate voltages on the hole (b) and electron (c) side of the Dirac point taken from the map in (a). The plateaus in differential resistance are clearly visible as steps in these traces.

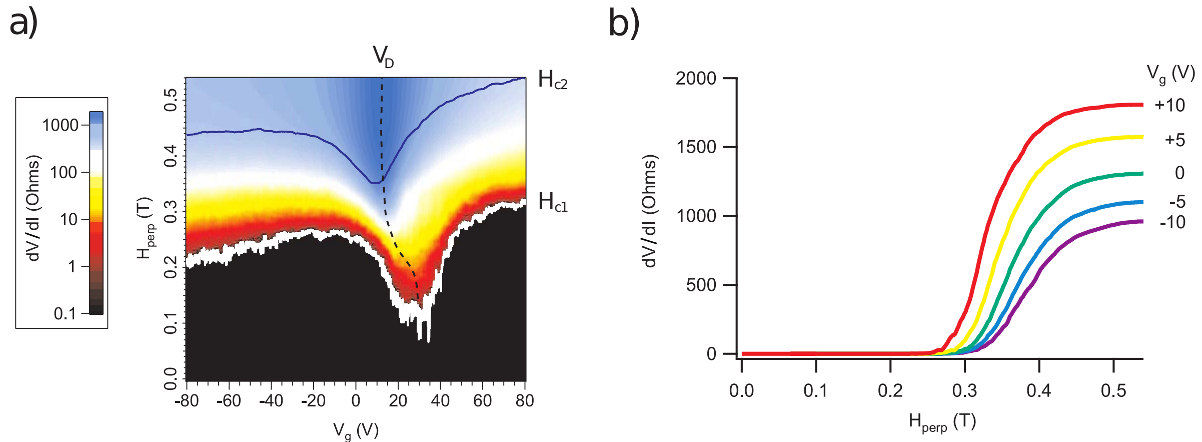

Figure 2.14: Low field magnetoresistance at low temperatures. a) Two-dimensional map of magnetoresistance as a function of gate voltage and magnetic field applied perpendicular to the sample at 100 mK. The logarithmic color scale indicates the linear resistance. The lower critical field H_{c1} is given by the white line, the blue line indicates the upper critical field H_{c2} and the black dotted line traces the Dirac point V_D, (see text) b) individual magnetoresistance curves for various gate voltages on the hole side of the Dirac point as labeled showing the smooth transition to the normal state.

are not free to move. Only when the number of vortices exceeds the number of pinning sites are the vortices free to move and the critical current goes to zero. This is the lower critical field for the sample, H_{c1}. The second effect of the magnetic field is to break the Cooper pairs and destroy superconductivity entirely. At this field, the sample will retain its normal state resistance. This is the upper critical field H_{c2} of the sample.

In figure 2.14, we display a two-dimensional map of linear differential resistance versus gate voltage and applied magnetic field. The lower critical field (H_{c1}) is identified as the field where a finite resistance first appears and the upper critical field (H_{c2}) is identified as the field where the resistance attains its same value as above the superconducting transition at 6 K. This map bears a qualitative similarity to the map of differential resistance as a function of gate voltage and bias current (figure 2.13). The lower critical field has 'V' shape with a minimum value at a gate voltage of +29 V which agrees with the minimum gate voltage for the critical current in figure 2.13. Above the lower critical field, the point of maximum resistance moves to more negative gate voltages similar to what was seen when increasing the bias current across the 'steps' in figure 2.13. Finally, the upper critical field shows a minimum at +12 V in agreement with the normal state properties of the device. In contrast to the bias current data, the resistance does not show discontinuous jumps as the field is increased.

This data can be qualitatively analyzed using the model discussed in the previous section of an array of randomly distributed Josephson junctions. In the case of the magnetic field, the critical current through a junction depends sensitively on the flux threading the area of junction. In figure 2.15 we show the behavior of the critical current for a gate potential near

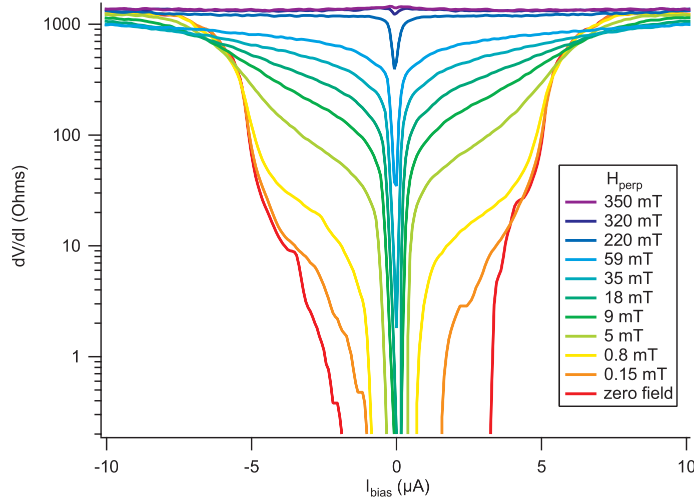

Figure 2.15: Critical currents and nonlinear resistance as a function of perpendicular magnetic field. Differential resistance on a logarithmic scale as a function of bias current for increasing magnetic fields perpendicular to the sheet at 100 mK and $V_g = +12$ V (V_D).

the Dirac point illustrating this sensitive dependence on applied field.

2.4.3 High-Magnetic Field Effects and Splitting of the Dirac Point

In magnetic fields above H_{c2} all of the Cooper pairs are broken and the material should display magnetoresistance characteristic of the normal-state hybrid material. However, at the lowest temperatures we observe a new effect; the charge neutrality point where the resistance is maximum splits into two separate peaks whose splitting and magnitude increase with increasing field. This is illustrated in the two-dimensional map of resistance shown in figure 2.16 a). Individual gate voltage traces at different magnetic fields shown in figure 2.16 b) clearly illustrate the splitting and 'dip' at the low field Dirac point. The temperature dependence of this effect is illustrated in figure 2.16 c) which displays the magnitude of the splitting at 100 mK and 800 mK for an applied field of 5.72 T.

A similar splitting was observed in high mobility samples of intrinsic graphene[17] at low temperatures and high magnetic fields, where the splitting was attributed to a measurement artifact due to current induced heating under finite current bias. This explanation assumes that the magnetoresistance is highly temperature dependent and the constant current bias at high resistance causes self-heating which raises the sample temperature above the bath temperature. In Checkelsky et al's samples, the effect was present for ohmic dissipation greater than 10 pW. For our samples under the same conditions we are only dissipating 0.2 pW, which makes their explanation unlikely. They also find that the effect is suppressed by disorder, unlike our samples, where extreme disorder due to the islands is present.

Intriguingly, the splitting of the Dirac peak in high magnetic fields corresponds exactly to the splitting of the $|n| = 1$ Landau level in graphene[13]

$$E_{LL}(n) = \hbar v_F \times \text{sgn}(n)\sqrt{2e|n|B/\hbar} \tag{2.8}$$

which is shown as the grey lines in figure 2.16 a). Clearly, more work is needed to understand the exact origin of the splitting of the Dirac peak in high fields for Sn decorated graphene.

2.5 Conclusions and Future Work

We have demonstrated a simple method to produce a two-dimensional superconductor on a graphene substrate and tune the transition via an electrostatic gate. This allowed us to systematically tune the carrier density at fixed disorder. Although structurally inhomogeneous, this material behaved electronically as a weakly disordered two-dimensional superconductor. While we have probed the properties of this system using electron transport, the readily accessible interface allows application of a myriad of local characterization techniques such as scanning probe microscopy, optical spectroscopy, etc. This tunable superconducting material may find applications in bolometers for sensing applications or as an element in circuits for quantum information processing.

We expect arranging the islands into regular arrays or superlattices should lead to interesting frustration effects as a function of applied magnetic and electric fields[70, 57]. Work is currently ongoing to adapt these studies to patterned arrays of superconducting materials. Figure 2.17 displays recently fabricated cross structures using CVD graphene samples where a square unit cell of one micron dimensions and 50 nm gaps has been fabricated. Initial tests of such a device using Pd/Al as a continuous superconducting layer did not show signs of superconductivity possibly due to a poor interface. Will Gannett continues work of investigating the properties of these materials in magnetic fields and under applied microwave irradiation where giant Shapiro steps are expected.

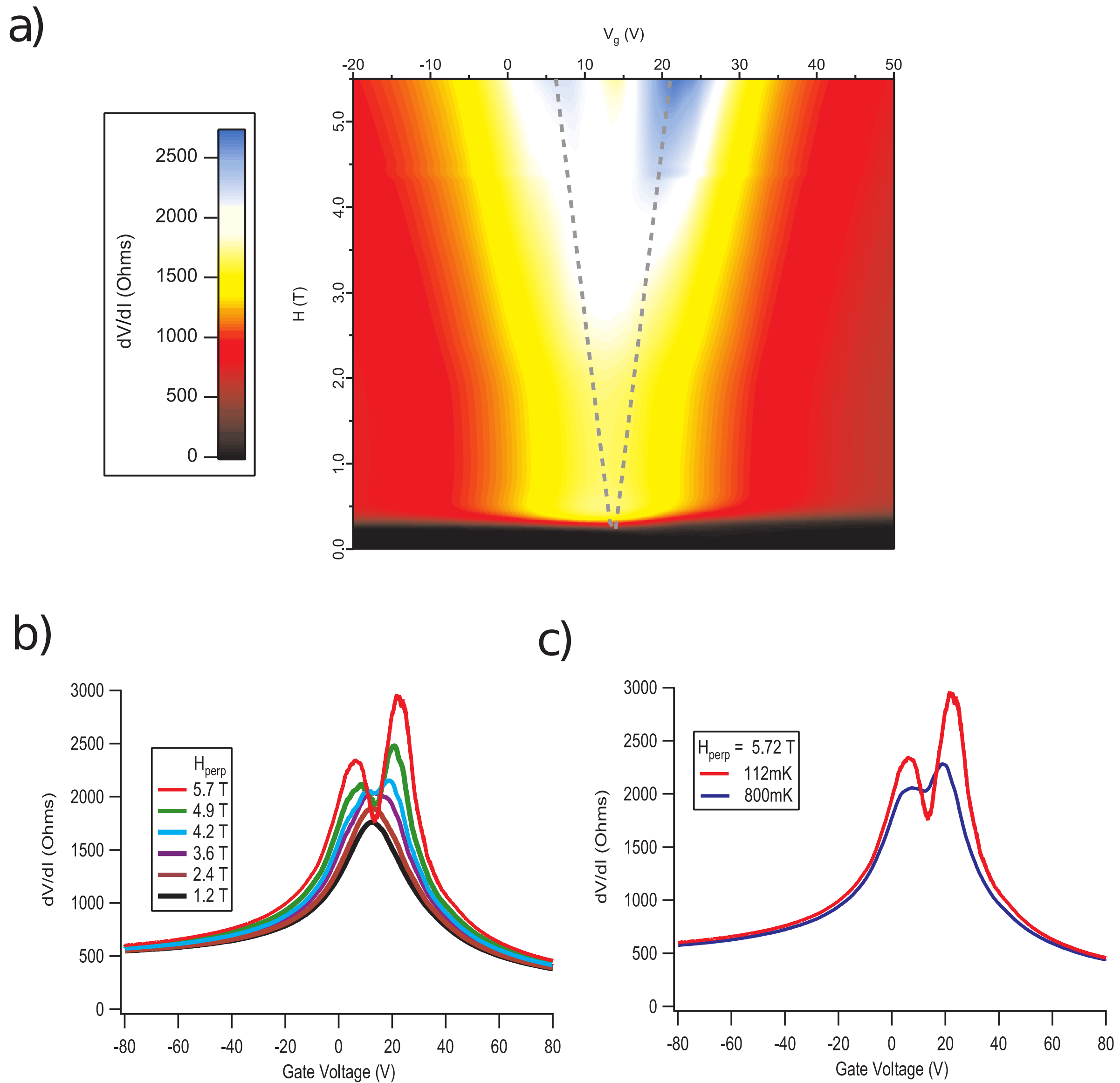

Figure 2.16: High field magnetoresistance at low temperatures and Dirac peak splitting. a) Two-dimensional map of magnetoresistance as a function of gate voltage and magnetic field applied perpendicular to the sample at 100 mK. The linear color scale indicates the low-bias linear resistance under 100 nA excitation at 17 Hz. The map covers the low field transition to the normal state and the high field splitting of the Dirac peak. The gray dotted lines trace out the spacing of the first Landau level. b) Differential resistance as a function of gate voltage at various magnetic fields from part (a) clearly showing the splitting of the Dirac peak in high fields. c) Temperature dependence of the Dirac peak splitting. Both curves were taken under an applied perpendicular magnetic field of 5.72 T.

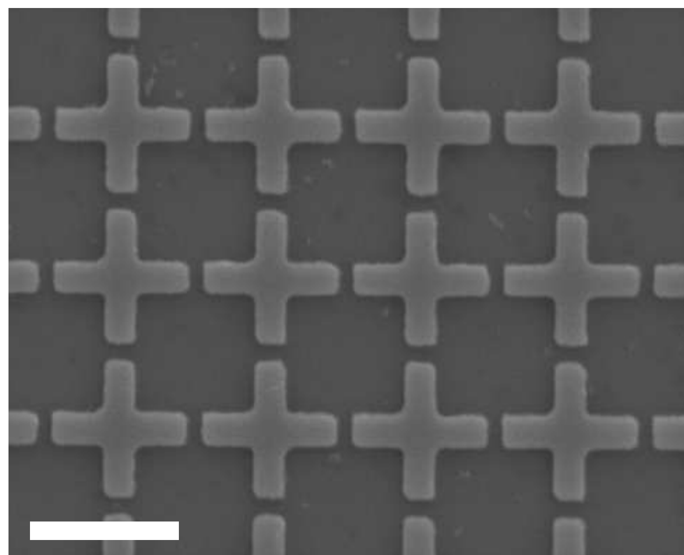

Figure 2.17: Patterned Josephson junction superlattice. SEM image of lifted off crosses. Scale bar is 1 micron.

Chapter 3

Other Two-Dimensional Hybrid Structures

3.1 Transport Through Superlattices of Ferromagnets

3.1.1 Overview of Theory and Device Structure

After investigation of superconductivity we turned our attention to the study of magnetic correlations coupled into the graphene sheet. However, initial investigations with the deposition of ferromagnetic materials (Fe, Ni, Co) on graphene revealed that they do not form clusters when deposited at room temperature due to their higher melting points. Therefore, we turned our attention to an artificially structured scheme similar to those responsible for giant magnetoresistance.

The giant magnetoresistance (GMR) effect has been developed into a core technology of hard disk drive storage and its discoverers were honored with the 2007 Nobel prize for their work[3]. GMR is a spin dependent resistance in combinations of ferromagnets and normal metals. Its simplest implementation consists of a trilayer spin valve where a normal metal is sandwiched between two ferromagnets as shown in figure 3.1. Due to the spin-dependent density of states in the ferromagnets there is a spin-dependent conductance associated with each spin orientation.

$$\sigma_\uparrow = en_\uparrow\mu \quad \sigma_\downarrow = en_\downarrow\mu \tag{3.1}$$

There are two independent configurations for the spin valve in figure 3.1. The first consists of the magnetization of the ferromagnets aligned and is referred to as the ferromagnetic (FM) configuration (b). The second configuration consists of the magnetization being anti-aligned and is referred to as the antiferromagnetic (aFM) configuration (c). Assuming that the initial current is unpolarized (ie. equal population of up and down spins) we can evaluate the resistance of the two configurations in a simple model of parallel resistances for the two spin channels.

$$R_{FM} = \frac{2R_HR_L}{R_H+R_L} \qquad R_{aFM} = \frac{R_H+R_L}{2} \tag{3.2}$$

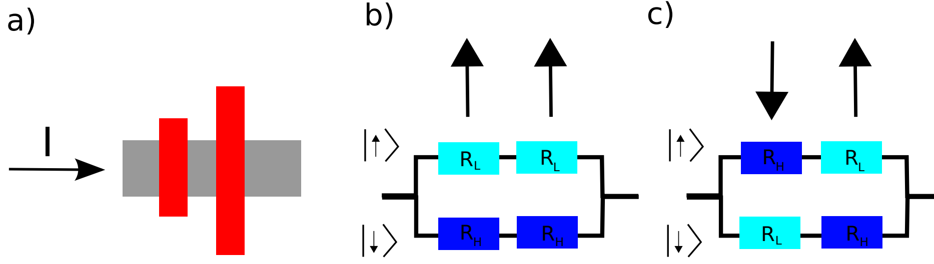

Figure 3.1: Device concept for magnetic transport measurements. Two ferromagnets with different coercive fields (red rectangles) are connected by a normal metal (grey) in our case this is the graphene sheet. The two possible configurations of the ferromagnets, aligned (FM) b) and anti-aligned (aFM) c) produced during a switching cycle lead to two different resistance states.

$$\frac{R_{FM}}{R_{aFM}} = \frac{4R_L/R_H}{(1 + R_L/R_H)^2} \tag{3.3}$$

where R_H is the high resistance associated with the conduction electrons spin being antialigned with the magnetic domain and R_L is the low resistance state associated with the conduction electron's spin being unaligned with magnetic domain. Thus, in the ferromagnetic orientation (FM) the resistance is expected to be lower than in the antiferromagnetic (aFM) state. The magnitude of the effect simply increases for subsequent stacked layers added in series. For this effect to be present the spin orientation of the electrons must be preserved between the ferromagnetic layers, therefore we require that the normal metal layer be thinner than the spin-flip scattering length, which has been determined for tunnel injected spin polarization to be $\simeq 1\mu$m in graphene[73].

Due to the labor intensiveness of this process a batch fabrication procedure needed to be developed. For this purpose chemical vapor deposited (CVD) graphene samples were used (see section A.2 for details). Briefly, devices were fabricated from CVD graphene deposited on oxidized wafers (285 nm SiO_2 on Si) that had been patterned with gold alignment marks and piranha cleaned. The CVD graphene was grown on Cu foils and transferred using the PMMA etching method. After transfer, electron beam lithography and etching were used to define a Hall bar type geometry. Subsequent e-beam lithography was used to deposit Ti/Au (5/35 nm) contacts. A final lithography step was used to pattern the superlattice structure and deposit Ni/Al (35/5 nm) bars. The Al capping layer is to prevent oxidation of the Ni bars. To achieve the high density fine features special attention to the proximity induced exposure was needed (see section A.3). A completed device is shown in figure 3.2.

3.1.2 Magnetoresistance in Parallel Fields

Samples were wirebonded in a configuration that allowed four-wire resistance measurements and loaded in a dilution refrigerator which was placed in a dewar equipped with

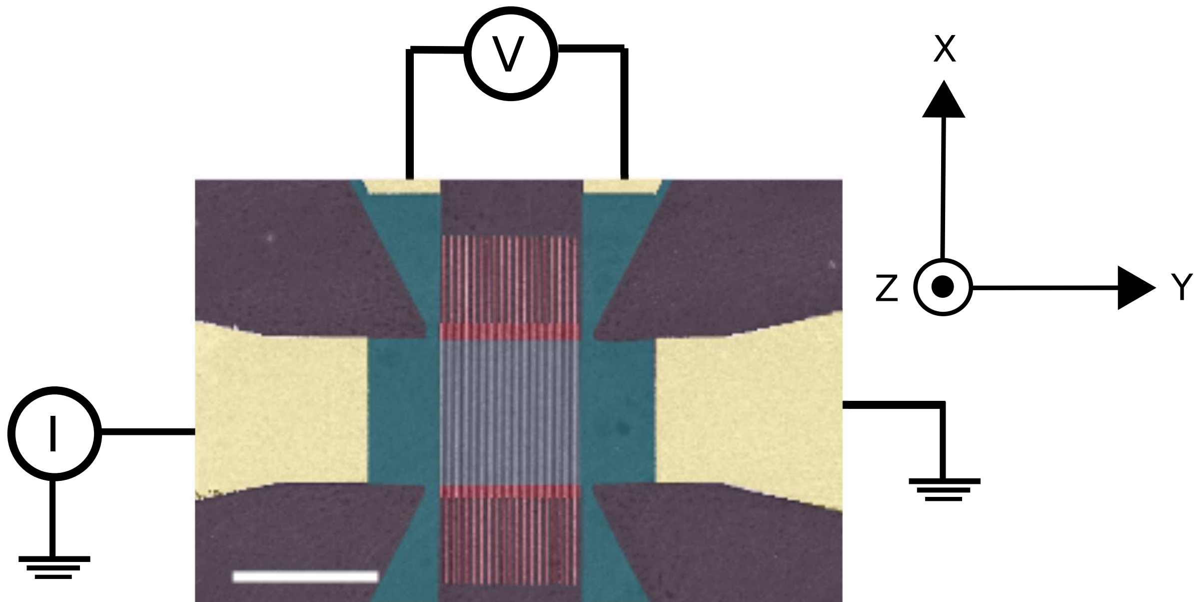

Figure 3.2: False color SEM image of magnetic superlattice device. Gold are the Ti/Au contacts, the graphene sheet is green and the nickel superlattice is red. The measurement setup is indicated and the coordinate system with reference to applied magnetic fields is given as well. Scale bar is ten microns.

superconducting magnets. One coil was oriented perpendicular to the plane of the sample (z direction in figure 3.2) and a split coil in the plane of the sample (x-y plane in figure 3.2). The orientation of the in-plane magnetic field could be controlled by rotating the refrigerator with respect to the coil. Measurements were made with respect to the two orthogonal directions (x and y in figure 3.2).

Figure 3.3 a) shows the resulting magnetoresistance at four different gate voltages of a device at 4 K with the applied field in the x-direction (perpendicular to the current flow). All of the curves display a sharp hysteretic dip at an applied field of ~ 50 mT. The magnitude of the dip increases as the zero-field resistance of the device increases. From the discussion above, we would expect a different behavior of the device. In particular, the device would be expected to exhibit a resistance maximum when the bars are anti-aligned in the aFM configuration at low fields and at high fields the resistance should decrease as the bars align.

Interestingly, when we apply a field in the y-direction (field parallel to the current) the magnetoresistance as shown in part b) of figure 3.3 displays a behavior much closer to what we would naively expect for the x-direction. The hysteretic magnetoresistance displays a rounded bump rather than a dip that occurs at a similar applied field (~ 50 mT) and once again is larger for gate voltages approaching the Dirac point (higher resistances).

Figure 3.4 plots the depth of the hysteretic dip when the field is applied in the x-direction as well as the height of the bump when the field is applied in the y-direction in comparison with the resistance of the device in zero applied field. We can see a general trend that

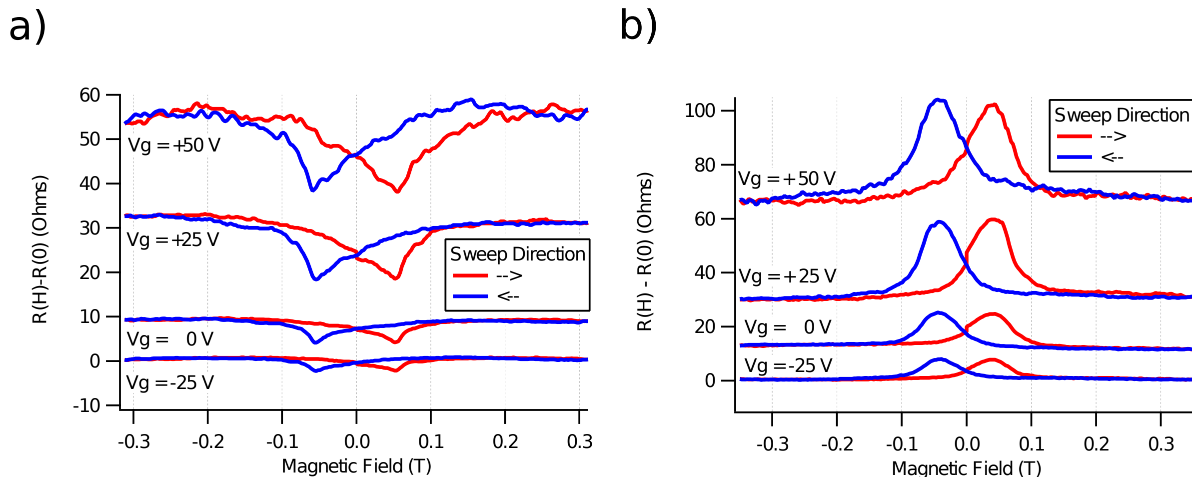

Figure 3.3: In-plane magnetoresistance at low temperatures. a) corresponds to fields in the x-direction and b) to fields in the y-direction (see figure 3.2) Each trace is the average of three sweeps of the magnetic field. Red traces are for increasing field sweeps and blue traces are for decreasing field sweeps. Curves are plotted as a difference from the zero-field value and offset vertically for visual clarity.

the magnitude of the hysteresis increases with increasing resistance. The relation of the sign of the magnetoresistance (negative for field perpendicular to current and positive for field parallel to current) bears resemblance to the anisotropic magnetoresistance seen in ferromagnetic materials, where the magnetoresistance is maximum for fields aligned with the current and minimum for fields perpendicular to the current[72].

3.1.3 Magnetoresistance in Perpendicular Fields

Weak Localization in Low Magnetic Fields

To further understand the unexpected in-plane magnetoresistance properties, we also studied the effect of magnetic fields oriented perpendicular to the substrate (z-direction). In figure 3.5 we see the magnetoconductance plotted for several different gate voltages after the sample had been fully polarized in the x-direction (ie. field of -300 mT applied and then lowered to zero before applying a perpendicular field. A field perpendicular to the graphene plane could affect the spin of the electrons by introducing a precession known as the Hanle effect[73], which would result in a periodic modulation of the resistance with field as the precession frequency matched the distance between bars.

However, we do not see such a modulation. Instead, the measured characteristics are much more reminiscent of weak localization. Theoretically graphene exhibits an unusual weak localization behavior due to the extra pseudospin (chiral) symmetry of the charge carriers[50].

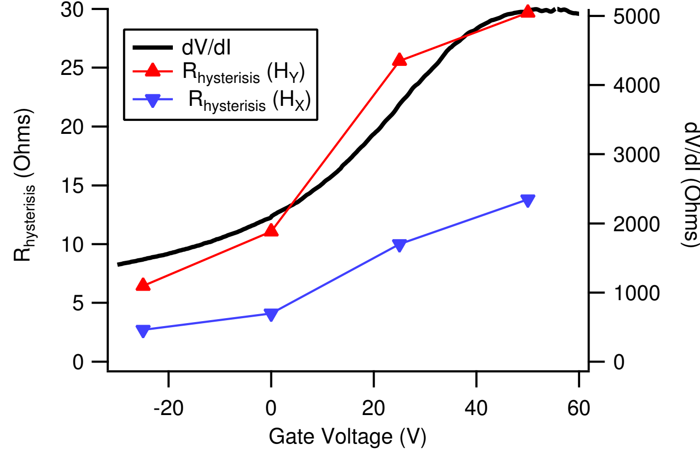

Figure 3.4: Summary of the in-plane magnetoresistance hysteresis and the zero-field resistance of the device. The solid black line is the zero applied magnetic field resistance of the device. The red triangles are the height of the hysteresis peaks for magnetic fields applied in the Y direction extracted from figure 3.3. The blue triangles are the height of dips in the resistance for fields applied in the X direction extracted from figure 3.3

$$\Delta\sigma(B) = \frac{e^2}{\pi h}\left[F\left(\frac{\tau_B^{-1}}{\tau_\phi^{-1}}\right) - F\left(\frac{\tau_B^{-1}}{\tau_\phi^{-1} + 2\tau_i^{-1}}\right) - 2F\left(\frac{\tau_B^{-1}}{\tau_\phi^{-1} + \tau_i^{-1} + \tau_*^{-1}}\right)\right] \tag{3.4}$$

where $F(z) = \ln(z) + \phi(1/2 + z^{-1})$, $\phi(1/2 + z^{-1})$ is the Digamma function, $\tau_B^{-1} = 4eDB/\hbar$, D is the electronic diffusion constant, τ_ϕ^{-1} is the phase breaking rate, τ_i^{-1} is the intervalley scattering rate and τ_*^{-1} is the scattering rate from chirality breaking defects and trigonal warping. The first term is a a weak localization term, while the second is an anti-localization effect.

Using the diffusion constant measured via the field effect at zero applied field $D = v_F \ell_{mfp}/2$ we can extract the various scattering rates from the measured magnetoresistance data in figure 3.5. As can be seen the agreement with theory is excellent and allows us confidence in the extracted scattering rates.

In figure 3.6 we plot the extracted scattering lengths (eg. $L_\phi = \sqrt{D\tau_\phi}$) as a function of gate voltage. The most notable feature of this graph is that the scattering length is essentially constant and limited to 125 nm. This is precisely the distance between our Ni bars and as one would expect for electrons scattering in the presence of magnetic impurities.

Splitting of the Dirac point in high magnetic fields

For higher applied fields the magnetoresistance increases and once again shows a splitting of the Dirac peak. In this case, the splitting is qualitatively different than the Sn coated samples. For Ni bar coated samples, the original Dirac peak does not shift at all, but a ‘satellite’ peak appears at a more positive gate voltage and increasingly becomes more

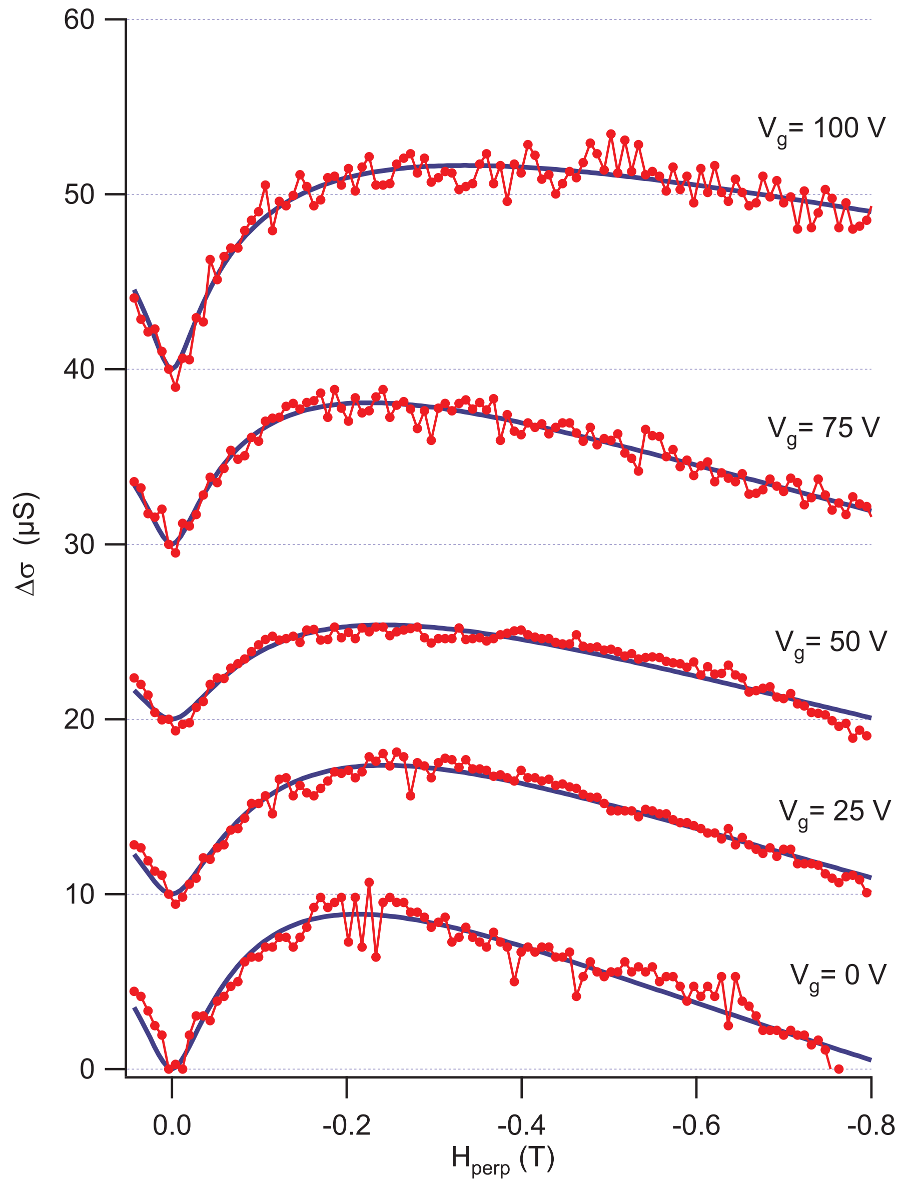

Figure 3.5: Low-field perpendicular magnetoconductance $\Delta\sigma = \sigma(B) - \sigma(0)$ of the device at 4.2 K for various gate voltages. Red dots are experimental data and blue lines are fits to the weak localization formula (eq. 3.4). The curves are offset vertically by 10 μS for clarity.

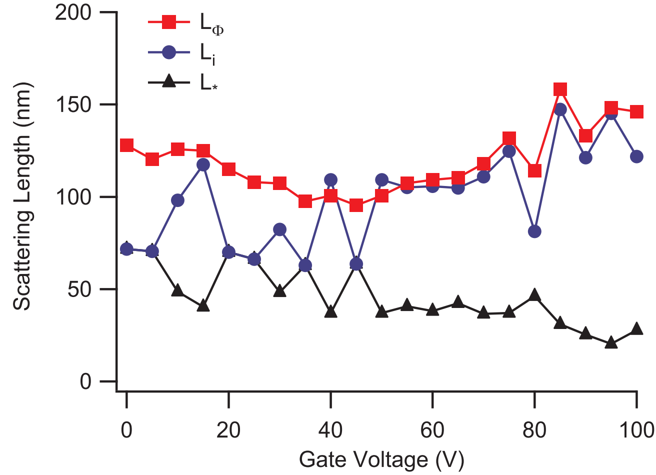

Figure 3.6: Scattering lengths as a function of gate voltage at 4.2 K using the fits to equation 3.4 extracted from the weak localization data presented in figure 3.5.

resistive until it is larger than the original peak. The splitting of this peak (ΔV = 30 V) corresponds closely to the inferred doping difference between the uncoated and Ni-coated graphene. Inverting equation 2.2 we see that this peak occurs at a value corresponding to $\Phi_M = 5.62$ eV, which is close to the value for Ni $\Phi_{Ni} = 5.47$ eV. A simple model for this system is strips of intrinsic graphene and Ni-coated graphene (doped to a higher positive gate voltage) in series, with a stronger magnetoresistance for the Ni-coated graphene. This corresponds exactly to our produced geometry.

3.1.4 Magnetic Force Microscopy Characterization of Magnetic Configuration

To gain a better insight into the somewhat mysterious transport properties observed above, we attempted to correlate the measured transport properties with the magnetic structure of the sample. To measure the magnetic configuration of the sample we used scanning magnetic force microscopy (MFM) to simultaneously measure topographic and magnetic information. We attempted to prepare the sample in the aFM configuration before measurement with the MFM by taking it through a minor loop. The sample was fully polarized to -300 mT in the x-direction then ramped to +50 mT (the apparent switching field) and finally brought to 0 mT. From the measured transport properties, this should place the sample in the aFM configuration (bottom of the dip in figure 3.3.

The sample was then loaded into a Veeco AFM chamber and measured using a standard magnetic probe with the assistance of Olivier Fruchart. In figure 3.8 we see the height and magnetic force images corresponding to the end of the Ni superlattice lines. The strong positive (blue) and negative (red) signals at the end of the lines indicate that our bars are indeed single domain samples and identification of these poles allows us to infer the

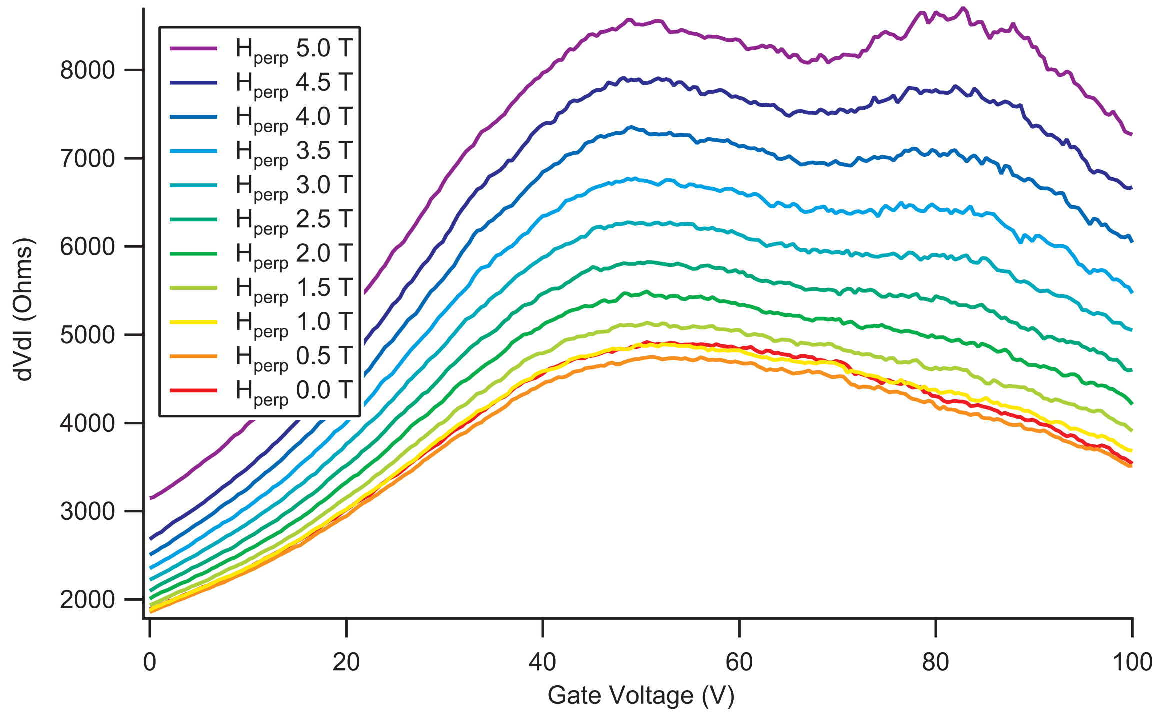

Figure 3.7: Appearance of a satellite Dirac peak in high magnetic fields. Perpendicular magnetoresistance as a function of gate voltage at 4.2 K for a range of fields. Note the appearance of a satellite Dirac peak at higher gate voltages as the perpendicular field is increased.

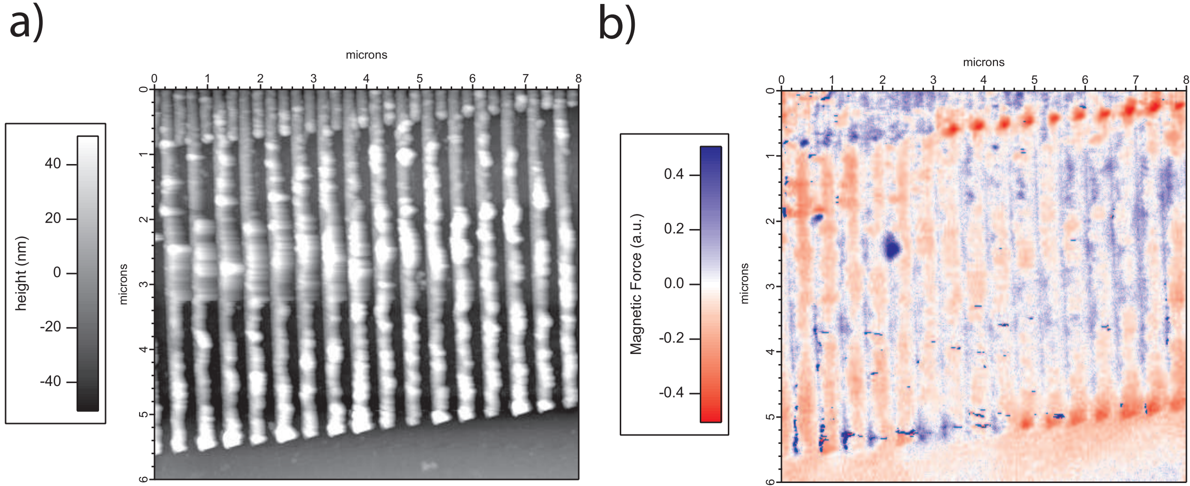

Figure 3.8: Magnetic force microscopy characterization of sample properties. a) Height image measured in tapping mode of the ends of the Ni bars. b) MFM image of the same area after completion of a minor loop in applied magnetic field. The signal is proportional to $\frac{\mathrm{d}^2B}{\mathrm{d}z^2}$ with red and blue indicating alternate magnetizations.

orientation of the bars. However, instead of the alternating alignment of the bars that was expected for the aFM configuration, we see blocks of aligned fingers of alternating orientation.

This interesting result deserves further study. In an noninteracting sample, we would expect the ground state to be randomly aligned orientations. And in an interacting sample, the simplest interaction would be the direct interaction which would produce an antiferromagnetic ground state with alternately aligned domains bars. From the blocks of aligned bars, it appears that the dominant interaction is ferromagnetic and there is a strong coupling between adjacent bars. The cause of this interaction could be mediated by the conduction electrons in graphene[64]. How the behavior of the unexpected behavior of the in-plane magnetoresistance is related to the microstructure also remains an open question. Will Gannett continues to study this system and possible design modifications [83] to determine the origin of the observed effects.

3.2 Non-local Resistance of Modified van der Pauw Disks

A further structure that we investigated was the inclusion of normal metals embedded in a graphene sheet. The geometry is that shown in figure 3.9. The van der Pauw geometry is a useful probe of materials since it allows the sheet resistance to be extracted without regard to sample dimensions using the standard formula.

$$e^{-\pi R_{12,34}/R_S} + e^{-\pi R_{23,41}/R_S} = 1 \tag{3.5}$$

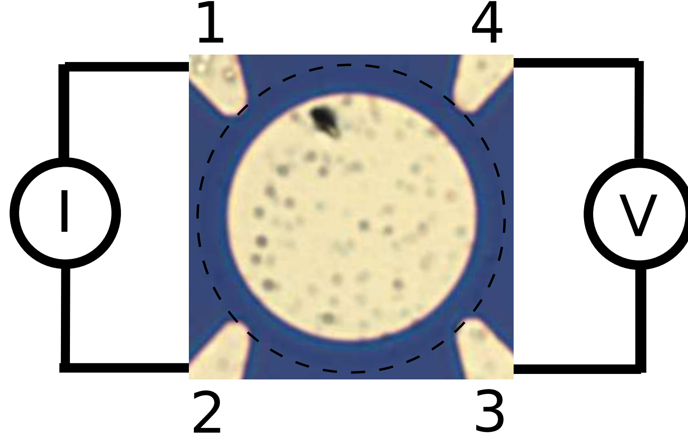

Figure 3.9: Optical image of a modified van der Pauw disk and associated setup. Four Ti/Au contacts touch the graphene sheet at equally spaced points and a large gold island is placed the center of the sheet. The extent of the graphene sheet is indicated by the dotted line. The non-local van der Pauw measurement setup is illustrated with current being sourced through one set of leads and the voltage being measured across the other set.

Normally, the van der Pauw method requires at least two independent measurements for determination of R_S, however in the case of symmetric samples the equation simplifies to

$$R_S = \frac{\pi R}{\ln(2)} \tag{3.6}$$

The transport properties were measured for devices fabricated as shown in figure 3.10. The measured resistance $R_{12,34}$ as well as the inferred sheet resistance R_S from equation 3.6 is shown. Two features are very prominent in this measurement. First, we note that the sheet resistance of the device is extremely low as expected for the high conductivity shunt present in the middle of the sheet. However, an unexpected feature is the presence of a dip in resistance at positive gate voltages, where we would expect to see a Dirac peak from previous measurements on CVD graphene (see section A.2).

Though unexpected, this dip was determined to be an artifact of the nonlocal measurement geometry. For the symmetric annular geometry of our devices one can calculate the non-local van der Pauw resistance using [79]

$$\rho(\alpha) = \frac{2}{\sigma_g \ln(2)} \sum_{n=1}^{\infty} \frac{(1+\alpha^{2n})\sigma_g + (1-\alpha^{2n})\sigma_0}{(1-\alpha^{2n})\sigma_g + (1+\alpha^{2n})\sigma_0} \frac{\cos(\frac{n\pi}{2}) - \cos(n\pi)}{n} \tag{3.7}$$

where σ_g is the sheet conductance of the graphene, σ_0 is the sheet conductance of the gold inclusion, and $\alpha = 25/30$ is the ratio of the diameter of the gold disk to the diameter of the graphene sheet. Using the known thickness of the gold (35 nm) and the conductivity of gold 4.55×10^7 S/m we can invert this formula to solve for the resistance of the graphene sheet from the measured transport properties. The extracted values of the graphene sheet resistance

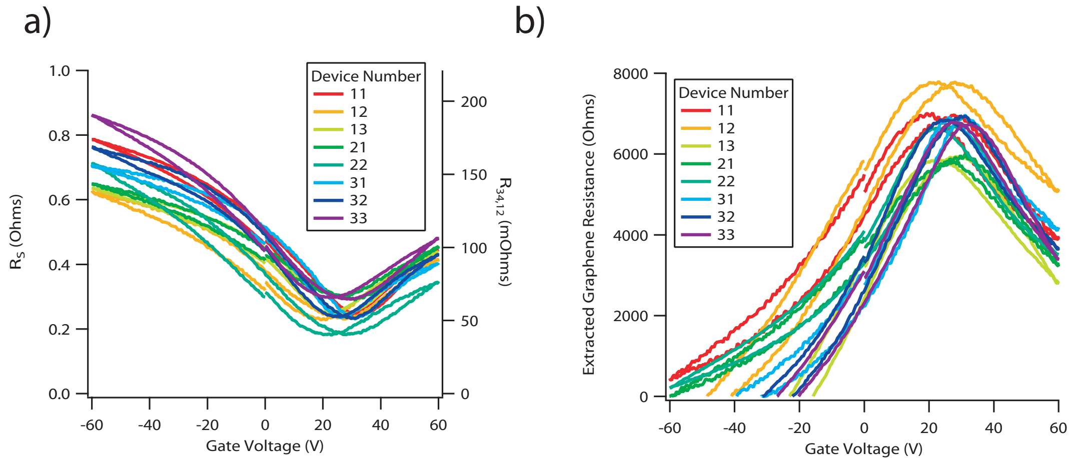

Figure 3.10: Electrical Transport of modified van der Pauw disk. a) Non-local resistance on the left axis and inferred van der Pauw resistivity on the right axis for several devices of the type shown in figure 3.9 fabricated from the same sheet. b) Extracted resistance of the graphene sheet using equation 3.7. Note the non-physical negative resistance values are likely due to an incorrect estimate of the gold sheet resistance.

are shown in figure 3.10 b). With no free parameters, this formula does an excellent job of reproducing sheet resistances similar to the values measured in rectangular sheets fabricated from CVD graphene (see section A.2).

The motivation of this measurement was the investigation of such structures for magnetic field sensing[66]. Problems with a leaky gate oxide after wire-bonding these devices did not permit detailed study of the magnetotransport in such structures, however using the known relations we can predict the expected behavior as a function of applied field and graphene sheet resistance [61]. The result is shown in figure 3.11. Recently, work on a similar structure fabricated using exfoliated graphene[59] has shown the promise of such structures for magnetic field sensing. Will Gannett continues to pursue the use of such structures and possible geometric enhancements of their magnetoresistance properties.

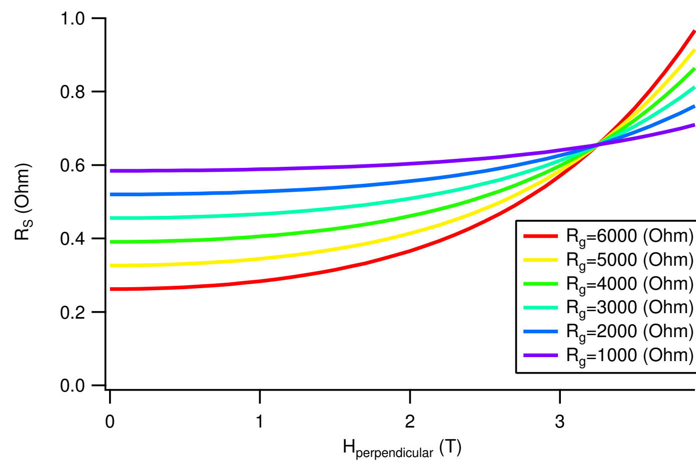

Figure 3.11: Predicted magnetic response of the modified van der Pauw disk using the theory of Poplavskyy [61] for a graphene mobility of 1000 cm^2 / (V s) and the sheet resistances as labeled.

Chapter 4

Hexagonal Boron Nitride: A Two-Dimensional Dielectric

Another key for manipulating electronic order in a field-effect device is the gate dielectric. Early development of the field effect transistor was hampered by the problem of surface states [5]. The problem of surface states still plagues organic electronics due to the difficulty interfacing molecules with inherently three-dimensional insulators [20]. Single-crystal boron nitride may be an interesting candidate for use as a gate dielectric in this context. The fact that it is inherently planar with an inert surface means that there will be no dangling bonds or surface states to affect charge carrier mobility at the interface.

In addition, it has been predicted that a bandgap should open in graphene devices with a boron nitride gate dielectric due to the differing dielectric environments of the A and B sublattices breaking the K/K' symmetry [32]. Previous studies of BN as a gate insulator had focused on large area polycrystalline films typically deposited via a plasma assisted chemical vapor deposition process[71]. These films may have extrinsic defects limiting their performance and the polycrystalline nature makes them unsuitable for application to bandgap opening in graphene. For these reasons we sought to characterize the dielectric properties of BN single crystals to evaluate their suitability as gate materials.

Hexagonal boron nitride is an isoelectronic compound to graphite where one of the carbon atoms in the basis has been replaced with boron and the other with nitrogen (see figure 4.1). However, it differs structurally from graphite in that the lattice stacking between layers is AA rather than the turbostratic AB stacking seen in graphite. This results in higher interlayer coupling due to the ionic nature of the bonds in BN. Being structurally so similar to graphite, BN shares many of the same physical properties such as high strength and high thermal conductivity. However, the ionic rather than covalent nature of the bond in boron nitride makes it a wide bandgap (5.5 eV) insulator.

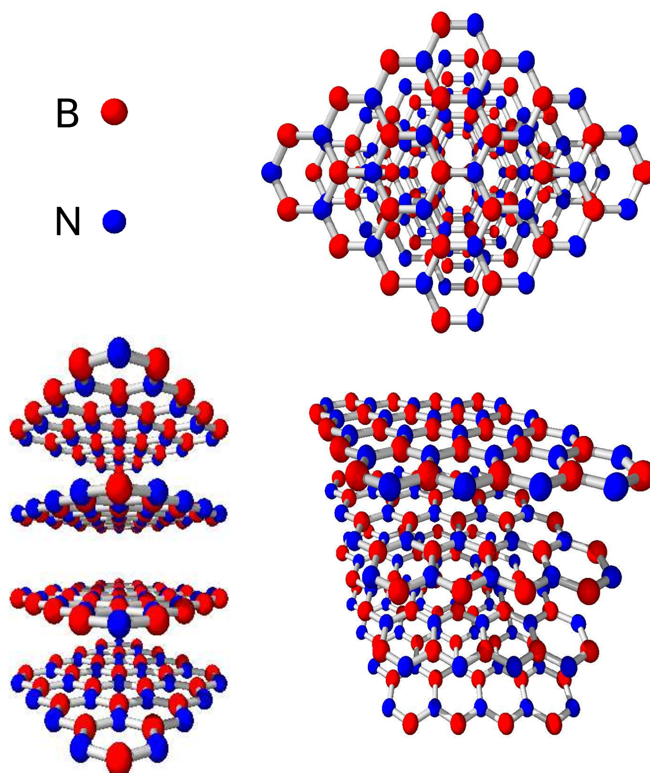

Figure 4.1: Rendering of the Boron Nitride lattice structure from three different perspectives illustrating the AA stacking order of the hexagonal lattice.

a)

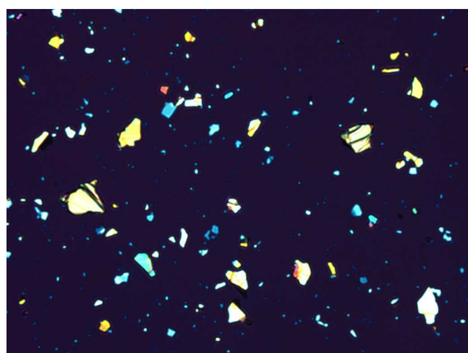

b)

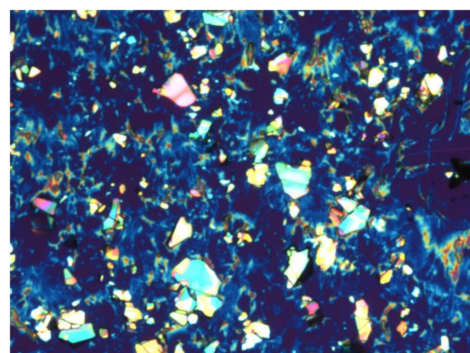

Figure 4.2: The samples were produced by removing the tape at room temperature (a) or 50 °C (b). More flakes are deposited during the hot peel (b), but also more tape residue is left behind. This tape residue can be dissolved in appropriate solvents such as acetone.

4.1 Dielectric Properties

4.1.1 Device Fabrication

Boron nitride is highly refractory and thus it has been notoriously difficult to synthesis high quality samples. Only recently has a CVD method based on precipitation from a supersaturated Ni-Mo alloy produced large high quality crystals suitable for optical studies[46]. However, large quantities of microcrystallites are routinely produced industrially and hot-pressed into high-temperature components. We sought to study whether these microcrystallites could be studied by similar methods employed for the study of graphene extracted from the crystallites of Kish graphite, with the goal of achieving high quality single crystal dielectrics.

Samples were produced in a method similar to those for graphene. We continued to use the 285 nm SiO_2 wafers due to their ready availability, though other thicknesses could increase the contrast[9]. Figure 4.2 shows an example region after exfoliating boron nitride onto it. In contrast to graphite, the boron nitride crystals show a rainbow of different colors due to reduced absorption and interference between the top and bottom surfaces. Due to the stronger interlayer interaction in BN it was more difficult to isolate thinner layers than with graphene[55].

4.1.2 Breakdown Strength

In order to produce single crystal samples suitable for electrical study we attempted to exfoliate the BN microcrystals onto previously defined gold electrodes. These electrodes were patterned with a high density in an interdigitated array using photolithography to achieve the highest possibility of a suitable flake being deposited over the electrodes. Once a suitable thin flake spanning just one of the electrodes was identified optically, standard electron beam lithography was used to make a top contact to the boron nitride and complete a parallel plate capacitor. A completed device is shown in figure 4.3.

To characterize the device, AFM was used to determine the thickness of the flake as 40.2 nm and standard electrical measurements were performed in a room temperature probe station using a Keithley 2400 source meter as a voltage source. Ideally, the two parameters most important for characterizing the strength of a gate dielectric are the dielectric constant k and the breakdown field E_b. Their product determines the maximum polarization (charge density per area) achievable at the interface of a FET device via the relation

$$P_{max} = k\epsilon_0 E_b = 5.5 \times 10^{11} \frac{kE_b}{\mathrm{MV/cm}} \quad (e/\mathrm{cm}^2) \tag{4.1}$$

In principle the parallel plate capacitor geometry should allow one to extract both k and E_b by measuring the capacitance C and the breakdown voltage V_b using

$$k = \frac{Cd}{\epsilon_0 A} \quad \text{and} \quad E_b = \frac{V_b}{d} \tag{4.2}$$

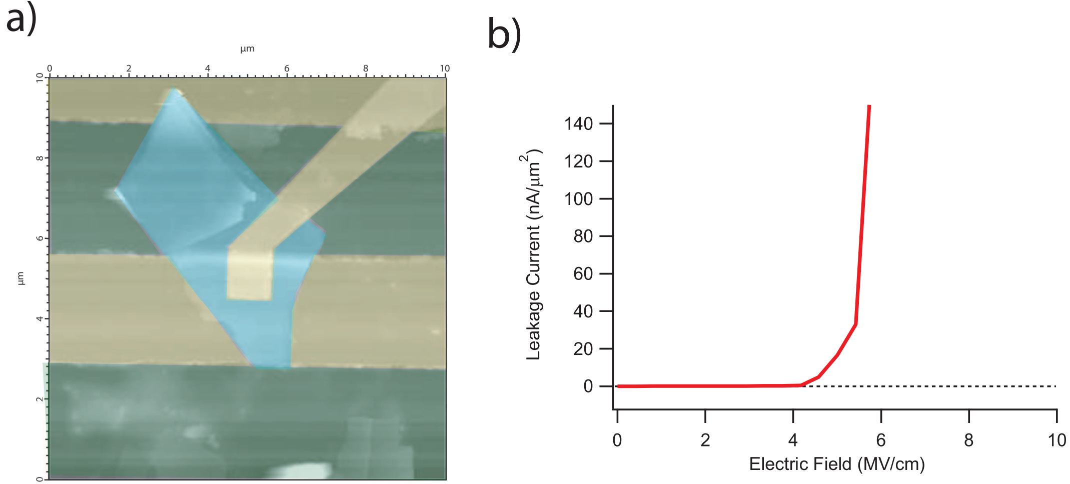

Figure 4.3: Electrical breakdown of a BN single crystal. a) False color AFM image of the connected hBN flake (blue) with contacts (gold) and SiO_2 substrate (green) used to extract the thickness of the flake. b) Breakdown of the single BN microcrystal under an applied voltage indicating $E_b = 4.2$ MV/cm.

where d in the thickness of the parallel plate capacitor and A is the area. Unfortunately, for our devices the capacitance of the BN flake is also in parallel with a much larger parasitic capacitance ($C_{par} =$ in agreement with the geometric area of the contact pads and SiO_2 thickness.) between the electrodes and the Si substrate, which prevents direct measurement of the capacitance due to the BN and independent determination of the dielectric constant.

We perform DC electrical measurements to determine the breakdown voltage of our flake. Figure 4.3 shows the measured current versus voltage characteristics for this device. From the inferred breakdown voltage and thickness we extract a breakdown field of 4.2 MV/cm, which gives a maximum polarization of $1.6 \times 10^{13}\ e/\mathrm{cm}^2$

Using general arguments, one expects the breakdown of a dielectric to occur at lower fields for higher k materials since higher k implies that the bonds are more easily polarized and thus broken[51]. A particularly simple thermochemical model for dielectric breakdown has been developed[51]. The empirical relation is given by

$$E_b = \frac{E_b^0}{k^{-0.59}} \tag{4.3}$$

with $E_b^0 = 26.2$ MV/cm. Which implies a maximum empirical polarization is given by[51]

$$P_{max} = P_0 k^{0.41} \tag{4.4}$$

with $P_0 = 1.4 \times 10^{13}\ e/\mathrm{cm}^2$. Known materials fall along this curve very well as shown in figure 4.4. When we add our BN sample to this list we see that it falls below the expected curve. Thus, BN offers no benefits in terms of increasing the maximum induced charge density in field effect devices. For turbostratic BN (mis-stacked AB instead of AA) this

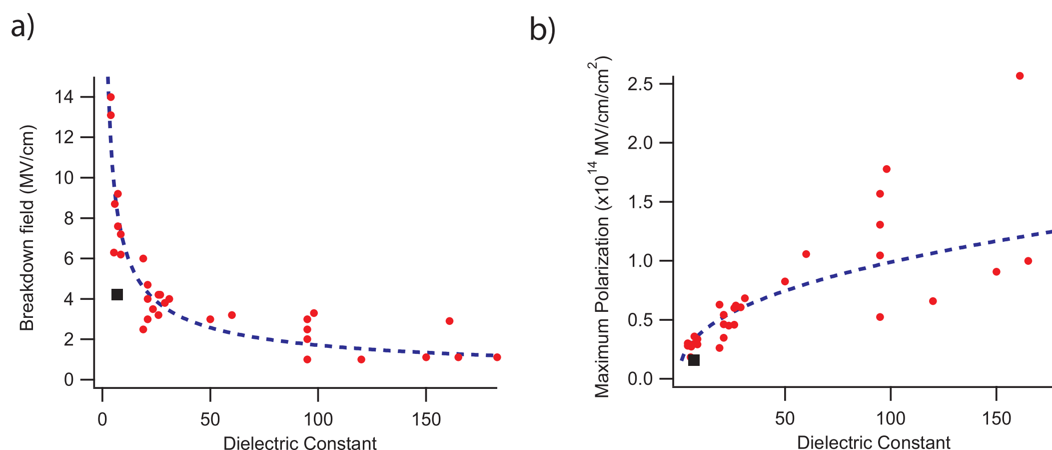

Figure 4.4: Electrical breakdown characteristics of dielectric materials. a) Experimental breakdown field of hBN (black square) compared to other dielectric materials (red circles) and the empirical relation equation 4.3 b) Identical data converted to maximum polarization values

model gives a breakdown voltage of 9 MV/cm falling directly on the empirical relation. The cause of the lower breakdown field in our samples may be due to defects which were also influencing the optical properties discussed above.

Recent work using solid polymer electrolytes[75] and room temperature ionic liquids[81] however has led to observation of the superconductor-insulator-transition to be studied in FET devices. It seems likely that these approaches are most promising for continued study of field-effect induced phase transitions. However, boron nitride's inert surface may yet prove useful in organic electronics or graphene based devices where it has the potential to open a bandgap due to arguments mentioned above. Work on using BN as a gate dielectric in these contexts continues to be pursued in the Zettl group by Will Gannett, Will Regan and Michael Rousseas.

Part II

Energy Applications of sp-2 Bonded Materials

Chapter 5

Hydrogen Storage

5.1 Motivation and Types of Storage

The majority of transportation in the world is powered by the chemical oxidation (burning) of fossil fuel, specifically oil . Total worldwide oil demand was 84 million barrels per day in 2006 and is expected to grow 40% by 2050[39]. At the same time, known reserves of fossil fuels are a finite resource and thus we will eventually run out of oil to be pumped out of the ground. Compounding this problem is the phenomenon of diminishing production known as peak oil[39], which indicates that total worldwide production capacity has already or will soon start diminishing as reserves become more difficult to locate and extract. The loss of fossil fuels and the cheap transportation they provide may be viewed as beneficial to the environment by some, but will have an enormous negative impact on the world economy. Clearly an urgent motivation exists to find an effective replacement form of energy storage to power the transportation sector of the economy.

One possible energy storage medium championed by the Bush administration is hydrogen, which could be converted to energy either in fuel cells or modified internal combustion engines. Environmentally, hydrogen holds appeal since its oxidization simply produces H_2O rather than environmental pollutants such as CO_2 associated with burning of hydrocarbons. However, hydrogen has some serious drawbacks to its use as a transportation fuel. Hydrogen is a dilute gas at standard conditions and thus the volumetric energy density is extremely low. Hydrogen is the lightest element and has an extremely high gravimetric energy density. However due to technical considerations of providing a sufficiently robust storage vessel, a hydrogen storage systems' total gravimetric energy density is unacceptably low. As such, the Department of Energy has outlined a series of hydrogen storage benchmarks (see table 5.1) with the goal of producing a viable hydrogen storage system for transportation purposes.

The challenge is to find materials that will store hydrogen efficiently yet also permit its release under mild conditions. The currently leading proposals for such materials fall into two broad classes:

1. Chemisorbtion relies on the formation of compounds that store hydrogen in a chemical bond. The hope is that these bonds can then be readily broken, usually under mild heating, to release the stored hydrogen. Many of the proposed candidates in this class

Physical Property	Target Value
Hydrogen Storage (%weight)	9.0
Gravimetric Energy Density (kW-h/kg)	3.0
Volumetric Energy Density (kW-h/L)	2.7
Refueling Rate (kG H2 / min)	2.0
Cycle Life	1500
System Cost ($/kW-h)	2

Table 5.1: DOE Hydrogen Storage Targets for 2015.

meet the volumetric requirements, but fail on the gravimetric benchmark due to the incorporation of heavy transition metal elements or insufficiently fast kinetics.

2. Physisorption on the other hand relies on weak van der Waals bonding of hydrogen to surfaces. The effective storage capacity is then highly dependent on the available surface area for binding as well as the strength of binding. This technique allows easy release of hydrogen, however it suffers from the drawback that weak binding limits total capacity. We sought to address this problem by investigating the effects of surface modification on hydrogen binding affinity.

5.2 Theoretical Considerations for Physical Adsorption

Theoretical analysis has been undertaken to understand the factors currently limiting hydrogen storage in physisorption materials and to design optimal physisorption materials[8]. For deliver between a loading pressure P_2 and a delivery pressure P_1 at a fixed temperature T, the optimum heat of adsorption ΔH_{ads}^{opt} is given by[8]

$$\Delta H_{ads}^{opt} = T\Delta S^o + \frac{RT}{2}\ln\left(\frac{P_1 P_2}{P_0^2}\right) \tag{5.1}$$

Where ΔS^o is the entropy change relative to standard pressure P_0 and it is found that $\Delta S^o \approx -8R$ for a wide variety of adsorbents[8]. For loading at 30 Bar and dispensing at 1.5 Bar at 298 K equation 5.1 predicts that the optimum heat of adsorption is given by 15.1 kJ/mol.

Equation 5.1 can also be used to determine the optimum operating temperature for a material with a given heat of adsorption by solving for T

$$T_{opt} = \frac{\Delta H_{ads}}{\Delta S^o + (R/2)\ln(P_1 P_2/P_0^2)} \tag{5.2}$$

The prototypical physisorption material is activated carbon, known for both its extremely high surface area and low cost. For typical activated carbons, $\Delta H^{ads} = 5.8$ kJ/mol[8]

giving an optimal working temperature of 155 K, which is far too low for practical hydrogen storage systems. Theoretical attempts have been made to search for possible ways to increase the heat of adsorption and thus the binding of high-surface area activated carbons. One promising suggestion was to consider the isoelectronic compound activated boron nitride. Theoretical predictions indicate a modest increase in binding energy to 8.7 kJ/mol for pure hBN[41]. However defective BN is predicted to show much stronger biding affinities, Stone-Wales defects and B/N bond rotation are predicted to show binding energies of 9.6 and 12.5 kJ/mol respectively[65].

While, high surface area boron nitride materials such as BN nanotubes have been produced and evaluated for hydrogen storage applications[49], the enthalpy of adsorption has not been measured for these materials. This makes determination of their hydrogen storage suitability difficult since the available surface area and binding affinity have not been separately determined. We sought to investigate the predictions of increased hydrogen storage on defective BN materials by independently measuring available surface area and binding affinity.

5.3 Synthesis of Activated Boron-Carbon-Nitride (a-BCN) materials

High specific surface area activated boron nitride (a-BN) was produced by converting an activated carbon (a-C) template using the method developed by Han et al[34]. Since the substitution destroys some of the pore structure of the a-C starting material, it is important to begin with a high quality activated carbon for use as the template. Highly activated carbon (Maxsorb AC) was reacted with B_2O_3 powder at 1600 C in a tube furnace under a flowing nitrogen atmosphere for 60 minutes.

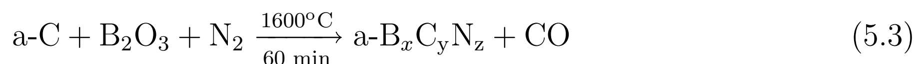

$$\text{a-C} + \text{B}_2\text{O}_3 + \text{N}_2 \xrightarrow[60\text{ min}]{1600^o\text{C}} \text{a-B}_x\text{C}_\text{y}\text{N}_\text{z} + \text{CO} \tag{5.3}$$

To complete the conversion and remove any remaining carbon, the product of this reaction was then held in a flow of 70 sccm N_2 and 10 sccm O_2at 650 C for 30 minutes[34], executing the following reaction.

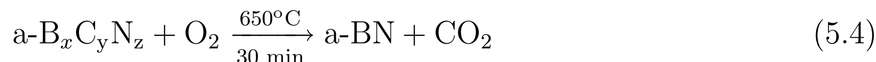

$$\text{a-B}_x\text{C}_\text{y}\text{N}_\text{z} + \text{O}_2 \xrightarrow[30\text{ min}]{650^o\text{C}} \text{a-BN} + \text{CO}_2 \tag{5.4}$$

Analysis of the resulting gray powder by SEM and TEM indicates that has similar morphology to the starting material, but charges significantly in the beam due to its insulating electronic characteristics. This is especially prominent in the fully converted sample which should be almost as insulating as hexagonal BN. Energy dispersive spectroscopy (EDS) indicates that the intermediate product a-$B_xC_yN_z$ contains significant carbon impurities while the final material consists of boron and nitrogen in roughly 1:1 ratio with residual impurities of B_2O_3 and trace amounts of carbon as shown in figure 5.1.

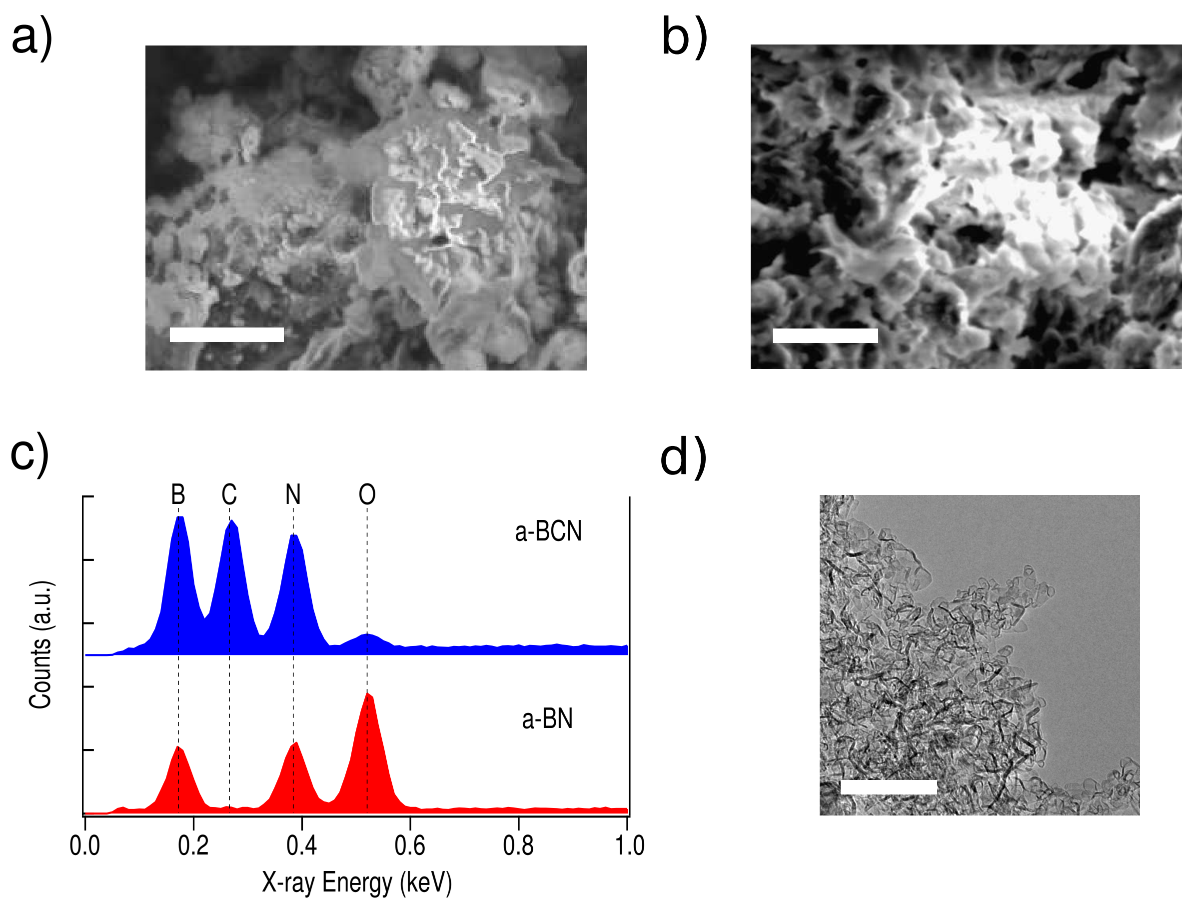

Figure 5.1: Characterization of the synthesized activated boron nitride. a) & b) SEM images of the BCN intermediate product and BN final product respectively. Scale bar is 5 microns. c) EDS spectra of the intermediate and final product showing conversion of the carbon to BCN and BN with residual oxide impurities. The positions of boron, carbon, nitrogen and oxygen K-lines are indicated. d) TEM image of the a-BN final product showing the crumpled sp-2 porous structure is maintained in the final material. Scale bar is 100 nm

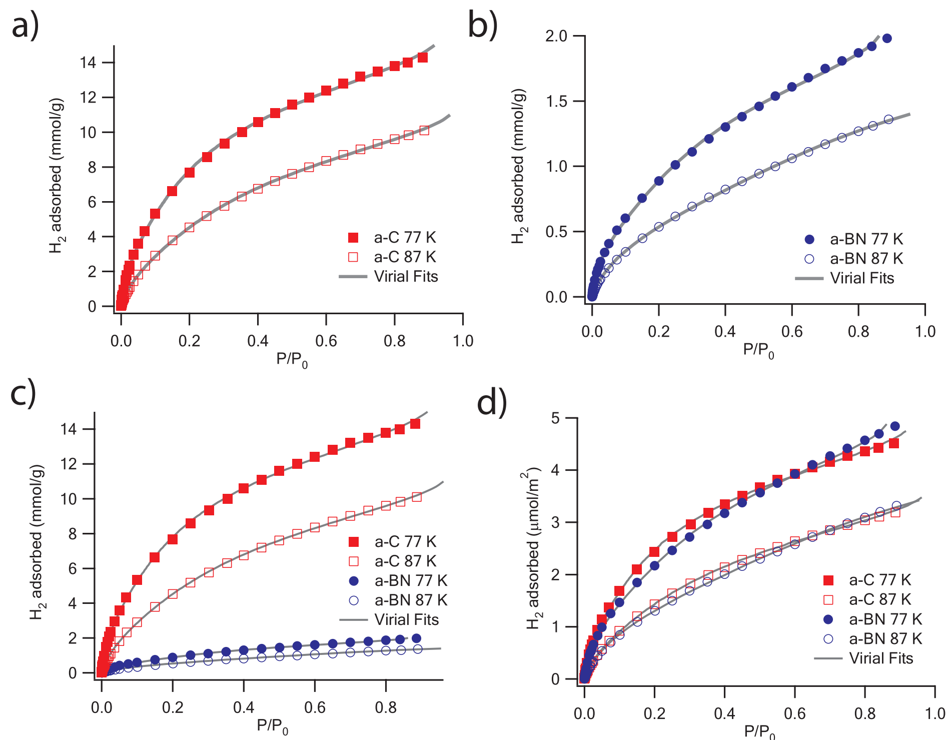

Figure 5.2: Comparison of hydrogen adsorption isotherms for a-C and a-BCN. Hydrogen adsorbed per unit mass for a-C (a) a-BN (b) at 77 and 87 K along with the viral fits using equation 5.5. c) same data as a) and b) on the same scale. d) data rescaled as a function of BET surface area instead of weight illustrating similar adsorption characteristics.

5.4 Hydrogen Absorption of Properties of a-C and a-BN

To evaluate the effect of the conversion reaction on hydrogen storage properties, we obtained hydrogen adsorption isotherms on a Micromeritics ASAP 2020 at 77 K (liquid nitrogen bath) and 87 K (liquid argon bath) for both the original a-C and the a-BN in addition to nitrogen isotherms at 77 K to obtain BET surface areas. Obtaining isotherms at different temperatures is crucial to determining the binding energy for adsorption. Knowing the enthalpy of adsorption along with the surface area data allows us to differentiate the effects of available binding sites and binding affinity, which is essential for rationally designing hydrogen storage materials.

As seen in figure 5.2, the amount of hydrogen adsorbed per mass decreased considerably from 2.85% to 0.397% after the conversion reaction. However, the conversion reaction is known to reduce the surface area of the material by etching some of the pores[34]. To account for this effect, we can normalize the absorption to the specific surface area obtained from nitrogen adsorption using the BET method[10]. The surface area of the material decreased from 3159 m^2/g for a-C to 410 m^2/g for a-BN. When the hydrogen adsorption is

Material	SA_{BET} (m^2/g)	H_2 ads (wt %)	H_2 ads ($\mu mol/m^2$)	ΔH_{ads} (kJ/mol)	T_{opt} (K)
a-C	3159	2.85	4.51	6.98	141
a-BN	410	0.397	4.84	7.43	150

Table 5.2: Comparison of adsorption properties for activated carbon and activated boron nitride. BET surface areas from N_2 adsorption at 77 K, H_2 adsorption at 77 K normalized by mass and also by BET surface area, ΔH_{ads} calculated via the virial fit (equation 5.6), T_{opt} calculated from equation 5.2

replotted with respect to the specific surface area in figure 5.2 d) both materials show similar adsorption characteristics.

5.4.1 Dominant Role of Brunauer-Emmett-Teller surface area

To analyze the hydrogen isotherms we use a virial expansion method[22], which is known to give quality results when extrapolated to the zero coverage limit. The isotherms are fit using the expansion given in equation 5.5.

$$\ln(P) = \ln(N) + \frac{1}{T}\sum_{i=0}^{m} a_i N^i + \sum_{i=0}^{n} b_i N^i \tag{5.5}$$

We find that $m = n = 4$ is a sufficient expansion to achieve quality fits of the experimental isotherms (gray lines in figure 5.2). Once the virial expansion coefficients a_i, b_i are obtained, one can use them to calculate the isoteric heat of absorption using the expression

$$\Delta H_{abs} = -R\sum_{i=0}^{m} a_i N^i \tag{5.6}$$

In figure 5.3, we plot the enthalpy of adsorption as a function of hydrogen coverage for both the a-C and a-BN materials. To make the comparison between materials we plot this as the physically relevant coverage of BET surface area instead of per unit mass. As predicted, the zero coverage enthalpy of adsorption for the a-BN increases slightly (7.43 kJ/mol) over the a-C starting material (6.98 kJ/mol). However this increase is much less than the value predicted by theory (8.7 kJ/mol), which may indicate that either the theory is overly optimistic or we have produced a material with a substantial portion of the 'wrong' type of defects, eg. residual carbon substitution in hBN is predicted to have lower binding of 2.9 kJ/mol[65].

5.5 Future Directions

The relevant properties of both the a-C starting material and a-BN are given in table 5.2. While, the total amount of hydrogen adsorbed decreased considerably, most of this is due

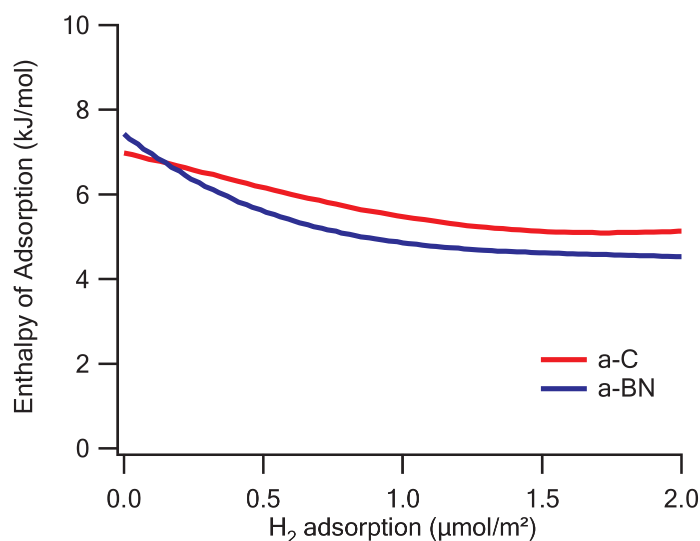

Figure 5.3: Enthalpy of Hydrogen absorption as a function of surface coverage for a-C (red) and a-BN (blue) calculated using the virial fits in figure 5.2 and the equation 5.6

to the decreased surface area in the a-BN material. The increased enthalpy of adsorption actually raises slightly the total amount of hydrogen adsorbed per unit area and the optimal working temperature. However, the measured properties still fall far below the DOE benchmark for transportation applications and the theoretical predictions. If more appropriate defect structures could be produced, eg. silicon substitution ($\Delta H_{theory} = 23.2$ kJ/mol [65]), the storage capacity may be raised further. It will be a considerable challenge to maintain high specific surface areas in these disordered materials. In the Zettl group, Kris Erickson continues for hydrogen storage.

Chapter 6

Nanotube Based Dye-Sensitized Solar Cells

6.1 History, Overview and Theory of Operation

In addition to the storage of energy using technologies such as hydrogen, it is also essential to produce energy using a renewable source. A possible technological solution is the production of electrical energy from the sun. Among the many proposed type of solar cells, the dye-sensitized cell is unique in that it attempts to mimic the natural process of photosynthesis. Briefly, a highly absorbent dye is coated on a high surface area semiconductor composed of a network of sintered TiO_2 nanoparticles which serves as one electrode. Photons absorbed by the dye molecule produce bound electron-hole pairs (excitons), which are split due to the potential at the dye semiconductor interface. The other charge moves through an iodine-based electrolyte to a transparent electrode made of TiO_2 completing the circuit[54].

Although dye sensitized solar cells have shown considerable promise and achieved efficiencies of >10%[54] they still have problems preventing their commercial adoption. In particular, the resistivity of the sintered nanoparticle network is an area that can be improved considerably. The simplest model for the complete circuit of a solar cell consists of a diode which produces a photocurrent J_{ph} along with a series resistance R_S and a shunt conductance G_{sh} in parallel with the active component. A simple circuit analysis allows one to obtain an equation relating the current density J and voltage V of the circuit

$$J = -J_{ph} + J_0 \left(e^{(V-JR_S)/V_T} - 1 \right) + (V - JR_S)G_{sh} \tag{6.1}$$

where J_{ph} is the photocurrent density, J_0 is the reverse bias saturation current density of the diode, $V_T = k_B T/e = 25.8$ mV is the thermal voltage at room temperature, R_S is the series resistivity and G_{sh} is the shunt conductance per area. Using this equation we can model the imperfections of the solar cell presented in figure 6.1 and fit $R_S = 0.027$ Ohm cm^2 and no shunt conductance the IV characteristics using (the black dotted line). We can compare this fit to the calculation of same circuit with the series resistance removed and obtain a theoretical efficiency of 5.3% (blue dashed curve), indicating that the series resistance is significantly hampering the device performance.

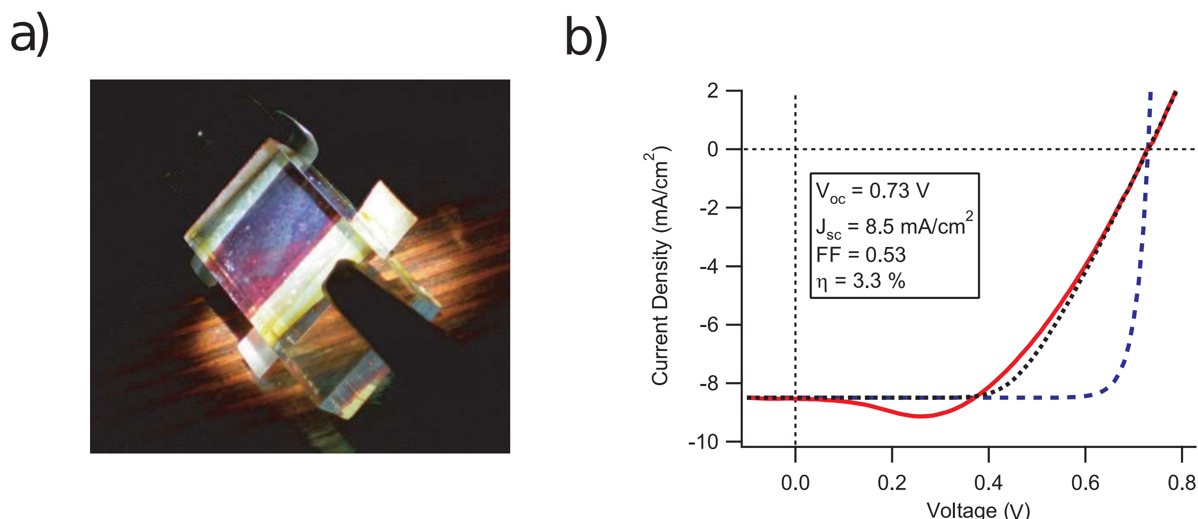

Figure 6.1: a) Photograph of a dye-sensitized solar cell fabricated by Bryan Chiang in the Zettl Lab. b) IV characteristics of the DSC under simulated AM1.5G illumination. The red solid line is experimental data. The dashed black line is a fit to the circuit model using equation 6.1 with $R_S = 0.027$ Ohm cm^2 and no shunt conductance. The dashed blue line is the same model with no series resistance $R_S = 0$ giving a theoretical efficiency of $\nu = 5.3\%$

Looking at figure 6.2 a) we can infer the cause of the series resistance is due to the poor conduction through the nanoparticle network[44]. To solve this problem one must maintain high surface areas of the titania necessary for efficient absorption and charge transfer, yet increase the conductivity of the resulting electrode. One possible solution is to use a nanotube forest with its associated high surface area and conductivity, but coated with a very thin layer of titania to adsorb the dye and forming the diode junction (figure 6.2 b)) as anticipated by other workers using nanowire arrays[47].

6.2 Atomic Layer Deposition of Titania on Nanotubes

In order to achieve the desired electrode geometry, we must develop a method of uniformly coating the nanotube electrode with titania. Atomic layer deposition (ALD) is a technique that allows precise control of deposited film thickness at the atomic scale. Figure 6.3 displays the ALD process using deposition of TiO_2 as a prototypical example. Conceptually, ALD can be viewed as a surface limited chemical vapor deposition reaction that is split into two complementary steps. The first precursor (A) is introduced into the chamber and completes a surface limited reaction. Any excess precursor A is purged from the chamber before introducing the second precursor (B). precursor B completes a surface limited reaction with the new surface formed by precursor A and then is purged from the chamber. One full cycle of this process produces one monolayer of deposited material. The process can be repeated N times to produce N layers of the desired material.

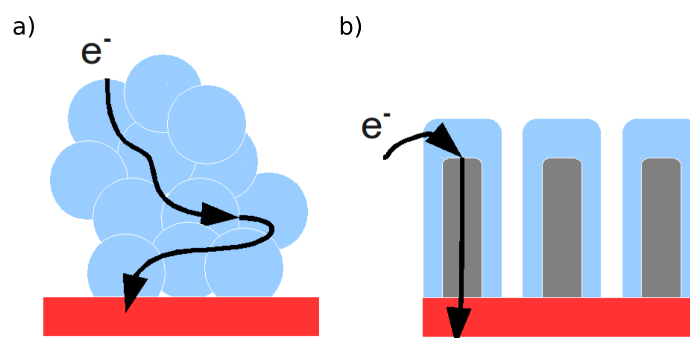

Figure 6.2: Charge conduction in dye-sensitized solar cell electrodes a) Charge transport in the nanoparticle network is torturous and results in high series resistance b) A nanotube array provides a high conductance pathway for charges generated in the TiO_2

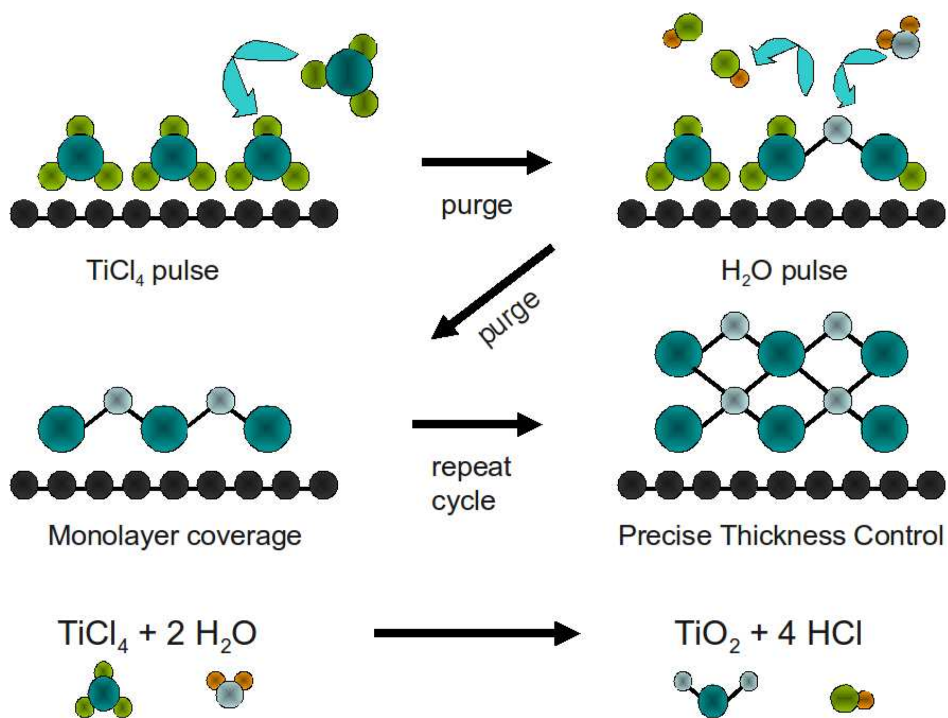

Figure 6.3: The ALD process cycle for deposition of TiO_2.

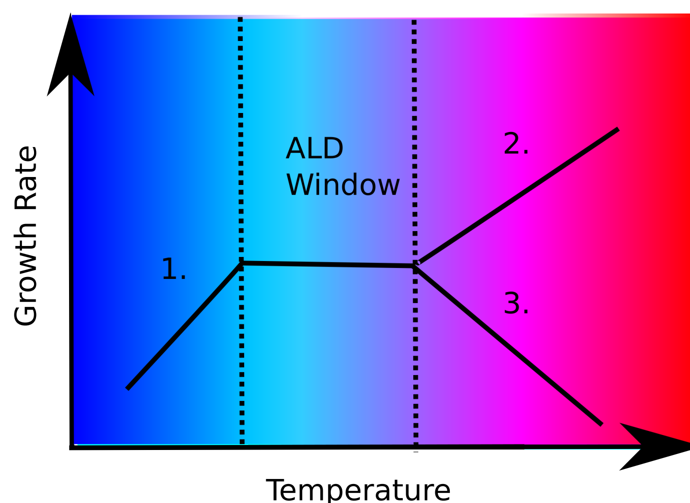

Figure 6.4: The "ALD window" for controlled layer-by-layer deposition. Percursor condensation on the surface at low temperatures results in uncontrolled multilayer deposition (1). At higher temperatures, reduced surface binding affinity limits coverage of precursors (2) or thermal decomposition produces uncontrolled chemical vapor deposition (3).

There are several key requirements to allow an ALD reaction to complete a controlled layer-by-layer deposition:

1. The precursors must not condense on the surface since this would prevent purging of excess precursor. This typically introduces a minimum temperature and maximum pressure for the reaction. In our system, we work at the fixed pressure of ~100 mTorr. So this becomes just a temperature constraint.

2. The precursors must either react or bind with the surface to produce a complete monolayer. This is important for the initial layer as subsequent layers do not encounter the original surface.

3. The materials must only react on the surface and not in the gas phase. The typical reaction that occurs in the gas phase is thermal decomposition of the precursors. This typically places another upper bound on the temperature to prevent precursor decomposition.

These three constraints serve to define an "ALD window" (see figure 6.4), which presents the temperature range where controllable layer-by-layer deposition is possible. Inside this window it is also possible that temperature can affect the crystalline structure of the deposited material [1].

Much of the work on ALD has been carried out on Si in the semiconductor industry in order to produce uniform thin high-k gate oxides for MOSFET applications. Si can easily be terminated with highly reactive hydroxl (OH) groups that will react with precursors to form an oxide such as HfO_2. Thus, constraint 2) listed above does not typically apply.

Unfortunately, for sp2-based materials the layered structure results in an inert surface that is not easily functionalized to produce a reactive surface. Therefore, constraint 2) is a dominant concern in these materials and it is constraint 3) which serves to limit the high temperature end of the ALD window.

For nanotubes and graphene, several approaches have been developed to confront this problem. One solution is to find a precursor that has sufficient binding affinity to produce monolayer coverage. Replacement of H_2O in standard oxide deposition recipes with NO_2 was shown to be an effective precursor with enhanced binding affinity [27]. Another possible solution is to use a seed molecule that has strong binding affinity and increased reactivity to produce the initial layer and proceed with standard ALD techniques subsequently. On nanotubes, pyrene-based molecules with hydroxl functionalities was shown to bind strongly via $\pi - \pi$ stacking and was sufficiently reactive for ALD due to the OH^- groups[78].

6.2.1 Effect of Temperature on Morphology and Coating Efficiency

Though our end goal was to coat dense nanotube forests with TiO_2 for use as electrodes, we initially sought to develop the coating process using arc-discharge produced multiwalled carbon nanotubes for characterization purposes. Samples were prepared from solutions of MWNT dissolved in IPA and drop coated onto lacey carbon TEM grids. These grids were then loaded into the sample chamber of a home built traveling-wave ALD reactor constructed by Alexandra Radenovic.

The system consists of a stainless steel tube furnace with nitrogen carrier gas at the inlet inlet connected to a roughing pump. Note that since some ALD byproducts (eg. HCl) are highly corrosive a cold trap was placed on the system to prevent damage to the pump. In general, the operating pressure of the system is ~100 mTorr. The liquid precursors (titanium tetrachloride, $TiCl_4$, and water, H_2O) are loaded into sealed stainless steel vessels. These vessels are connected to the chamber via stainless steel tubing with two solenoids at each end. Sequential opening and closing of the solenoids fills this tubing with precursor from the vapor pressure at room temperature of the liquid precursor. Thus the length of tubing serves as an aliquot for each cycle of the ALD process. A computer running LabView controlled the sequential opening and closing of solenoids with controlled timing of the dosing and purging steps. A purge time of 10 seconds was determined to be sufficient by observing the induced pressure spike and decay as the dosing step was initiated.

For initial characterization of the coating the system was pumped down and the temperature was allowed to stabilize at 120 °C for one hour before beginning the ALD cycles. After 200 cycles of deposition, the system was allowed to cool under vacuum and samples were loaded into a TEM for observation. The coated tubes displayed what appeared to be a uniform coating of amorphous material. To determine the elemental composition of this coating electron energy loss spectroscopy (EELS) and energy filtered imaging was performed. Figure 6.5 shows energy filtered images of a TiO_2 coated MWNT and a full EELS spectrum showing the energy loss peaks for carbon, titanium and nitrogen. Since $TiCl_4$ was used as a precursor, attempts were also made to observe Cl impurities, however no peak could be

detected. The energy filtered images clearly show a multiwalled carbon nanotube (diameter = 15.5 nm) sheathed in a titanium coating (thickness = 9.2 nm). This implies the rather slow coating rate of 0.05 nm per cycle. Analysis of the relative intensities of the Ti and O peaks indicates that the coating has a stoichiometry of 0.47 ± 0.07:1 as expected for TiO_2.

Our goal was to produce crystalline TiO_2 in the anatase phase for DSC based solar cells. From previous work on TiO_2 ALD it was shown that deposited films undergo an amorphous to anatase phase transition at 165 °C[1]. We performed several ALD depostions across this temperature boundary to determine the optimal conditions for coating the tubes with a crystalline coating. In figure 6.6, we show the effects of increasing temperature on the deposition of TiO_2 on MWNT.

We first note the change in coating efficiency as the temperature is increased. The lowest temperature (120 °C) was set to prevent condensation of the H_2O (ie. the lower bound of the ALD window). Coating at 120 °C produces a complete and uniform coverage, while already at 200 °C the coating has become discontinuous. The coating remains discontinuous at 300 °C, however a crystalline structure is now observed. At 400 °C only the amorphous carbon of the support grid is coated, while the MWNT are completely barren indicating that we have moved completely out of the ALD window due to decreased precursor-substrate binding affinity.

From these depositions, it appears that layer-by-layer deposition is only possible for the amorphous phase. However for efficient charge transport (band conduction versus hopping conduction) in a DSC, we would like to have a uniform coating of the crystalline anatase material. to achieve this goal we employed a technique that produced an interfacial seed layer (2 nm, 40 cycles) of amorphous TiO_2 deposited at 120 °C followed by deposition at 300 °C to produce a uniform coating of crystalline material (5 nm, 100 cycles). The results of this process are shown in figure 6.7. This process does indeed produce a uniform coating of the crystalline material which is determined to be anatase phase via selected area diffraction analysis.

6.3 Coating of Forests for Production of Solar Cells With Carbon Nanotube Electrodes

Now that the ALD process has been developed for deposition on isolated tubes, we turn to the deposition on nanotube forests and their incorporation into dye-sensitized solar cells. Forests grown on tantalum foil were placed in the ALD reactor and coated using the dual stage recipe presented above. In figure 6.8, we show the results and subsequent electron energy dispersive spectroscopy (EDS) analysis of such a forest. It appears that the sample has been coated very well by the dual stage process, resulting in a continuous uniform coating of TiO_2.

Solar cells were constructed out of such forests by Bryan Chiang using the same construction as the dye-sensitized cell presented above, with the nanotube electrode directly replacing the nanoparticle electrode. The performance characteristics of the best such cell are presented in figure 6.9. While the cell does produce power, it does not perform very

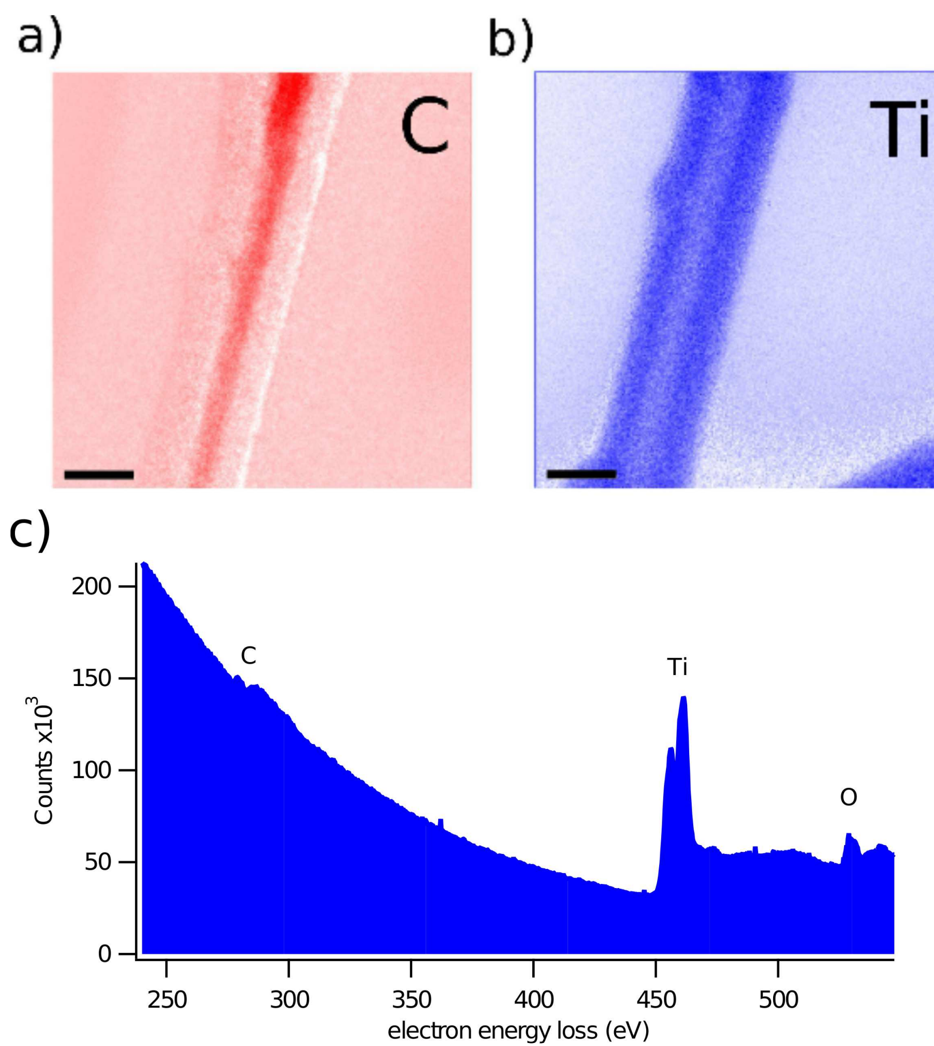

Figure 6.5: EELS Characterization of TiO_2 coated MWNT. Energy filtered imaging of the carbon peak (a) and titanium peak (b) for a TiO_2 coated MWNT. Scale bar is 20 nm. The full EELS spectrum is shown in (c) with the C, Ti, and O absorption marked.

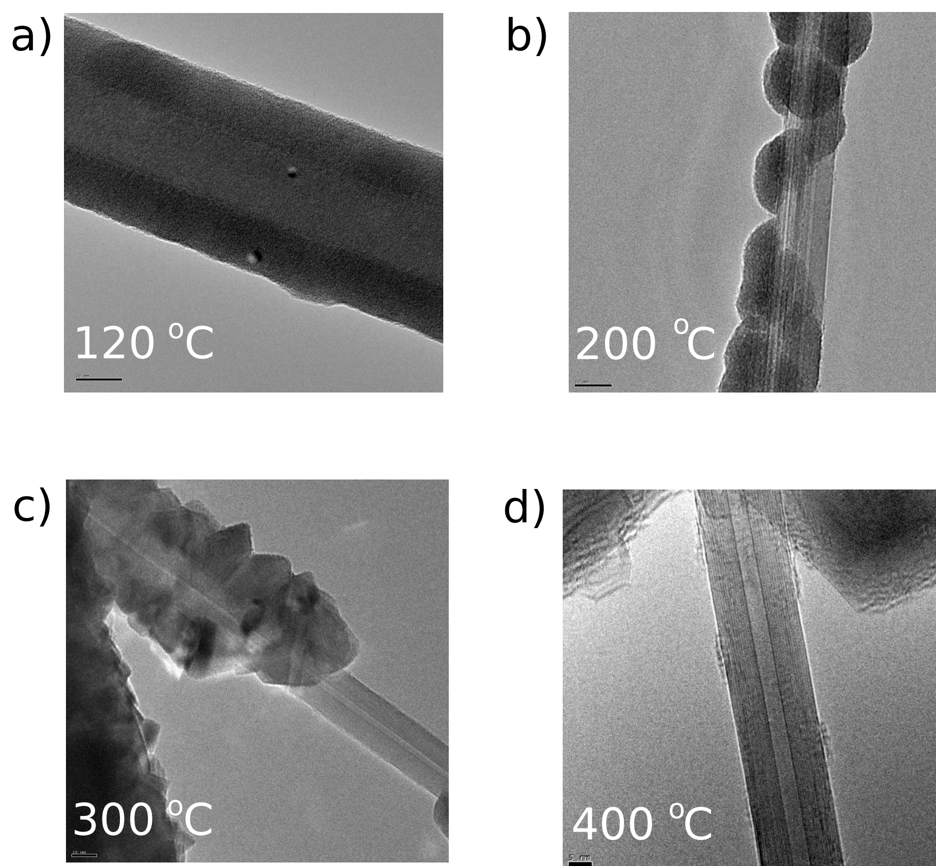

Figure 6.6: TEM images of MWNT coated with ALD for 200 cycles at 120 °C, 200 °C, 300 °oC, 400 °C (a-d) respectively.

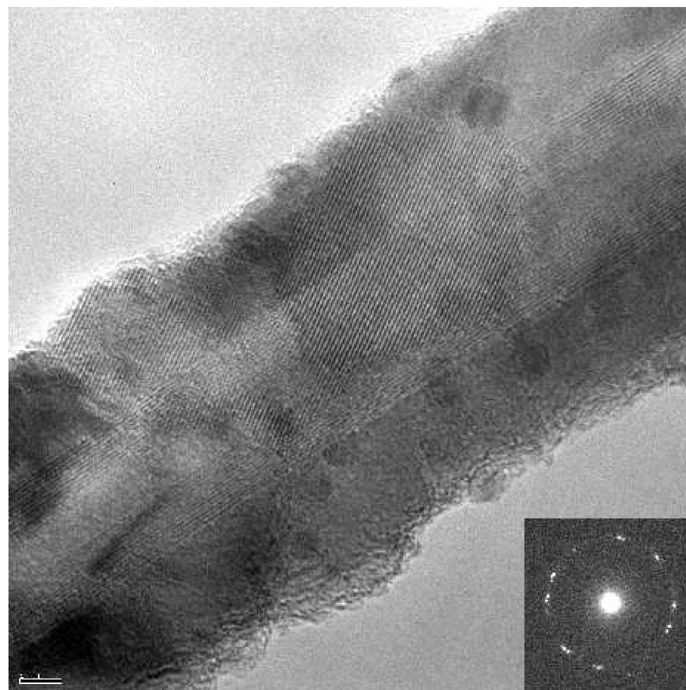

Figure 6.7: Dual Stage Coating Process. TEM image of the coating after an ALD deposition at 120 °C for 40 cycles followed by 100 cycles at 300 °C. Inset is a selected area diffraction pattern illustrating the polycrystalline anatase structure.

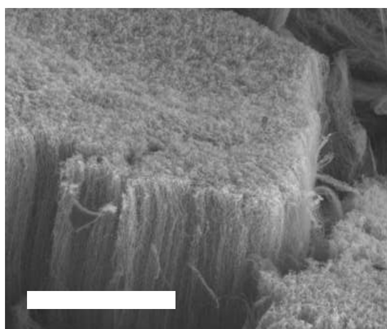

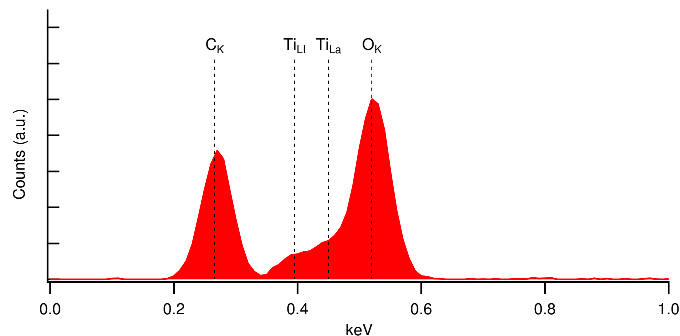

Figure 6.8: Nanotube forest coated by ALD TiO_2. a) SEM image of a coated forest. Scale bar is 20 microns b) EDS analysis of the coated forest with the relevant peaks labeled. Note that the Ti L peaks are much lower intensity than the C and O K peaks due to the lower cross section for excitation.

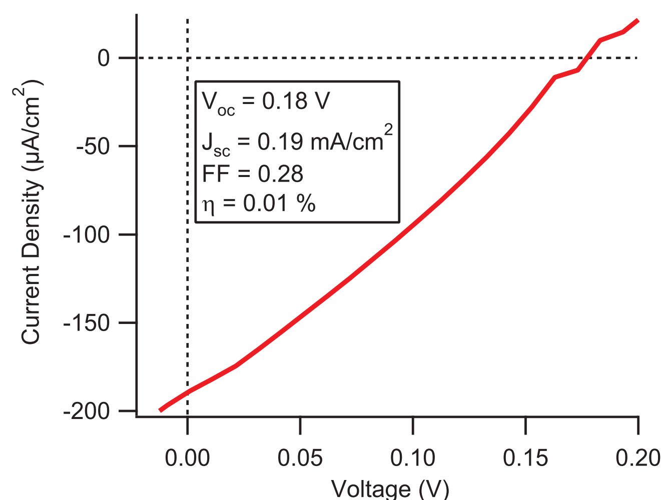

Figure 6.9: IV Characteristics of a DSC with a carbon nanotube electrode fabricated in the Zettl lab. Relevant performance parameters are listed.

well in comparison to the standard cell. Using the model presented in equation 6.1 we can analyze what is limiting this cell's performance. The finite slope at the short circuit current indicates that there is a significant shunt conductance $G_{sh} = 0.8$ S / cm^{-2} in this cell.

The cause of this shunt conductance is likely due to imperfect coating of the TiO_2 layer resulting in exposed areas of the nanotube which provide a direct current path. Although the coating was determined to be continuous via TEM and SEM observations, in the first case these were performed on isolated tubes and the second only observed tubes at the edge of the forest. It is possible that tubes in the interior of the forest are not coated well. There are two reasons the forests could be coated less efficiently than isolated tubes. First, the diffusion of precursors into the interior of the forest may be sufficiently long that it does not complete in one cycle of the process. Second, the small aliquot of precursor per cycle may not be sufficient to complete monolayer coverage of the forests. These two effects in principle could be alleviated by increasing the dose and amount of equilibration time of each cycle.

In conclusion, a process for atomic layer deposition on low binding affinity materials has been developed and applied to TiO_2 deposition on nanotubes. The coating process was then applied to production of dye sensitized solar cells using coated carbon nanotube forests as one electrode. Unfortunately, these cells did not out-perform the traditional dye sensitized solar cells due to a significant shunt conductance present. Further work is needed to implement ALD-coated nanotube electrodes in dye-sensitized solar cells, paying particular attention to the ability to coat completely the interior of the forests using a modified process.

Part III

Other Research

Chapter 7

Two-Dimensional Mechanical Membranes

7.1 Device Fabrication

In order to study the mechanical properties of suspended graphene and other materials we microfabricated structures that allowed suspension of isolated sections of graphene (see section A.4). Briefly a silicon wafer with 285 nm of silicon oxide was patterned using standard photolithography and etched with an SF_6 plasma to produce an array of holes 1 micron in diameter and ~50 nm deep. Kish graphite was then exfoliated onto the sample and thin flakes were identified using the standard optical contrast on unsuspended portions and confirmed via Raman spectroscopy. To contact the samples a low temperature soldering method[33] was used to avoid lithography and capillary forces associated with drying, which tend to rip the sheet. Typically, a single solder contact was made to each flake to ground the sample and allow the ability to apply a gate potential to the flake supplied via a silver paint contact to the silicon substrate. The AFM tip was also grounded to eliminate any electrostatic force between the AFM tip and the sheet during scanning.

7.2 Buckling and Strain in Suspended Graphene

The forces involved in exfoliating graphene onto a substrate can lead to induced strain in the sheet. Typically, the van der Waals force bonding the graphene to the substrate flattens the sheet and prevents observation of any geometric effects due to the strain. However, the portions of the graphene sheets suspended over holes in our substrates are free from substrate interactions and thus can exhibit buckling and wrinkling induced by strain. Figure 7.2 shows a tapping mode AFM image of buckling induced in a bilayer graphene sheet suspended over four separate 1 micron diameter holes. Compressive strain due to the exfoliation procedure has induced ripples of similar magnitude and wavelength across all four of the holes.

Wrinkling is a general phenomena in elastic sheets subjected to compressive strain[16, 15]. In general, detailed knowledge of the strain field and geometric boundary conditions are necessary to solve the highly nonlinear problem. However, general arguments based on

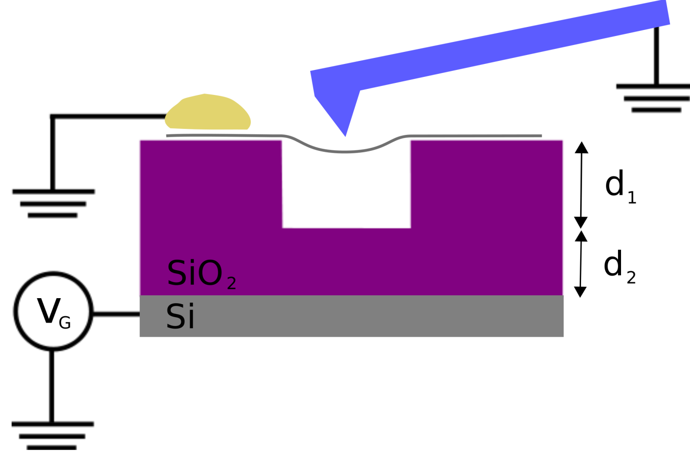

Figure 7.1: Schematic of the measurement geometry for electrostatic AFM measurements. The graphene sheet is mechanically exfoliated over the pre-etched holes in the SiO_2 substrate. It is then contacted using solder. Both the sample and the AFM tip are grounded to prevent electrostatic interaction between the tip and the sheet. A voltage is applied to the heavily doped silicon substrate to act as a back gate. d_1 and d_2 are the height of the sheet above the bottom of the hole and the thickness of the remaining SiO_2 used for capacitance calculations.

balancing the bending and stretching energies in the sheet give a simple scaling law between the wavelength and the amplitude of the wrinkles[16].

$$\gamma \approx \frac{1}{\nu}\left(\frac{A}{\lambda}\right)^2 \tag{7.1}$$

Where $\gamma = \frac{\delta \ell}{\ell_0}$ is the strain in the sheet, $\nu = 0.16$ is the Poisson ratio of the material, A is the amplitude of the wrinkles and λ is the wavelength of the ripples. The exact solution involves multiplicative corrections $\mathcal{O}(1)$ due to the exact boundary conditions of the geometry. We can use the measured amplitude and wavelength from figure 7.2 to deduce a value of the compressive strain in the graphene sheet in table 7.2.

An additional way to determine the strain inducing the ripples is by measuring the shift in the Raman G mode which under a compressive strain shifts as[63]

$$\Delta\omega_G = \frac{E}{2\omega_0}\left(A(S_{11} + S_{12})\right)\gamma = -3438\gamma \text{ (cm}^{-1}) \tag{7.2}$$

Where $E = 0.92$ TPa is the Young's modulus, $A = -1.44 \times 10^7$ cm^{-2}, $S_{11} = 0.98$ TPa^{-1}, $S_{12} = -0.16$ TPa^{-1} are constants derived from measurements on graphite and $\omega_0 = 1580.021$ cm^{-1} is the unstrained G-mode frequency[63]. Using this formula and the measured G-band frequencies over the various holes we can correlate the strain deduced by the Raman shift with the strain inferred from the scaling analysis.

The results of both methods of determining the strain are presented in table 7.2 The agreement between these two measurements is rather poor. This is likely due to the fact that

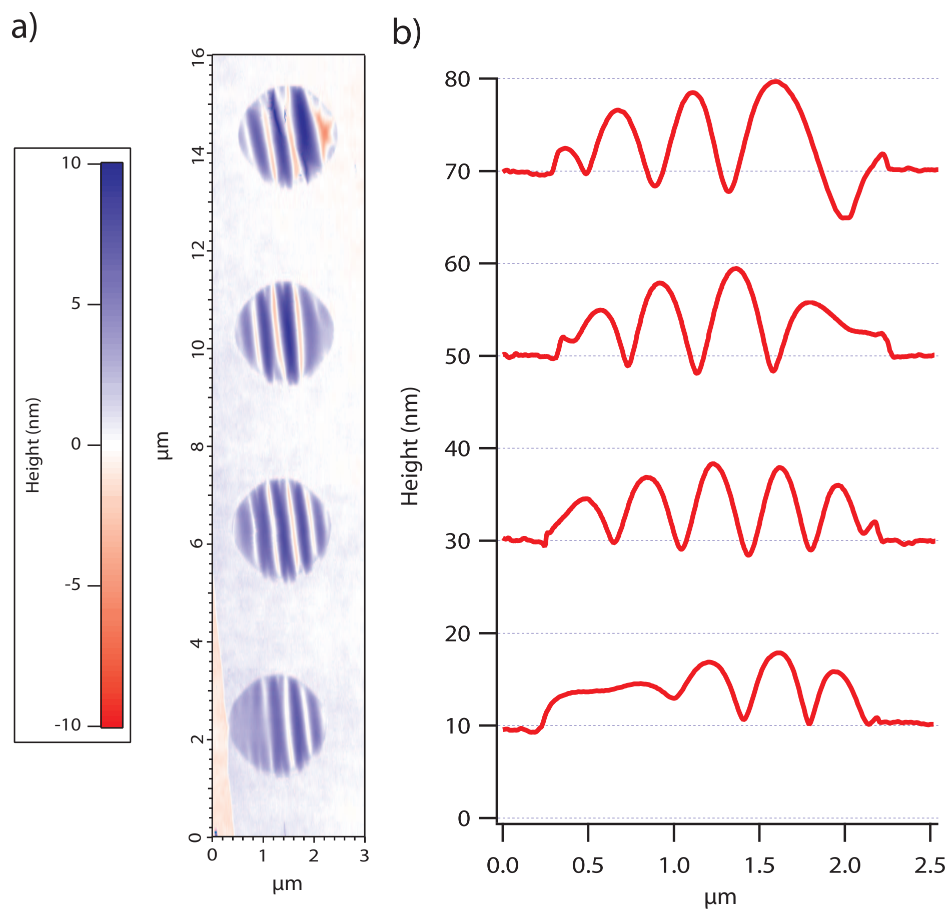

Figure 7.2: Wrinkling in graphene sheets exfoliated over holes. Tapping mode AFM images of suspended graphene wrinkling over four holes in a) and line profiles across the center of the holes in b)

Hole Number	A(nm)	λ (nm)	$\gamma_{scaling}$ (10^{-4})	$\Delta\omega_G$ (cm^{-1})	γ_{Raman} (10^{-4})
1	4.0	520	3.7	-1.3	3.8
2	3.4	450	3.6	-2.7	7.9
3	3.6	390	5.3	-2.9	8.3
4	2.9	370	3.8	-2.5	7.3

Table 7.1: Summary of wrinkling data measured by AFM and Raman spectroscopy. Amplitude A and wavelength λ of the wrinkles measured by AFM and the compressive strain $\gamma_{scaling}$ inferred from equation 7.1. Measured Raman shift $\Delta\omega_G$ with respect to $\omega_G^0 = 1580.021$ cm^{-1} calibrated on a thick portion of the same graphene flake and inferred strain γ_{Raman} from equation 7.2

the G-position is affected not only by the local strain field, but also by induced doping[60]. The magnitude of doping induced shifts due to impurities during processing is similar in magnitude to the expected strain induced shifts. Recent work on temperature induced strain and rippling has controllably produced larger ripples and higher strains[4, 18].

7.3 Electrostatic Deflection of Suspended Graphene

If the exfoliation process has not induced an asymmetric strain field, the graphene sheet will lie flat across the holes as shown in figure 7.3. Note that the sheet is typically pulled down and taut like a drum head by van der Waals attraction to the sides of the hole. On these flat sheets we can apply a potential to the back gate and controllably deform the membrane. A fixed back-gate potential is applied and then a tapping-mode AFM image is acquired, which shows increasing bending of the graphene sheet under applied potential (figure 7.3).

The deflection of the graphene sheet is similar for positive and negative potentials applied to the back gate. This can be understood by considering the forces due to the applied potential. The electrostatic charge on the back gate produces a force on the sheet given by differentiating the electrostatic potential energy of a parallel plate capacitor.

$$U = \frac{1}{2} C_g V_g^2 \tag{7.3}$$

$$F = -\frac{\mathrm{d}U}{\mathrm{dz}} = -\frac{1}{2}\frac{\mathrm{d}C_g}{\mathrm{d}z} V_g^2 = \frac{k_2^2 \epsilon_0 A}{2(d_2 + k_2 d_1)^2} V_g^2 \tag{7.4}$$

Where for our sample we have $k_2 = 3.9$ for SiO_2 and $d_1 = 109$ nm and $d_2 = 181$ nm from the measured depth of uncovered holes and the known oxide thickness (see section A.4 for details). This force produces a pressure ($P = F/A$) of

$$P = 183.3\, V_g^2 \quad \text{(Pa)} \tag{7.5}$$

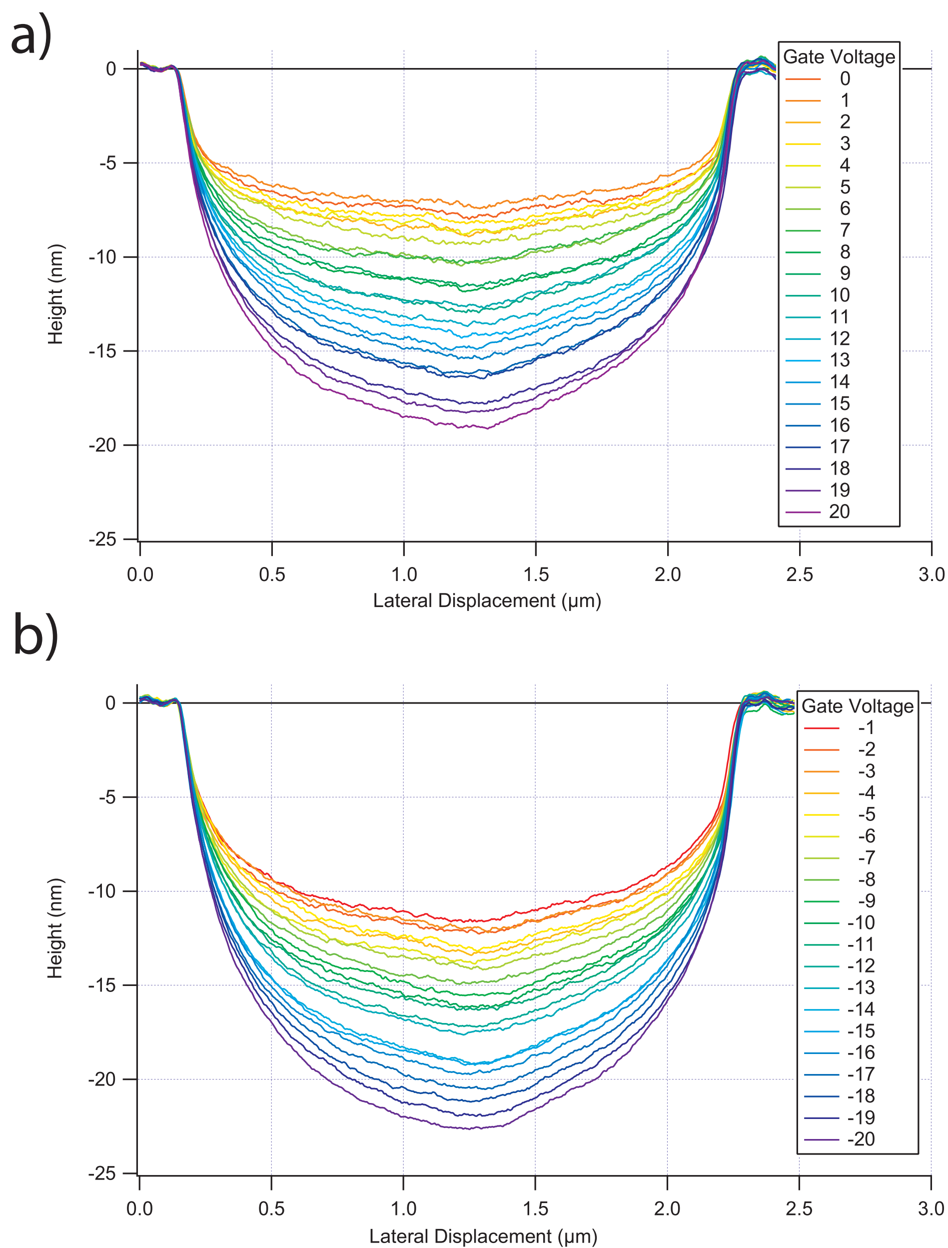

Figure 7.3: Imaging electrostatic deflection of bilayer graphene. Profiles measured by tapping mode AFM across the middle of a suspended bilayer membrane at different applied gate voltage, a) $V_g > 0$ and b) $V_g > 0$

Note that since the plates of the capacitor are always oppositely charged this is always an attractive force resulting in the symmetry with respect to gate voltage. Using classical continuum mechanics the maximum deflection of a tensioned membrane subjected to a transverse pressure satisfies the following equation [37]

$$Eh\xi_{max}^3 + 4R^2\alpha^3 T\xi_{max} - R^4\alpha^3 P = 0 \tag{7.6}$$

where $R = 1.0665$ microns is the measured radius of the circular membrane, $P = 183.3\,V_g^2$ Pa is the pressure induced by the gate voltage, E is the Young's modulus, $h = 0.78$ nm is the thickness of the bilayer membrane measured by AFM, T is the constant preloaded tension per unit length along the boundary induced by the van der Waals attraction as noted above and

$$\alpha = \frac{6615\,(\nu^2 - 1)}{2\,(2791\nu^2 - 4250\nu - 7505)} \tag{7.7}$$

with $\nu = 0.165$ the Poisson's ratio of the graphene membrane. Using the measured $\xi_{max}(V_g)$ extracted from figure 7.3, we fit equation 7.6 to obtain the Young's modulus E and preloaded tension T due to the van der Waals force. In figure 7.4 we see the extracted maximum deflection and the fit to equation 7.6 with an extracted Young's modulus of $E =$ 14.4 TPa and preloaded tension of $T = 1.2$ N/m. The extreme discrepancy between the extracted value and the accepted value of 1.1 TPa is likely due to an incorrect height inferred from AFM measurements over the suspended portion of the sheet. McEuen et al. found that the tip graphene interaction is modified on the portion that is suspended sheets[11] when the AFM is operated using the same amplitude feedback on non-suspended and suspended portions. Since we are making a relative measurement this should not affect our results. It seems most likely that our results are skewed the extremely high value of the initial tension.

Kwanpyo Kim continues the study of electromechanical membranes formed out of graphene sheets and in particular their properties probed via in situ TEM measurements.

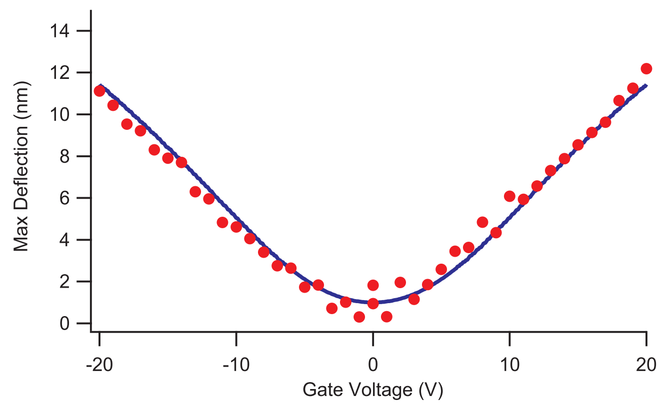

Figure 7.4: Extraction of mechanical parameters from the maximum deflection of the graphene sheet as a function of gate voltage for the data shown in figure 7.3. Note that the data for negative gate voltages has been shifted downwards by a constant amount to account for hysterisis induced by slipping of the sheet between measurements (see text). The blue curve is a fit to equation 7.6.

Bibliography

[1] J Aarik, A Aidla, T Uustare, and V Sammelselg. Morphology and structure of tio2 thin-films grown by atomic layer deposition. *Journal Of Crystal Growth*, 148(3):268–275, MAR 1995.

[2] L.G. Aslamazov and A. I. Larkin. Influence of fluctuation pairing of electrons on conductivity of normal metal. *Phys. Lett. A*, A 26(6):238–&, 1968.

[3] Mn Baibich, Jm Broto, A Fert, Fn Vandau, F Petroff, P Eitenne, G Creuzet, A Friederich, and J Chazelas. Giant magnetoresistance of (001)fe/(001) cr magnetic superlattices. *Physical Review Letters*, 61(21):2472–2475, NOV 21 1988.

[4] Wenzhong Bao, Feng Miao, Zhen Chen, Hang Zhang, Wanyoung Jang, Chris Dames, and Chun Ning Lau. Controlled ripple texturing of suspended graphene and ultrathin graphite membranes. *Nature Nanotechnology*, 4(9):562–566, SEP 2009.

[5] J Bardeen. Surface states and rectification at a metal semi-conductor contact. *Physical Review*, 71(10):717–727, 1947.

[6] M. R. Beasley, J. E. Mooij, and T. P. Orlando. Possibility of vortex-antivortex pair dissociation in 2-dimensional superconductors. *Phys. Rev. Lett.*, 42(17):1165–1168, 1979.

[7] V.L. Berezinskii. Destruction of long-range order in one-dimensional and 2-dimensional systems possessing a continuous symmetry group .2. quantum systems. *Sov. Phys. JETP*, 34(3):610, 1972.

[8] SK Bhatia and AL Myers. Optimum conditions for adsorptive storage. *Langmuir*, 22(4):1688–1700, FEB 14 2006.

[9] P. Blake, E. W. Hill, A. H. Castro Neto, K. S. Novoselov, D. Jiang, R. Yang, T. J. Booth, and A. K. Geim. Making graphene visible. *Applied Physics Letters*, 91(6), AUG 6 2007.

[10] S Brunauer, PH Emmett, and E Teller. Adsorption of gases in multimolecular layers. *Journal Of The American Chemical Society*, 60:309–319, JAN-JUN 1938.

[11] J. Scott Bunch, Scott S. Verbridge, Jonathan S. Alden, Arend M. van der Zande, Jeevak M. Parpia, Harold G. Craighead, and Paul L. McEuen. Impermeable atomic membranes from graphene sheets. *Nano Letters*, 8(8):2458–2462, AUG 2008.

[12] LG Cancado, K Takai, T Enoki, M Endo, YA Kim, H Mizusaki, A Jorio, LN Coelho, R Magalhaes-Paniago, and MA Pimenta. General equation for the determination of the crystallite size L-a of nanographite by Raman spectroscopy. *Applied Physics Letters*, 88(16), APR 17 2006.

[13] A. H. Castro Neto, F. Guinea, N. M. R. Peres, K. S. Novoselov, and A. K. Geim. The electronic properties of graphene. *Reviews Of Modern Physics*, 81(1):109–162, JAN-MAR 2009.

[14] A. D. Caviglia, S. Gariglio, N. Reyren, D. Jaccard, T. Schneider, M. Gabay, S. Thiel, G. Hammerl, J. Mannhart, and J. M. Triscone. Electric field control of the laalo3/srtio3 interface ground state. *Nature*, 456(7222):624–627, 2008.

[15] E Cerda and L Mahadevan. Geometry and physics of wrinkling. *Physical Review Letters*, 90(7), FEB 21 2003.

[16] E Cerda, K Ravi-Chandar, and L Mahadevan. Thin films - Wrinkling of an elastic sheet under tension. *Nature*, 419(6907):579–580, OCT 10 2002.

[17] Joseph G. Checkelsky, Lu Li, and N. P. Ong. Divergent resistance at the Dirac point in graphene: Evidence for a transition in a high magnetic field. *Physical Review B*, 79(11), MAR 2009.

[18] Chun-Chung Chen, Wenzhong Bao, Jesse Theiss, Chris Dames, Chun Ning Lau, and Stephen B. Cronin. Raman Spectroscopy of Ripple Formation in Suspended Graphene. *Nano Letters*, 9(12):4172–4176, DEC 2009.

[19] J. H. Chen, C. Jang, S. Adam, M. S. Fuhrer, E. D. Williams, and M. Ishigami. Charged-impurity scattering in graphene. *Nat. Phys.*, 4(5):377–381, 2008.

[20] LL Chua, J Zaumseil, JF Chang, ECW Ou, PKH Ho, H Sirringhaus, and RH Friend. General observation of n-type field-effect behaviour in organic semiconductors. *Nature*, 434(7030):194–199, MAR 10 2005.

[21] R. W. Crane, N. P. Armitage, A. Johansson, G. Sambandamurthy, D. Shahar, and G. Gruner. Fluctuations, dissipation, and nonuniversal superfluid jumps in two-dimensional superconductors. *Physical Review B*, 75(9), MAR 2007.

[22] Mircea Dinca, Anne Dailly, Yun Liu, Craig M. Brown, Dan. A. Neumann, and Jeffrey R. Long. Hydrogen storage in a microporous metal-organic framework with exposed Mn2+ coordination sites. *Journal Of The American Chemical Society*, 128(51):16876–16883, DEC 27 2006.

[23] X. Du, I. Skachko, and E. Y. Andrei. Josephson current and multiple andreev reflections in graphene sns junctions. *Physical Review B*, 77(18):184507, 2008.

[24] X. Du, I. Skachko, A. Barker, and E. Y. Andrei. Approaching ballistic transport in suspended graphene. *Nat. Nanotechnol.*, 3(8):491–495, 2008.

[25] K. Epstein, A. M. Goldman, and A. M. Kadin. Renormalization effects near the vortex-unbinding transition of two-dimensional superconductors. *Physical Review B*, 26(7):3950–3953, 1982.

[26] D. B. Farmer, R. Golizadeh-Mojarad, V. Perebeinos, Y. M. Lin, G. S. Tulevski, J. C. Tsang, and P. Avouris. Chemical doping and electron-hole conduction asymmetry in graphene devices. *Nano Lett.*, 9(1):388–392, 2009.

[27] DB Farmer and RG Gordon. ALD of high-kappa dielectrics on suspended functionalized SWNTs. *Electrochemical And Solid State Letters*, 8(4):G89–G91, 2005.

[28] M. V. Feigel'man, M. A. Skvortsov, and K. S. Tikhonov. Proximity-induced superconductivity in graphene. *JETP Lett.*, 88(11):862–866, 2008.

[29] A. C. Ferrari, J. C. Meyer, V. Scardaci, C. Casiraghi, M. Lazzeri, F. Mauri, S. Piscanec, D. Jiang, K. S. Novoselov, S. Roth, and A. K. Geim. Raman spectrum of graphene and graphene layers. *Phys. Rev. Lett.*, 97(18):187401, 2006.

[30] A. K. Geim and K. S. Novoselov. The rise of graphene. *Nat. Mater.*, 6(3):183–191, 2007.

[31] G. Giovannetti, P. A. Khomyakov, G. Brocks, V. M. Karpan, J. van den Brink, and P. J. Kelly. Doping graphene with metal contacts. *Phys. Rev. Lett.*, 101(2):026803, 2008.

[32] Gianluca Giovannetti, Petr A. Khomyakov, Geert Brocks, Paul J. Kelly, and Jeroen van den Brink. Substrate-induced band gap in graphene on hexagonal boron nitride: Ab initio density functional calculations. *Physical Review B*, 76(7), AUG 2007.

[33] Caglar O. Girit and A. Zettl. Soldering to a single atomic layer. *Applied Physics Letters*, 91(19), NOV 5 2007.

[34] WQ Han, W Mickelson, J Cumings, and A Zettl. Transformation of bxcynz nanotubes to pure bn nanotubes. *Applied Physics Letters*, 81(6):1110–1112, AUG 5 2002.

[35] Db Haviland, Y Liu, and Am Goldman. Onset of superconductivity in the two-dimensional limit. *Physical Review Letters*, 62(18):2180–2183, MAY 1 1989.

[36] H. B. Heersche, P. Jarillo-Herrero, J. B. Oostinga, L. M. K. Vandersypen, and A. F. Morpurgo. Bipolar supercurrent in graphene. *Nature*, 446(7131):56–59, 2007.

[37] Alfonso Hermida. Deflection of stretched circular membrane under pressure. *NASA Tech Briefs*, page GSC14223, September 1999.

[38] J. C. Heyraud and J. J. Métois. Equilibrium shape and temperature; lead on graphite. *Surface Science*, 128(2-3):334–342, 1983.

[39] RL Hirsch, R Bezdek, and R Wendling. Peaking of world oil production and its mitigation. *Aiche Journal*, 52(1):2–8, JAN 2006.

[40] B. Huard, N. Stander, J. A. Sulpizio, and D. Goldhaber-Gordon. Evidence of the role of contacts on the observed electron-hole asymmetry in graphene. *Phys. Rev. B*, 78(12):121402(R), 2008.

[41] SH Jhi and YK Kwon. Hydrogen adsorption on boron nitride nanotubes: A path to room-temperature hydrogen storage. *Physical Review B*, 69(24), JUN 2004.

[42] B. M. Kessler, C. Oe. Girit, A. Zettl, and V. Bouchiat. Tunable Superconducting Phase Transition in Metal-Decorated Graphene Sheets. *Physical Review Letters*, 104(4), JAN 29 2010.

[43] Markus Koenig, Steffen Wiedmann, Christoph Bruene, Andreas Roth, Hartmut Buhmann, Laurens W. Molenkamp, Xiao-Liang Qi, and Shou-Cheng Zhang. Quantum spin hall insulator state in HgTe quantum wells. *Science*, 318(5851):766–770, NOV 2 2007.

[44] N Kopidakis, KD Benkstein, J van de Lagemaat, and AJ Frank. Transport-limited recombination of photocarriers in dye-sensitized nanocrystalline TiO2 solar cells. *Journal Of Physical Chemistry B*, 107(41):11307–11315, OCT 16 2003.

[45] J. M. Kosterlitz and D. J. Thouless. Ordering, metastability and phase-transitions in 2 dimensional systems. *J. Phys. C: Solid State Phys.*, 6(7):1181–1203, 1973.

[46] Yoichi Kubota, Kenji Watanabe, Osamu Tsuda, and Takashi Taniguchi. Deep ultraviolet light-emitting hexagonal boron nitride synthesized at atmospheric pressure. *Science*, 317(5840):932–934, AUG 17 2007.

[47] Matt Law, Lori E. Greene, Aleksandra Radenovic, Tevye Kuykendall, Jan Liphardt, and Peidong Yang. ZnO-Al2O3 and ZnO-TiO2 core-shell nanowire dye-sensitized solar cells. *Journal Of Physical Chemistry B*, 110(45):22652–22663, NOV 16 2006.

[48] E. J. H. Lee, K. Balasubramanian, R. T. Weitz, M. Burghard, and K. Kern. Contact and edge effects in graphene devices. *Nat. Nanotechnol.*, 3(8):486–490, 2008.

[49] RZ Ma, Y Bando, HW Zhu, T Sato, CL Xu, and DH Wu. Hydrogen uptake in boron nitride nanotubes at room temperature. *Journal Of The American Chemical Society*, 124(26):7672–7673, JUL 3 2002.

[50] E. McCann, K. Kechedzhi, Vladimir I. Fal'ko, H. Suzuura, T. Ando, and B. L. Altshuler. Weak-localization magnetoresistance and valley symmetry in graphene. *Physical Review Letters*, 97(14), OCT 6 2006.

[51] JW McPherson, J Kim, A Shanware, H Mogul, and J Rodriguez. Trends in the ultimate breakdown strength of high dielectric-constant materials. *Ieee Transactions On Electron Devices*, 50(8):1771–1778, AUG 2003.

[52] Petter Minnhagen. The two-dimensional coulomb gas, vortex unbinding, and superfluid-superconducting films. *Rev. Mod. Phys.*, 59(4):1001–1066, Oct 1987.

[53] D. S. Novikov. Numbers of donors and acceptors from transport measurements in graphene. *Applied Physics Letters*, 91(10), SEP 3 2007.

[54] B Oregan and M Gratzel. A low-cost, high-efficiency solar-cell based on dye-sensitized colloidal tio2 films. *Nature*, 353(6346):737–740, OCT 24 1991.

[55] D. Pacile, J. C. Meyer, C. Oe. Girit, and A. Zettl. The two-dimensional phase of boron nitride: Few-atomic-layer sheets and suspended membranes. *Applied Physics Letters*, 92(13), MAR 31 2008.

[56] K. A. Parendo, K. H. Sarwa, B. Tan, A. Bhattacharya, M. Eblen-Zayas, N. E. Staley, and A. M. Goldman. Electrostatic tuning of the superconductor-insulator transition in two dimensions. *Phys. Rev. Lett.*, 94(19):197004, 2005.

[57] C. H. Park, L. Yang, Y. W. Son, M. L. Cohen, and S. G. Louie. Anisotropic behaviours of massless dirac fermions in graphene under periodic potentials. *Nat. Phys.*, 4(3):213–217, 2008.

[58] K. Pi, K. M. McCreary, W. Bao, W. Han, Y. F. Chiang, Y. Li, S. W. Tsai, C. N. Lau, and R. K. Kawakami. Electronic doping and scattering by transition metals on graphene. *Phys. Rev. B*, 80(7):5, 2009.

[59] Simone Pisana, Patrick M. Braganca, Ernesto E. Marinero, and Bruce A. Gurney. Tunable Nanoscale Graphene Magnetometers. *Nano Letters*, 10(1):341–346, JAN 2010.

[60] Simone Pisana, Michele Lazzeri, Cinzia Casiraghi, Kostya S. Novoselov, A. K. Geim, Andrea C. Ferrari, and Francesco Mauri. Breakdown of the adiabatic Born-Oppenheimer approximation in graphene. *Nature Materials*, 6(3):198–201, MAR 2007.

[61] D. Poplavskyy. Comment on extraordinary magnetoresistance of a semiconductor-metal composite van der pauw disk. *Journal of Magnetism and Magnetic Materials*, 267(3):406 – 407, 2003.

[62] A. J. Rimberg, T. R. Ho, C. Kurdak, J. Clarke, K. L. Campman, and A. C. Gossard. Dissipation-driven superconductor-insulator transition in a two-dimensional josephson-junction array. *Phys. Rev. Lett.*, 78(13):2632–2635, 1997.

[63] H Sakata, G Dresselhaus, Ms Dresselhaus, and M Endo. Effect of uniaxial-stress on the raman-spectra of graphite fibers. *Journal Of Applied Physics*, 63(8, Part 1):2769–2772, APR 15 1988.

[64] Saeed Saremi. RKKY in half-filled bipartite lattices: Graphene as an example. *Physical Review B*, 76(18), NOV 2007.

[65] S. A. Shevlin and Z. X. Guo. Hydrogen sorption in defective hexagonal BN sheets and BN nanotubes. *Physical Review B*, 76(2), JUL 2007.

[66] SA Solin, T Thio, DR Hines, and JJ Heremans. Enhanced room-temperature geometric magnetoresistance in inhomogeneous narrow-gap semiconductors. *Science*, 289(5484):1530–1532, SEP 1 2000.

[67] B. Spivak, P. Oreto, and S. A. Kivelson. Approach to a superconductor-to-bose-insulator transition in disordered films. *Phys. Rev. B*, 77(21):214523, June 2008.

[68] Myles A. Steiner, Nicholas P. Breznay, and Kapitulnik Aharon. Approach to a superconductor-to-bose-insulator transition in disordered films. *Phys. Rev. B*, 77(21):212501, June 2008.

[69] S. Takei and Y. B. Kim. Nonequilibrium-induced metal-superconductor quantum phase transition in graphene. *Phys. Rev. B*, 78(16):165401, 2008.

[70] S. Teitel and C. Jayaprakash. Josephson-junction arrays in transverse magnetic-fields. *Phys. Rev. Lett.*, 51(21):1999–2002, 1983.

[71] P. Thevenin, A. Soltani, and A. Bath. Synthesis of hexagonal boron nitride thin films by a plasma assisted chemical vapor deposition method. *Journal de Physique IV (Proceedings)*, 11(3):Pr3–803–10, August 2001.

[72] W Thomson. *Proceedings of the Royal Society*, 8:546, 1857.

[73] Nikolaos Tombros, Csaba Jozsa, Mihaita Popinciuc, Harry T. Jonkman, and Bart J. van Wees. Electronic spin transport and spin precession in single graphene layers at room temperature. *Nature*, 448(7153):571–U4, AUG 2 2007.

[74] Dc Tsui, Hl Stormer, and Ac Gossard. Two-dimensional magnetotransport in the extreme quantum limit. *Physical Review Letters*, 48(22):1559–1562, 1982.

[75] K. Ueno, S. Nakamura, H. Shimotani, A. Ohtomo, N. Kimura, T. Nojima, H. Aoki, Y. Iwasa, and M. Kawasaki. Electric-field-induced superconductivity in an insulator. *Nature Materials*, 7(11):855–858, NOV 2008.

[76] K Von Klitzing, G Dorda, and M Pepper. New method for high-accuracy determination of the fine-structure constant based on quantized hall resistance. *Physical Review Letters*, 45(6):494–497, 1980.

[77] Karl-Heinz Wagenblast, Anne van Otterlo, Gerd Schön, and Gergely T. Zimányi. Superconductor-insulator transition in a tunable dissipative environment. *Phys. Rev. Lett.*, 79(14):2730–2733, Oct 1997.

[78] Xinran Wang, Scott M. Tabakman, and Hongjie Dai. Atomic layer deposition of metal oxides on pristine and functionalized graphene. *Journal Of The American Chemical Society*, 130(26):8152+, JUL 2 2008.

[79] C. M. Wolfe, G. E. Stillman, and J. A. Rossi. High apparent mobility in inhomogeneous semiconductors. *Journal of The Electrochemical Society*, 119(2):250–255, 1972.

[80] Xuesong Li, Weiwei Cai, Jinho An, Seyoung Kim, Junghyo Nah, Dongxing Yang, R. Piner, A. Velamakanni, Inhwa Jung, E. Tutuc, S.K. Banerjee, L. Colombo, and R.S. Ruoff. Large-area synthesis of high-quality and uniform graphene films on copper foils. *Science*, 324(5932):1312–14, 5 June 2009.

[81] J. T. Ye, S. Inoue, K. Kobayashi, Y. Kasahara, H. T. Yuan, H. Shimotani, and Y. Iwasa. Liquid-gated interface superconductivity on an atomically flat film. *Nature Materials*, 9(2):125–128, FEB 2010.

[82] Yuanbo Zhang, Victor W. Brar, Caglar Girit, Alex Zettl, and Michael F. Crommie. Origin of spatial charge inhomogeneity in graphene. *Nature Physics*, 5(10):722–726, OCT 2009.

[83] JG Zhu, YF Zheng, and GA Prinz. Ultrahigh density vertical magnetoresistive random access memory (invited). *Journal Of Applied Physics*, 87(9, Part 3):6668–6673, MAY 1 2000.

Appendix A

Device Fabrication

A.1 Exfoliated Graphene Devices

To produce high quality graphene flakes for exfoliated measurements care must be taken with the preparation of both the graphene and underlying substrate. For cryogenic measurements the silicon wafer must be degenerately doped. This means the room temperature resistivity must be below 5 mOhm-cm. This is to ensure that the gate will properly function below ~4 K (liquid He). Note that wafers doped between 5-10 mOhm-cm will function down to 4 K, but below that will become unusable. This is due to the freezing out of carriers evident by gate hysteris and increasingly slow dynamics. These wafers can still be used for experiments at low temperatures provided that the gate voltage is set at a temperature above the temperature the carriers freeze out at. Then the sample can be cooled through the transition, freezing the gate charge configuration in place. This is the method currently being used for cryogenic measurements with double layer ionic based gates[81].

On top of the silicon substrate, a high quality gate oxide must be grown. The best quality gate oxide is dry chlorinated oxide. This leaves the oxide with a minimal amount of charged impurities and the highest breakdown strength. For optical identification of graphene, the ideal thickness is 285 nm as discussed in the text. 285 nm is thick by semiconductor processing standards and many suppliers will suggest wet oxide which is suitable for microelectromechanical (MEMS) structures, but is not suitable as a gate oxide due to excessive defects. Wafers we used from Silicon Quest Intl. with the dry oxide routinely have room temperature breakdown voltages of greater than 100 V corresponding to breakdown fields 3 MV/cm, with improved properties at low temperatures since defects cannot be thermally activated.

Once, the raw wafers have been obtained with the appropriate oxide thickness, they must be prepared for deposition. The standard method to prepare the wafers is a piranha etch. This etch consists of 1:3 hydrogen peroxide in concentrated nitric acid at 60 °C for 15 min. This etch eliminates any organic contamination from the surface and leaves the oxide hydroxyl terminated. A successful piranha etch can be checked by confirming that water wets the surface with near zero contact angle.

A.1.1 Exfoliation of samples onto prepared wafers

For exfoliated devices, samples were prepared from either flakes of Kish graphite or hexagonal boron nitride powder. One or two flakes were dropped onto a piece of transparent Scotch tape approximately six inches long. This piece of tape was then folded over onto itself and peeled back approximately four times until a fairly uniform coating appeared, ie. transition from a Rorschach type pattern to to a "glittery dirt." A suitable prepared silicon substrate approximated half an inch wide and four inches long was secured with double-sided tape (Scotch brand removable) on its backside. The tape with exfoliated graphene was then pressed down using a thumb moving across the substrate.

After the tape was secured to the silicon substrate, further pressing was employed to ensure full contact of the silicon and tape. This was observed to be especially important if the tape contained large flakes that provided a "spacer" between the tape and the silicon. Two methods were employed during the removal of tape to produce different densities of samples. In the first method, the tape was slowly peeled backwards while applying pressure between the tape and the sample. This produced a low density of flakes, but a clean substrate with little tape residue between flakes. The second method, involved placing the substrate with tape onto a hotplate at 60 °C. After temperature equilibrium had been reached, the tape was removed using the same pressing method while hot (using latex gloves for thermal protection). This technique produced a higher density of flakes, but resulted in a higher density of tape residue between flakes.

A.1.2 Optical identification of thin flakes

To characterize the exfoliated microcrystallites before sample fabrication we use a form of simple optical absorption spectroscopy correlated to AFM measurements. The optical absorption setup consisted of a tungsten white light source illuminating the sample through the objective of a microscope. Light collected by the microscope is passed though a selected bandpass filter with a band width of 10 nm before being recorded using a CCD. Using simple electromagnetic theory, the intensity of reflected light can be found by considering the thickness and dielectric constant of each material in the stack; hBN or graphene (n_1, D_1 then 285 nm SiO_2 ($n_2, d_2 = 285$ nm) and a back plane of Si n_3.

$$I = \left| \frac{r_1 e^{i(\Phi_1+\Phi_2)} + r_2 e^{i(\Phi_1-\Phi_2)} + r_3 e^{-i(\Phi_1+\Phi_2)} + r_1 r_2 r_3 e^{i(\Phi_1-\Phi_2)}}{e^{i(\Phi_1+\Phi_2)} + r_1 r_2 e^{i(\Phi_1-\Phi_2)} + r_1 r_3 e^{i(\Phi_1+\Phi_2)} + r_2 r_3 e^{i(\Phi_1-\Phi_2)}} \right|^2 \tag{A.1}$$

with

$$\Phi_i = \frac{2\pi n_i d_i}{\lambda} \quad \text{and} \quad r_i = \frac{n_{i-1} - n_i}{n_{i-1} + n_i} \tag{A.2}$$

with $n_0 = 1$ the vacuum above the flake. So,the contrast is given by by the difference between the intensity with the flake, $I(n_1, d_1)$ and the intensity with just vacuum ($n = 1$), I_0.

$$C(n_1, d_1) = \frac{I_0 - I(n_1, d_1)}{I_0} \tag{A.3}$$

Images stored from the CCD were analyzed for contrast using ImageJ to measure the recorded intensity of a flake and the recorded intensity of the bare substrate in order to calculate the contrast. Note that since we are only concerned with the relative difference in reflection between the bare substrate and boron nitride covered substrate, all systematic errors due to the energy distribution of the white light source and response of the CCD cancel out of our measurement.

The samples were then loaded into an Asylum MFP-3D atomic force microscope to acquire height maps of the flakes. The AFM was used in non-contact (tapping mode) with NSC-35 cantilevers from MikroMasch. The heights were measured as scans across the edge of flakes and the relative difference taken at the step edge to eliminate any artifacts due to sample tilt.

In figure A.1, we show the results of such measurements on several BN flakes. Note that the agreement is fairly good for this method except at 525 nm, which is possibly due to defect absorption in our BN starting material. For graphene, with a much stronger absorption (imaginary part of the dielectric constant), the absorption method is extremely effective and individual layers can be counted by comparing their absorption, ie. the linear portion of equation A.1 gives equally spaced absorption as a function of layer thickness.

A.1.3 Raman scattering analysis of thin flakes

A further method of confirming the thickness and quality of the thin crystallites studied in this work was the application of Raman spectroscopy. Raman spectra were acquired in a Renishaw Invia confocal micro-Raman spectrometer equipped with three lasers and two separate dispersive gratings that separate the light onto a one-dimensional CCD for spectral acquisition. All of the spectra in this thesis were acquired using the 514 nm line as this was the highest quality laser on the system. The Invia system operates in reflection mode and can measure Raman shifts from 100 cm^{-1} (limited by the cutoff of the filter eliminating elastic Rayleigh scattering) to 3200 cm^{-1}.

Raman scattering is the inelastic scattering of photons with the absorption or emission of phonons in the material under study. Measuring the energy lost or gained by the photons as they scatter gives the energy of the phonons emitted or absorbed. The Raman scattering intensity for any mode is directly proportional to the sample thickness since the interaction depends on the optical path length. This gives a rough estimate of the thickness. However, for graphene there is an even more sensitive probe of the thickness for very thin layers. Ferrari et al[29] showed that the 2D mode at 2700 cm^{-1} is hybridized and split into four separate bands when interlayer coupling is taken into account. This means that the 2D mode provides a sensitive measure of the layer number and in particular can allow one to unambiguously identify monolayer graphene samples as shown in figure A.2. However, we note that the hybridization is sensitive to the registry of the graphene layers and incommensurate mis-stacked layers also support a symmetric 2D peak as seen in some CVD bilayers.

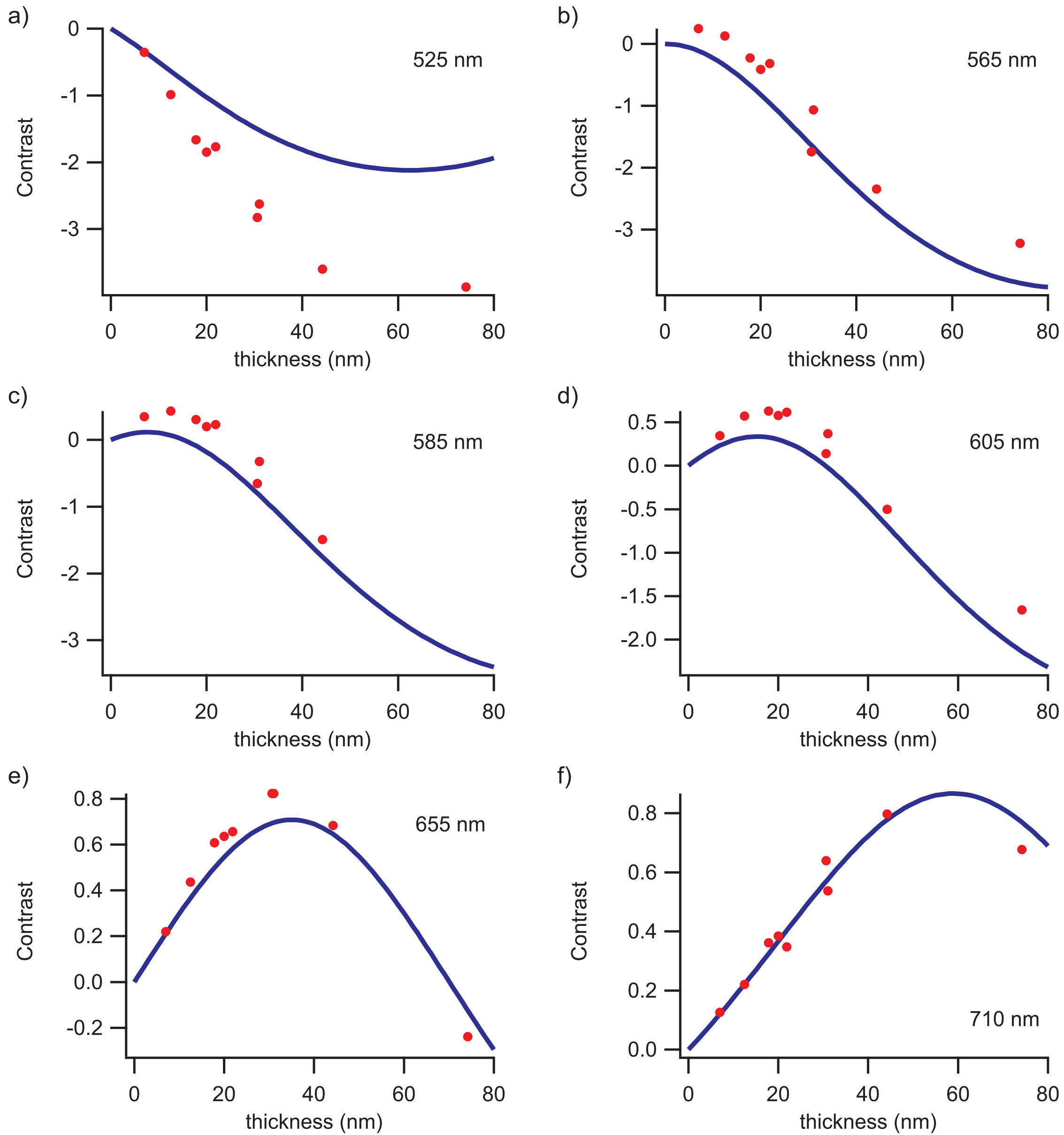

Figure A.1: Contrast vs. height for hBN microcrystals. Measured contrast at 525, 565, 585, 605, 655, and 710 nm (a-f respectively) of various microcrystallites of hexagonal BN on SiO_2/Si as a function of thickness as measured by AFM. The red dots are the data points and the blue line is a global fit over all wavelengths to the dielectric constant $n_{BN} = 1.69$ without any absorption using equation A.3.

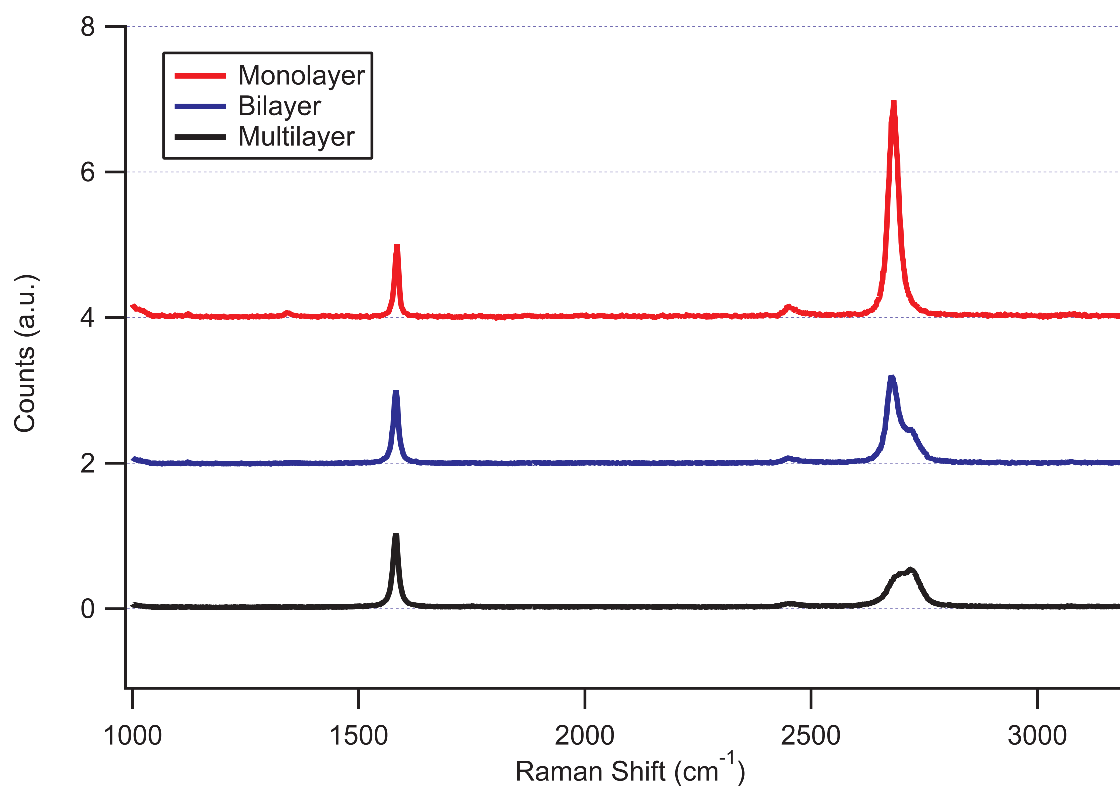

Figure A.2: Raman spectra of different graphene layer thicknesses; monolayer, bilayer and multilayer. Note the evolution of the 2D peak at ~ 2700 cm^{-1} from one symmetric peak to a superposition of four peaks as layer thickness increases. All spectra were acquired for 514 nm excitation and the intensities were normalized to the G peak at ~ 1600 cm^{-1}.

A.1.4 Alignment to scratches for exfoliated graphene

Once appropriate flakes have been identified via optical contrast and Raman scattering[29], electron beam lithography needs to be performed to contact them. Since we are using relatively large portions of wafer and the density of monolayer and bilayer flakes is relatively small it is not worth the work of patterning alignment marks to index the flakes (see section for uses of pre-patterned alignment marks). Instead the most effective method is to make manual scratches into the electron beam resist.

The sample is mounted on the spindle of a spin coater and enough drops of polymethylmethacrylate (PMMA) diluted to 4% concentration in aniline (PMMA A4) to fully cover the sample are deposited. The sample is then spun up to 3000 rpm in 3 seconds where it maintains rotation for 30 seconds before decelerating to rest in 3 seconds. For these conditions, 30 seconds is sufficient to reach the steady state polymer thickness of ∼300 nm. The steady state is confirmed optically due to the constant color observed after ∼25 seconds of rotation.

The coated samples loaded under an optical microscope equipped with a three-axis micromanipulator with a sharp tungsten probe at the end. When the flake of interest is located, the manipulator is used to make four tiny scratches in the resist. The preferred technique is to use only vertical indentations using the z-axis as this produces the smallest scratches. When the scratches have been made, an image of the sample with scratches is taken at 20x to be used in the design of alignment and pattern marks using DesignCAD for interfacing with Nabbity Pattern Generating System (NPGS).

Once loaded into DesignCAD, the outline of the scratches is traced taking care to define the edge of the scratch as the region where the color changes from green to purple as this is the portion that will show contrast in the electron beam when performing alignment. Alignment typically needs to be performed by hand for each device since the location of the flake and orientation will vary from sample to sample. The alignment using this method is typically within one micron limited mainly by the diffraction limit of optical light preventing more precise imaging of the scratch marks. After alignment, the samples are exposed to the electron beam at a does of 350 μC/cm^2 in the desired pattern of the electrodes.

After exposure, the samples are developed in 1:3 solution of methylisobutylketone (MIBK) and isopropyl alcohol (IPA) for 2 minutes to remove the resist from the patterned regions. The samples are now ready for contact deposition. This is done in an 3 kW electron beam (eBeam) evaporator using 60-300 mA of current depending on the material and rates of typically one angstrom per second.

After deposition of contacts, the sample is lifted off in hot acetone (60 °C) stirred for twenty minutes. If the sample has still not lifted off after twenty minutes, it is lightly squirted while still in solution using a syringe. The completely lifted off sample is removed from the hot acetone while spraying with IPA to ensure that it does not dry immediately after removal as this was determined to produce dirtier samples. After rinsing in IPA the sample is blown dry with nitrogen and ready for measurements. See A.3 for an overview of the device during various steps of processing.

For loading into refrigerators, samples were mounted onto copper coated fiberglass circuit boards with predefined traces and standard using silver paint. Care was taken to make sure

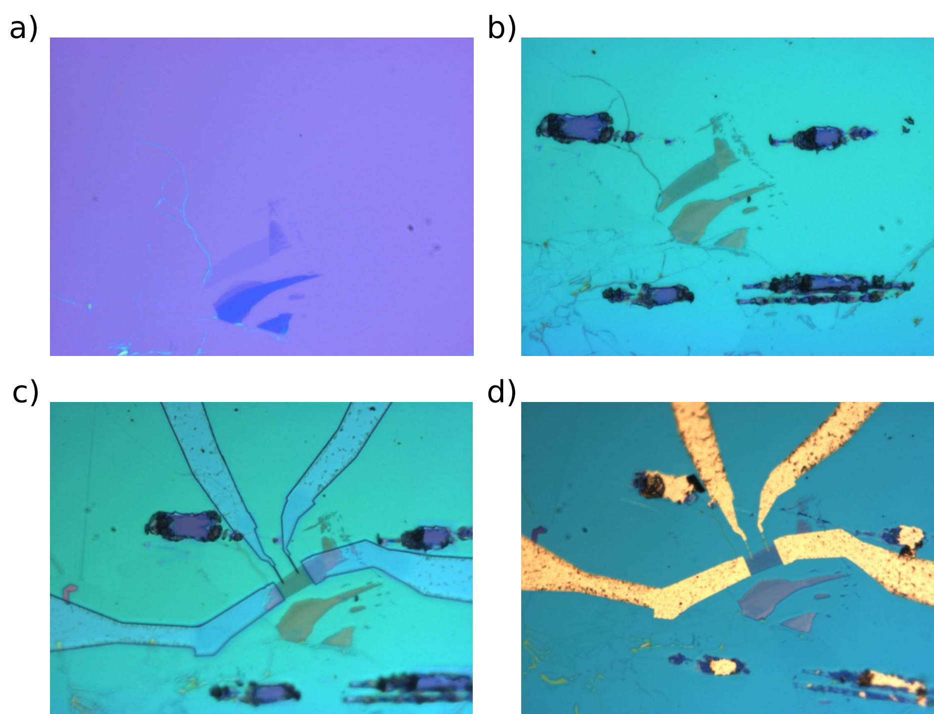

Figure A.3: Alignment and patterning exfoliated graphene sheets. a) Image identifying a prominent bilayer graphene sheet by optical contrast. b) After deposition of Sn and coating with PMMA the resist has been scratched with the micromanipulator for alignment in subsequent electron beam lithography c) After exposing the pattern with the electron beam and developing the resist to check alignment of the patterned features. d) The completed device after deposition of Ti/Au contacts and liftoff.

that the silver paint overlapped an exposed edge of the sample to ensure adequate contact with the silicon for use as a back gate. Once the silver paint was allowed to dry, the sample was electrically contacted using aluminum wire bonded to a trace on the circuit board and the other end on the gold contact pad using a WestBond ultrasonic wirebonder. Limiting the ultrasonic power to 350 μW over 50 ms prevented the bonding process from breaking the gate oxide and destroying the sample.

Overall, non-stop fabrication using this process allows production of about 15 working devices a week.

A.2 Chemical Vapor Deposition Devices

The availability of large sheets of chemical vapor deposited graphene[80] offers many possibilities for new device structures and repeatable parallel fabrication, but some effort must be taken to ensure successful fabrication. The procedure below was found to work extremely well even for devices requiring many patterning steps. Wafers coated with the 285 nm dry oxide are prepared for transfer by first using electron beam lithography to pattern an array of Cr/Au (5/35 nm) alignment marks on the wafer and then etched with piranha to clean the surface before transferring the graphene. It is important to use Cr/Au for the alignment marks since many other possible metals are etched by the piranha solution. Au is ideal for alignment since it is heavy and thus easily visible in the electron microscope. Patterning alignment marks beforehand was found to be essential since the transferred graphene is featureless and basically invisible in the scanning electron microscope when coated by resist.

Graphene is grown by the decomposition of methane onto a copper foil (25 μm thick) at 1000 °C in a Lindberg Blue one-inch tube furnace under vacuum ($\sim$ 500 mTorr) for 15 minutes. The as-grown graphene can be transferred to the prepared wafer from the Cu foil by depositing a layer of PMMA and etching the underlying Cu in a solution of $FeCl_3$. The free floating PMMA/graphene is then fished onto the prepared silicon wafer and allowed to slowly dry overnight at 60 °C. Finally, the PMMA is dissolved in hot acetone at 60 °C to leave a large area sample of CVD graphene on the substrate (see [80] for further details).

The next step in device fabrication is to etch the large area graphene into appropriate sized samples. This step serves two purposes. First, it electrically isolates sections of the graphene to be used as separate devices. Second, it clears portions of the substrate to be used for deposition of contact materials. It was found that if contacts were placed only over the graphene that the adhesion to the substrate was extremely low due to the small van der Waals force between the oxide and graphene, thus contacts would peel off when probed or a wire bond was attempted. The standard electron beam lithography from above is used to pattern the graphene registered to the previously defined alignment marks. This process can be automated in the NPGS system since the arrangement and shape of the alignment marks is predetermined. After the graphene has been exposed into the appropriate shape, eg. a hall bar, via electron beam lithography, the graphene is etched by a short low power oxygen plasma (50 sccm O_2 50 W 20 s). Excess resist can then be washed away using hot acetone (60 °C) and the wafer is coated again using the same PMMA A4 recipe for patterning of the contacts.

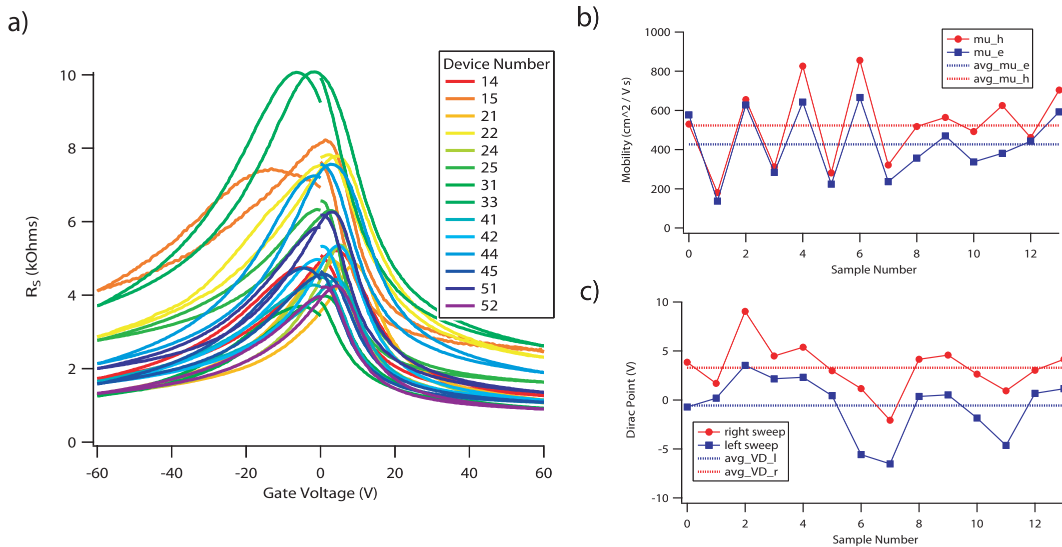

Figure A.4: Electrical characterization of CVD graphene devices a) Sheet resistance versus gate voltage for devices fabricated into 10 micron squares from the same large area graphene sheet. b) Electron and hole mobilities for these devices c) location of the Dirac point, including hysteresis at room temperature.

Now the graphene can be patterned and developed to produce the contacts again using automated alignment and array stepping with NPGS. After depositing the metallic contacts, liftoff in hot acetone, rinsing in isopropyl alcohol and blowing dry with nitrogen as before, the sample is ready for measurements. If more patterning steps are needed, they proceed as above. Note that if you wish to continue patterning after a metal deposition it may be necessary to define another set of alignment marks, since the alignment and deposition can possibly obscure the original set of alignment marks. Overall, this process allows the production of > 100 working devices per week, a considerable improvement versus the exfoliated process allowing a wider range of samples to be tested.

Electrical characterization was performed on 5x5 batches of devices fabricated from the same piece of CVD graphene to determine the quality and reproducibility of devices. As shown in figure A.4 the characteristic of graphene devices are fairly consistent in a batch. However the quality of CVD graphene is not yet as high as exfoliated graphene as seen from the mobility ~ 500 cm^2 / (V s). Work is currently underway to determine the cause of this low mobility.

A.3 Production of the finest features requires attention to the proximity effect

When features are very closely spaced as the Ni bars in section 3.1.1, care must be taken to consider proximity doses. While the electron beam itself is very small, the dose

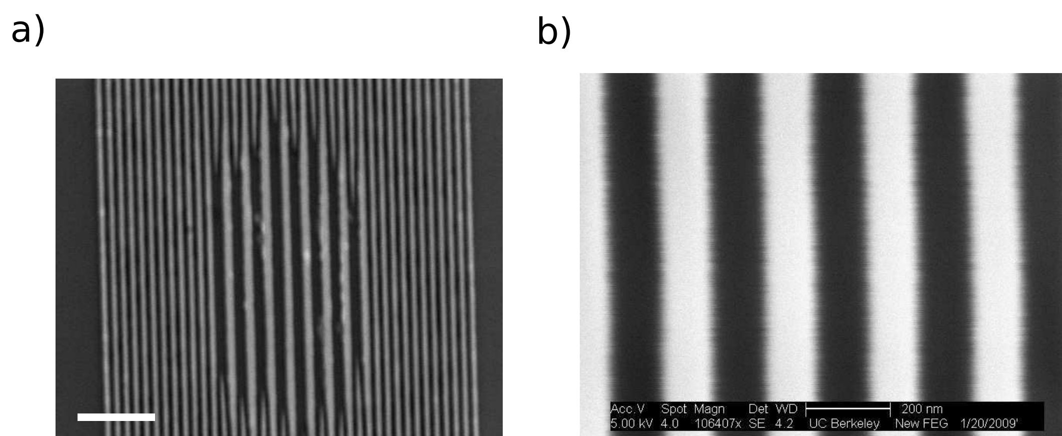

Figure A.5: Image of closely spaced fine features using e-beam lithography. The material deposited was 30/5 nm of Ni/Al and the dosing in a) was uniform exposure at the nominally correct dose 350 μC/ cm^2 and b) is a close up after the dose in the middle has been lowered to account for the proximity effect (see text for details).

due to secondary electrons can have a wide area. For isolated features, this is typically not a problem since the secondary electron dose falls below the threshold for development and results in no measurable difference. However, when features are closely spaced this proximity dose is added to any direct does, causing the actual dose to be increased over the prescribed dose. This results in closely spaced features being overexposed at a dose that is nominally correct for isolated features. This effect is clearly seen in figure A.5. Note that the center of the finely spaced array of lines is overexposed, while the edges remain well defined. This is because the center experiences the highest proximity dose, while the edges see no proximity dose from the outside.

In principle it is possible to account for the extra proximity dose at each point and adjust for it accordingly. For our purposes it is typically acceptable to correct for this effect by making a test exposure at the nominally correct area dose 350 μC / cm^2 (figure A.5) a), noting the boundary of the overexposed region and lowering the exposure in this region. For fine lines, it is typically best to convert from the area dose to an equivalent line dose, which is dependent on the actual size of the electron beam spot used. For the FEI Sirion XL30, spot 1 corresponds to 20 pA of current and the effective line dose was found to be 4 nC/cm. Note that this corresponds to an effective beam width of 114 nm (due to back scattered electrons in the SiO_2. Using this exposure on spot 1 the corrected exposure for the array of fine lines necessary to produce the required superlattices was found to be 4 nC/cm on the first 1.5 microns of short lines from the edge and alternate exposures of 3.75 nC / cm and 3.25 nC/cm for the long and rest of the central short lines respectively. Note that the alternate exposure of long and short lines is to ensure that the ends of the long lines are properly exposed. This does result in small alternation of the thickness between lines, but was deemed the most simplest and most effective solution. The result of making the correction discussed above is shown in figure A.5 b), where lines 125 nm wide and spaced by

125 nm were easily produced by lifting off a Ni/Al (30/5 nm) stack.

A.4 Production of holey substrates for graphene electromechanical measurements

To produce the holey substrates for electromechanical measurements it was necessary to pattern a large area of the wafer with a high density of small features. Since electron beam lithography is a serial procedure, the required time to pattern an area scales with the size of the area. To overcome this limitation we patterned wafers using optical lithography which is inherently parallel process. We had an optical mask fabricated that could be used in either a simple contact exposure or a 5x reduction stepper. Using this mask we could pattern either four or six inch wafers with a large array of holes. After the wafer was exposed and developed, it was etched using an RF plasma (200 W 90 sccm SF_6 5 minutes) in a Ptherm parallel plate etcher to remove a portion of the oxide. Removal of only part of the oxide was to prevent the possibility of shorting the sample to the back gate. This could happen either by the graphene falling to the bottom of holes or through the solder contact wicking to the bottom of the holes. To calibrate the depth of the etch, the AFM was used to measure the depth of the holes and the result compared against the known thickness of the original oxide, giving an etch depth of 109 nm.

Appendix B

Experimental Protocols

B.1 Electrical Measurements

All electronic measurements in this thesis were performed in a four-probe current-biased geometry, except for the breakdown voltage measurements for hBN, which is inherently a two-probe voltage-biased measurement (performed using a Keithley 2410). The four-probe technique is essential for accurate measurements on intrinsic properties of nanoscale samples where contact resistances can vary widely and dominate measured transport properties. In principle, a current bias is applied to the sample through one set of bias-leads and the voltage difference is measured between two probe-leads.

The linear resistance of a device is the voltage drop induced across the voltage leads in the limit of vanishingly small current. The sample may have intrinsic nonlinear properties or there may be non-linearities induced by Joule heating from the applied current. It is particularly important to eliminate these effects for cryogenic measurements where small superconducting critical currents in nanoscale samples present an intrinsic nonlinearity and sample properties may depend sensitively on temperature with Joule heating being a large effect in small samples. The required small bias currents and the associated small voltage drops present a challenge for achieving high signal to noise ratios during measurements.

To eliminate electromagnetic interference it is important that all low level signals (bias currents and induced voltages) be well shielded. The stainless steel room temperature probe station (Desert Cryogenics) with conductive glass viewport as well as the vacuum cans of all the Zettl group cryogenic probes act as effective Faraday cages blocking electromagnetic waves. Therefore it suffices to place high level signals as close to the inputs and outputs of these stages as possible. For current biasing, the simplest way to accomplish this is to place a high resistance bias resistor (1-10 MOhm) on the input to the cryostat and supply a relatively large voltage (0.1-1 V) bias to it. This acts as an effective

The resistor is a standard 1% resistor mounted in a bud box and the voltage is supplied by the output of a Stanford Research Systems 830, 850 or equivalent lock-in amplifier. The use of a lock-in serves two purposes. First, it serves as an intrinsic averaging procedure to increase the signal to noise ratio. Also, by periodically reversing the bias it rejects any spurious offset voltages that may be present such as thermoelectric voltages in cryogenic measurements due

to contacts between dissimilar metals at wire bonds and solder joints. The low-level voltage signals from the sample were amplified by an appropriate pre-amp placed as close as possible to the output feedthrough. In this work, Stanford Research Systems pre-amplifiers were used as well as custom-built low noise pre-amplifiers constructed at the Institut Neel.

Non-linear differential resistance measurements were made by using the same lock-in technique as above, however a larger DC bias voltage was added to produce a DC bias current upon which the differential measurement could be made. To accomplish this the ground of the lock-in oscillator output was "floated" by using a Keithley 2410 or 2612 as a voltage source.

To quickly obtain low resolution current-voltage characteristics of devices to check for nonlinearities, the standard oscilloscope tracing method was used. The same pseudo-current biasing scheme was used except the voltage across the biasing resistor was supplied by a triangle waveform. This bias signal was used as the 'x' input of a Tektronix digital sampling oscilliscope and the voltage signal from the preamp was supplied as the 'y' input. The xy-display then traces out a voltage versus current curve.

For field effect measurements, the gate voltage was supplied by a Keithley 2410 or 2612 and the current was limited by setting the compliance to ensure that it remained below 100 nA. Note that capacitive charging currents transiently reach nanoamp levels, but the steady state leakage current remains at picoamp levels on high quality oxides and thus does not interfere with the measurements of resistance.

All electronic measurements were synchronized over a general purpose interface bus (GPIB) using programs custom written in LabView. Raw data was stored in double precision as text files specifically formatted for the IGOR Pro data analysis software.

B.2 He-3 Refrigeration

The majority of the cryogenic data between 10 K and ~360 mK in this thesis were taken using a Cryo Industries ^{3}He refrigerator in the Zettl research group. For acquiring low temperature data at fixed temperatures below ~360 mK, dilution refrigerators in Grenoble were used. Achieving base temperatures in a dilution refrigerator is straightforward, but they are ineffective for making rapid temperature sweeps between 4 K temperature and base temperature ~100 mK due to slow cycling speeds.

For operation of the ^{3}He fridge to obtain the needed resistance versus temperature data, specific protocols were employed to ensure efficient and accurate operation. In our ^{3}He refrigerator, temperature control is provided by two heaters (one on the sample stage **H1** and one on the charcoal sorb **H2**) and two needle valves (one controlling input to the 1K-pot **N1** and the other to the charcoal sorb **N1**). The 1K-pot and charcoal sorb are pumped by rough pumps through these needle valves to allow cooling via pumping on liquid helium. Additionally, the main sample space is evacuated by a turbo pump to achieve thermal isolation and eliminate cryopumping of impurities onto the sample. After loading into the cryostat and ensuring that no leaks are present, this pump is typically turned off to lower electronic noise levels.

There are several different modes of operation depending on what temperature range you

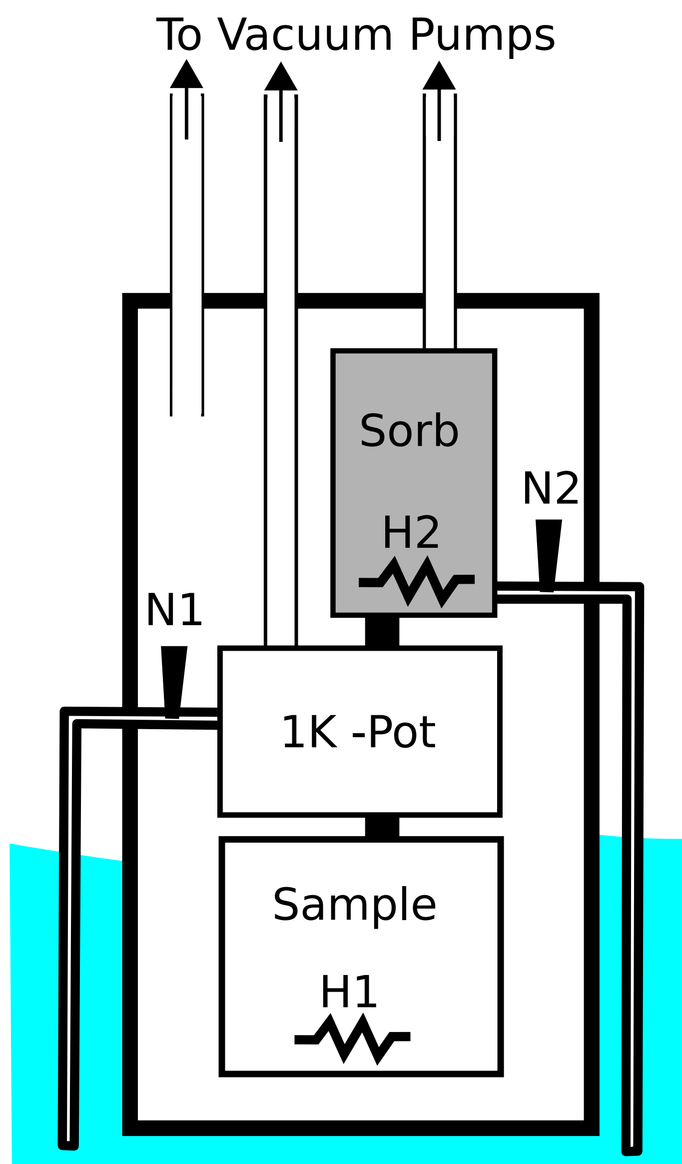

Figure B.1: Schematic of Cryo Industries ^{3}He fridge. The location of the three main stages, charcoal sorb, 1K-pot and sample stage are indicated. The location of the needle valves **N1** and **N2** controlling the 1K-pot and the charcoal sorb are indicated. They pull liquid helium from the bath (blue) through the sipping tubes using the vacuum lines exiting the top of the schematic. The heaters **H1** and **H2** on the sample stage and charcoal sorb are indicated.

are operating in. For sample temperatures between 4 and 1 K, the cooling power is provided by pumping on liquid helium in the 1K-pot. The needle valve to the 1K-pot (**N1**) needs to be set by hand to allow liquid helium to enter and the rough pump must be pumping to achieve cooling power. To achieve thermal contact between the sample and the 1K-pot, ^{3}He gas needs to be present. This is accomplished by ensuring that ^{3}He is desorbed from the the charcoal sorb by heating it to 40 K using the heater (**H2**) and controller (Lakeshore 340). The presence of ^{3}He gas is confirmed by monitoring the pressure in the ^{3}He space and ensuring that it remains positive. Finally, the sample stage heater (**H1**) and a proportional-integral-derivative (PID) control loop from a Lakeshore 340 is used to offset the cooling power of the 1K-pot and maintain a stable temperature in this regime. These temperatures can be maintained indefinitely (as long as liquid helium remains in the cryostat).

Below 1.6 K, the cooling power is provided by pumping on liquid ^{3}He sitting above the sample using the charcoal sorb. The first step to achieve these temperatures is condensing the ^{3}He onto the sample using the 1K-pot. Power to the sample heater should be removed and the cooling power of the 1K-pot maximized using the needle valve (**N1**) while maintaining the charcoal sorb temperature at 40 K using **H2**. The temperature of the 1K-pot and sample stage should drop to $\sim$1.6 K and the pressure in the ^{3}He will drop below atmosphere and stabilize at the low end of the gauge (-30 in Hg). This indicates that all of the ^{3}He has been desorbed from the 1K-pot and condensed onto the sample. to cool the sample further, power was removed from the charcoal sorb heater (**H2**) and the charcoal heater is cooled by opening the needle valve **N2**. This cools the sorb and pumps on the ^{3}He, lowering the temperature of the sample to $\sim$360 mK if no heat is applied to **H1**. Base temperature can be maintained for at least 12 hours under normal operating conditions. If using **H1** to maintain a temperature above base temperature, the temperature can be maintained only for short periods ¡1 hr due to additional heat load causing evaporation of the condensed ^{3}He.

To achieve stable and accurate resistance versus temperature curves over the range 500-6 K, a hybrid procedure needed to be developed to interpolate between these two temperature control regimes. Due to instabilities associated with evaporation of the ^{3}He between 1-2 K upon heating, stable operation is only obtained when cooling the sample. The protocol developed used both needle valves (**N1** and **N2**) cooling the 1K-pot and the charcoal sorb at a high rate. Heaters **H1** and **H2** are controlled via PID loops on Lakeshore 340s to maintain initial temperatures of 6 K at the sample and 40 K at the charcoal sorb. The temperature cycle is started by ramping the setpoint of the PID loop for heater **H1** from 6 K to 300 mK at 0.3 K/min, while maintaining the charcoal sorb at 40 K. When the sample temperature reaches 3 K, the setpoint of **H2** is ramped from 40 K down to 4 K at 6 K/min. When, the sample and charcoal sorb have both reached the lowest temperature, the setpoints can be reset to 6 K and 40 K to quickly heat the system and start the cooling cycle again. Using this protocol, the cooling smoothly crosses between the gas and liquid cooling regimes. Note that this protocol uses a fair amount of liquid helium due to the simultaneous heating and cooling needed for temperature control.

Appendix C

Basic graphene electronic properties

This appendix covers some basic properties of graphene used throughout the main text. In particular, the useful relations between an applied gate voltage and the Fermi energy, Fermi wave vector and carrier concentration as well as the relations between measured resistance and mobility and mean free path. In some cases these differ from the standard relations in two dimensions due to the unique dispersion in graphene.

The structure of graphene consists of carbon bonded into a two dimensional hexagonal lattice. The unit cell contains two inequivalent atoms located at (0,0) and (1.4 Å,0) which form the so-called A and B sublattices, as shown in figure C.1.

Using the crystal structure of graphene, one can make a simple tight binding calculation[13] which gives a band structure as shown in figure C.2. Many of the interesting properties of graphene are due to this unique electronic band structure. As see in the figure, the conduction and valence bands cross the Fermi energy at two inequivalent points labeled K and K'. In the low energy approximation, near the Fermi surface the dispersion takes on a linear character resulting in the so-called Dirac cone in analogy with a relativistic massless Dirac fermion from quantum field theory.

$$E_F = \hbar v_F k_F \tag{C.1}$$

Thus, the quasiparticles in graphene behave as effective one dimensional massless particles with a "speed of light" given by the Fermi velocity

$$v_F = 10^6 \mathrm{m/s} \tag{C.2}$$

The conductance σ of graphene is given by the standard relation between carrier density and carrier mobility

$$\sigma = n_e e \mu_e + n_h e \mu_h \tag{C.3}$$

where n is the carrier density, (electrons or holes), e is the elementary charge and μ is the mobility of the carriers.

Typically, we produce devices in a field-effect geometry where the carrier density can be controlled via a voltage applied to a back-gate acting as one plate of a parallel plate capacitor.

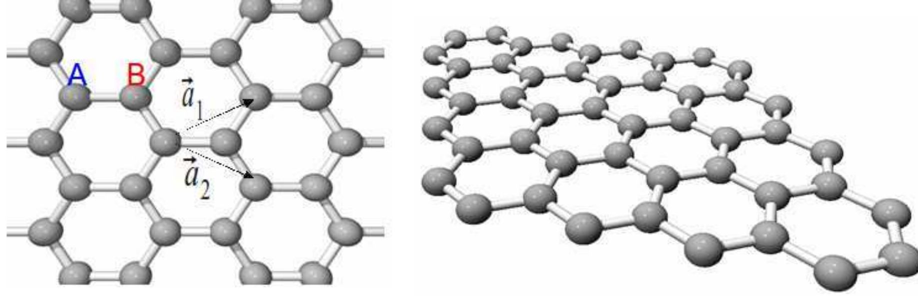

Figure C.1: Graphene lattice structure. The lattice vectors are given by $\vec{a}_1 = a_{C-C}\left(\frac{3}{2}\hat{x} + \frac{\sqrt{3}}{2}\hat{y}\right)$ and $\vec{a}_2 = a_{C-C}\left(\frac{3}{2}\hat{x} - \frac{\sqrt{3}}{2}\hat{y}\right)$ with $a_{C-C} = 1.4$ Å and the position of the A and B sublattices are indicated.

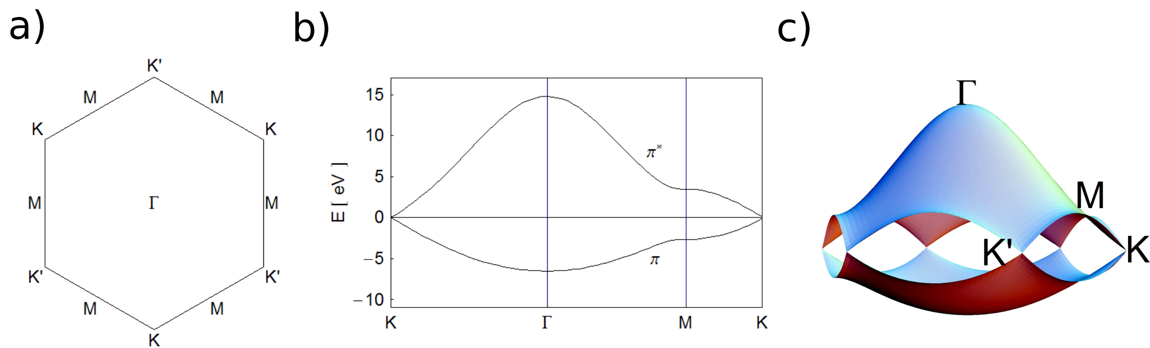

Figure C.2: Graphene electronic band structure. a) Hexagonal graphene Brillouin zone with high symmetry points labelled. b) Graphene band structure plotted along high symmetry directions. c) Full three dimensional graphene brillouin zone with high symmetry points labeled.

This allows us to convert an applied voltage into an induced charge in the graphene sheet via the standard capacitance relation

$$n = C_g|V_g - V_D| \tag{C.4}$$

Where C_g is the specific capacitance per unit area of the back gate (115 aF/ μm^2 for our 285 nm oxide) and a shift in the Dirac point V_D (point of minimum carrier density) from zero applied potential due to unintentionally introduced dopants has been taken into account as well. This relation allows us to extract the field-effect mobility of the carriers μ by fitting the linear portion of the conductance versus gate voltage curve.

$$\mu = \frac{1}{eC_g}\frac{\mathrm{d}\sigma}{\mathrm{d}V_g} \tag{C.5}$$

We can also use the charge carrier density to determine the Fermi wave vector via the two-dimensional density of states.

$$k_F = \sqrt{\pi n} = \sqrt{\pi C_g|V_g - V_D|} \tag{C.6}$$

Which allows us to extract the mean free path of the charge carriers

$$\ell_{mfp} = \frac{h}{2e^2}\frac{\sigma}{k_F} \tag{C.7}$$